INTERFACIAL ASSEMBLY OF NATURAL AND SYNTHETIC COMPONENTS FOR FUNCTIONAL BIONANOCOMPOSITES

A Dissertation
Presented to
The Academic Faculty

by

Michelle C. Krecker

In Partial Fulfillment
of the Requirements for the Degree
Doctor of Philosophy in the
School of Materials Science and Engineering

Georgia Institute of Technology
May 2021

INTERFACIAL ASSEMBLY OF NATURAL AND SYNTHETIC COMPONENTS FOR FUNCTIONAL BIONANOCOMPOSITES

Approved by:

Dr. Vladimir V. Tsukruk, Advisor
School of Materials Science and Engineering
Georgia Institute of Technology

Dr. Eric Vogel
School of Materials Science and Engineering
Georgia Institute of Technology

Dr. Valeria Milam
School of Materials Science and Engineering
Georgia Institute of Technology

Dr. Dhriti Nepal
Materials Science Directorate
Air Force Research Laboratory

Dr. Satish Kumar
School of Materials Science and Engineering
Georgia Institute of Technology

Date Approved: April 19, 2021

Dedicated to my family and friends.

ACKNOWLEDGEMENTS

These past five years have brought to me both great trials and great triumphs. Through each, I have had the privilege of unwavering support and guidance from those around me. First, I would like to thank my advisor Prof. Vladimir Tsukruk for his unending support, motivation, and wisdom. It has been a privilege to learn from and work with a distinguished scientist and professor who devotes so much time and effort into the wellbeing and success of his students. I would also like to express gratitude to Dr. Valeria Milam, Dr. Satish Kumar, Dr. Eric Vogel, and Dr. Dhriti Nepal for their willingness to serve as members of my committee and strengthening my work through valuable feedback.

I would like to acknowledge all past and present members of the SEMA lab for providing a great learning environment and helping me endure the challenges of research. Specifically, I would like to thank Dr. Rui Xiong, Dr. Ruilong Ma, and Dr. Anise Grant for their mentorship and training as well as Dr. Minkyu Kim and Daria Bukharina for their advice and contributions to my work. In addition, I would also like to thank collaborators Dr. Patrick Dennis, Dr. Maneesh Gupta, Dr. Chelsea Buck, and Marquise Crosby for support and training during my internships at the Air Force Research Laboratory and for providing us with the suckerin-12 protein and collaborators from Drexel university including Dr. Yury Gogotsi and Dr. Christine Hatter for providing MXene materials.

Finally, I would like to acknowledge my parents, Mark and Mindy, who have loved and supported me in every aspect of my life, my sisters, Kimberly, Jennifer, and Sarah, for never letting my confidence waver, and Debbie and Roger Walker for welcoming me into their family and guiding me during a critical time in my life.

TABLE OF CONTENTS

ACKNOWLEDGEMENTS ..... **iv**

LIST OF TABLES ..... **viii**

LIST OF FIGURES ..... **ix**

LIST OF SYMBOLS AND ABBREVIATIONS ..... **xiv**

SUMMARY…… ..... **xv**

CHAPTER 1. INTRODUCTION **1**

1.1 Natural Components 3

1.1.1 Silk Fibroin 5

1.1.2 Sucker Ring Protein 6

1.2 Two-Dimensional Flakes 7

1.2.1 Graphene Oxide 7

1.2.2 $Ti_3C_2T_x$ MXene 8

1. 3 Hybrid Materials 10

1.3.1 Modified Graphene Oxides 10

1.3.2 Modified MXenes 12

1.4 Nanocomposite Systems 13

1.4.1 Nanocomposite Assembly 13

1.4.2 Silk and Graphene Nanocomposites 14

1.4.3 MXene Nanocomposites 16

1.5 Limitations in Bionanocomposites 16

1.6 References 17

CHAPTER 2. GOALS, OBJECTIVES, AND ORGANIZATION AND COMPOSITION OF DISSERTATION **28**

2.1 Research Goals 28

2.2 Technical Objectives 29

2.3 Organization and Composition of Dissertation 30

CHAPTER 3. EXPERIMENTAL DETAILS **33**

3.1 Synthesis, Assembly, and Processing 33

3.1.1 Synthesis of 2D $Ti_3C_2T_x$ 33

3.1.2 Preparation of Silk Fibroin Solution 33

3.1.3 Preparation of Silk-Encapsulated MXene 34
3.1.4 Membrane fabrication via vacuum assisted filtration 35
3.2 Characterization 35
3.2.1 High Resolution Atomic Force Microscopy 35
3.2.2 Attenuated Total Reflectance Fourier Transform Infrared Spectroscopy 36
3.2.3 UV-Vis Spectroscopy 36
3.2.4 X-ray Photoelectron Spectroscopy 36
3.2.5 Scanning Electron Microscopy 37
3.2.6 Conductivity Measurements 37
3.2.7 Tensile Mechanical Testing 37
3.2.8 Buckling Mechanical Testing 38
3.3 References 38

CHAPTER 4. BIO-ENCAPSULATED MXENE FLAKES FOR ENHANCED STABILITY AND COMPOSITE PRECURSORS 40

4.1 Introduction 40
4.2 Experimental Details 42
4.2.1 Synthesis of Materials 42
4.2.4 Suspension Stability Studies 42
4.2.5 Transport Properties 43
4.2.6 Characterizations 43
4. 3 Results and Discussion 44
4.3.1 Morphology of silk-MXene flakes 44
4.3.2. Monitoring of secondary structure and surface chemistry of silk-MXene flakes .. 49
4.3.3 Morphology and Transport Properties of Silk-Encapsulated MXene Membranes 56
4.4 Conclusion 61
4.5 References 62

CHAPTER 5. MULTILAYERED NANOCOMPOSITES FROM SILK MODIFIED MXENES 70

5.1 Introduction 70
5.2.1 Solution Processing 71
5.2.2 Buckling Mechanical Testing 72
5.3 Results and Discussion 73
5.3.2 Morphology and Mechanical Properties of Multilayered Composites 75

5.3.2 Mechanical Properties of Individual Nanosheets 79
5.4 Conclusion 81
5.5 References 82

CHAPTER 6. SUCKERIN-12 ENCAPSULATED MXENE STABILITY VIA HOFMEISTER SALT ANNEALING 85
6.1 Introduction 85
6.2.1 Materials 86
6.2.2 Sample Preparation 86
6.3 Results and Discussion 88
6.3.1 Composition and Deposition Mode Dependent Suckerin-12 Thin Film Formation 88
6.3.2 Hofmeister Salt Aided Suckerin-12 Stabilization and Assembly 90
6.3.3 Morphology of Suckerin-12-MXene Nanosheets 93
6.3.2 Manipulation of Secondary Structure of Suckerin-12 Using Salts 94
6.4 Conclusion 98
6.5 References 100

CHAPTER 7. GENERAL CONCLUSIONS AND BROADER IMPACT 102

APPENDIX A. CHAPTER 4 SUPPORTING INFORMATION 109

APPENDIX B. CHAPTER 6 SUPPORTING INFORMATION 122

LIST OF TABLES

Table 1.1 Bionanocomposites containing functionalized graphene oxides and biomaterials……
.11

Table 4.1 Table showing resistance measurements obtained via four-point-probe measurements on MXene and SFMX papers fabricated using vacuum assisted filtration as well as literature reported values……58

Table A.1 Table showing permeance and dye rejection performance of MX and SFMX vacuum assisted filtration films……121

Table B.1 Summary of processing conditions and RMS roughness measurements discussed in the main text for suckerin-12 films……...122

Table B.2 Summary of processing conditions and RMS roughness measurements for suckerin-12-MXene systems as discussed in the main text……..….123

LIST OF FIGURES

Figure 1.1 Schematics showing (a) grains held together with biopolymers, (b) mechanisms of sliding with and without organic layers, (c) interlocking $CaCO_3$ plates with protein mortar in nacre, (d) crack bridging shown with horizontal tension, as well as comparisons of (e) strength, and (f) toughness of natural nacre and synthetic composites. Figure from ref. [9]……..……2

Figure 1.2 Chemical and domain structures of (a) silk fibroin modified from ref.,[10,11] (b) nanocellulose,[12,13] (c) 3, 4, 5trihydroxyphenethylamine (TOPA),[14] (d) graphene oxide,[15] and (e) $Ti_3C_2T_x$ MXene where T= O, OH, or F.[16]……4

Figure 1.3 Schematic of (a) MXenes and their corresponding MAX phases,[39] and the structure of $Ti_3C_2T_x$ with varying degrees of T= -O, OH, and F groups in the (b) stacking direction, (c) top view, and (d) illustration of hydrogen bonding (black dotted lines) between layers. Figure b-d modified from ref.[40]……..9

Figure 1.4 Graphene oxide functionalization routes through non-covalent and covalent interactions on basal planes and sheet edges.[65]……..10

Figure 1.5 Fabrication of ordered bionanocomposites via (a) layer-by-layer assembly, (b) vacuum assisted filtration, and (c) cast drying.[1] (Figure modified from ref [77–79])……13

Figure 2.1. Schematic showing material components and research plan……28

Figure 4.1 Surface modification of MXene flakes with silk fibroin: (a) Single flake of $Ti_3C_2T_x$ MXene with surface functional groups (T_x = O, OH, F) and co-assembly of silk fibroin on flake surfaces; (b) typical amino acid composition of silk backbones.[8,9] (c) Schematic representation of individual encapsulated flake on silicon substrate with parameters derived from high resolution atomic force microscopy (HRAFM) imaging; (d) layered morphology of a thin bio-MXene film assembled via vacuum assisted filtration of SFMX dispersions……..41

Figure 4.2 AFM topography images (top), corresponding phase images (middle), and height histograms (bottom) from the selected white boxes of a pristine $Ti_3C_2T_x$ MXene flake (a) and after silk deposition and rinsing (b). Z-scale is 7 nm for topography and 6° scale for phase images (all scale bars are 200 nm) ….……45

Figure 4.3 AFM topography images (top) and corresponding phase images (bottom) of co-assembled SFMX on days one (a), three (b), five (c), seven (d), and 19 (e) with 20 nm Z-scale for topography, and 6° scale for phase images. Topography images are provided in false color to better show silk corona morphology……46

Figure 4.4 ATR-FTIR spectra of SFMX over time (a), examples of deconvolution for day one (b) and day 19 (c), and the secondary structure of the silk evolution in SFMX after different co-assembly time (d)……50

Figure 4.5 Ti 2p XPS spectra of MXene (a, b) and Silk modified MXene (c, d) on day one (a, c) and after being kept in water for 22 days at room temperature (b, d) ……51

Figure 4.6 UV-Vis spectra of pristine MXene (a, b) and silk modified MXene (c, d) at 0.01 wt% in water showing 2 peaks between 235 and 385 nm (a, c) and one between 650 to 900 nm (b, d) ……...…….53

Figure 4.7 Plots of UV-Vis peak position and absorbance intensity for peaks 3 (a) and 5 (b, c) as designated in Figure A.8 for pristine MXene (a, b) and SFMX (c) suspensions…….55

Figure 4.8 SEM micrographs showing cross sections of fractured MXene (a) and SFMX (b, c) membranes assembled via vacuum assisted filtration; (c) shows a magnified image of the area framed in (b)…….57

Figure 4.9 Pictures showing an LED set up with a 9V battery (a) lighting up a 5.2 μm thick MXene paper (b) and a 10.6 μm thick SFMX paper (c)……..59

Figure 4.10 Images of a representative SFMX film on track-etched polycarbonate membrane before (a) after (b) filtering out MB dye. Optical images of glass vials containing filtrate solution before (c) and after being filtered with MXene films (d) and SFMX films(e)…….....60

Figure 5.1 AFM images of SFMX flakes spun cast from solutions kept at 25°C (a), 35°C (b), and 50°C (c) for 24 hours and high-resolution titanium XPS spectra of fresh SFMX (d) and SFMX after 24 hours at 50°C. AFM image scale bars and z scales are 400 nm and 15 nm, respectively…….74

Figure 5.2 SEM images of papers made from pristine MXene (a), fresh SFMX (b) and SFMX after 22 days at 4°C. Scale bars are 5 μm……76

Figure 5.3 Stress-strain curves from tensile tests of pristine MXene, fresh SFMX, and SFMX from day 22 (a) and composites made with varying weight per cent concentrations of silk (b)……77

Figure 5.4 Plots containing values of modulus (a), ultimate stress (b), and ultimate strain (c) obtained from tensile tests of MXene silk composites at different weight per cents of silk……..78

Figure 5.5 AFM images and corresponding height profiles (bottom) of pristine MXene (a, b), fresh SFMX (c, d), and SFMX after day 22 days at 4°C (e, f) on PDMS substrates before (a, c, d) and after (b, d, f) 30% uniaxial compression. Scale bars are 400 nm, and the z scale is 40 nm……..80

Figure 6.1 ATR-FTIR of drop (A) and spin cast (B) 1 wt% suckerin-12 where deconvoluted peaks are displayed under the overall amide 1 peak to show how ATR-FTIR spectra were analyzed. The secondary structure in each sample calculated from peak area of their respective peaks is given in (C)……..89

Figure 6.2 ATR-FTIR of the amide 1 peak of spin cast 1 wt% suckerin-12 films before (control) and after salt annealing for 1 hr (A) as well as a graph of the secondary structure composition derived from deconvolution of the spectra (B)……..91

Figure 6.3 AFM topography images (top) and corresponding height histograms (bottom) of a pristine MXene flake before (a) and after (b) suckerin-12 deposition. Scale bars are 400 nm, and the z scale is 9 nm……..….94

Figure 6.4 AFM topography images (top) and corresponding height histograms (bottom) of MXene flakes with suckerin deposited after soaking in 100m M sodium citrate (a, b) and 100mM sodium sulfate (c, d) for one hour (a, c) and 11 days (b, d). Z scale is 9 nm……..95

Figure 6.5 AFM topography images (top) taken with an ultrasharp tip and corresponding height histograms (bottom) of MXene flakes with suckerin deposited after soaking in 100 mM sodium sulfate (a) sodium citrate (b), sodium phosphate (c), and sodium acetate (d) for 16 hours. Scale bars are 400 nm, squares are 300 nm X 300 nm, and Z scales are 12 nm……..96

Figure 6.6 AFM topography images (top) taken with an ultrasharp tip and corresponding height histograms (bottom) of drop (a) and spin (b) cast MXene flakes directly modified with suckerin-12 in solution. Scale bars are 400 nm, squares are 300 nm X 300 nm, and Z scales are 12 nm…….97

Figure 6.7 AFM topography images (top) taken with an ultrasharp tip and corresponding height histograms (bottom) of MXene flakes directly modified with suckerin-12 in solution deposited via spin casting after soaking in 100 mM sodium sulfate (a) sodium citrate (b), sodium phosphate (c), and sodium acetate (d) for 16 hours. Scale bars are 400 nm, squares are 300 nm X 300 nm, and Z scales are 12 nm……98

Figure A.1 AFM topography images of pristine MXene (a) and SFMX on day 1 (b) with 16 nm Z-scale and 500 nm scale bars……109

Figure A.2 AFM topography images of SFMX on day 3 with 16 nm Z-scale and 500 nm scale bars……..109

Figure A.3 AFM topography images of SFMX on day 5 with 16 nm Z-scale and 500 nm scale bars……..110

Figure A.4 AFM topography images of SFMX on day 7 with 16 nm Z-scale and 500 nm scale bars……..110

Figure A.5 AFM topography images of SFMX on day 19 with 16 nm Z-scale and 500 nm scale bars……..…111

Figure A.6 A topographical AFM image of a day three SFMX flake (a) with corresponding height histogram showing flake and corona height (b), flake height profile showing size of corona (c), and profile showing a fibril height (d)…….112

Figure A.7 AFM images of silk spin (a, c, e, g) and dip (b, d, f, h) cast from 0.1 wt% silk solution that was kept at 4 °C for 105 days (a, b) and six days (c, d, e, f, g, h). The images include silk films allowed to sit in water at 4 °C (e, f) and 50 °C (g, h) for three days. Z scale is 10 nm and scale bars are 200 nm…….113

Figure A.8 ATR-FTIR spectra of silk and SFMX from fresh solutions and those kept at 4 °C for 22 days……...114

Figure A.9 XPS spectra of pristine MXene and SFMX after being stored in water at 4°C and room temperature over a period of 22 days……115

Figure A.10 UV-Vis spectra of pristine silk, MXene, and SFMX solutions at 0.01 wt% from (a) 180-1000 nm and from (b) 180-350 nm to show the peak origins of the SFMX..116

Figure A.11 Plots of UV-Vis peak position and absorbance intensity for peaks 3 (a), 4 (b) and 5 (c) as designated in Figure A.10…….117

Figure A.12 AFM topography images and corresponding histograms of pristine MXene (a), SFMX (b), MeOH vapor treated SFMX (c), and MeOH solvent treated SFMX. Scale bars are 200 nm and Z scale is 30 nm……117

Figure A.13 AFM topographical (top) and corresponding phase (bottom) images (Z=25 nm, phase=10°, Scale bar=500 nm) of dip cast SFMX flakes (a) allowed to dry by evaporation and (b) dried with an air gun as well as one flake spun cast from water at 3000 rpm for 30 seconds (c) before and (d) after being rinsed with water via spin casting……118

Figure A.14 SEM images showing the thickness of MX (a, c) and SFMX (b, d) vacuum filtered papers……...119

Figure A.15 UV-Vis spectra of PMR (a, b), BB (c, d), P (e, f), R6G (g, h), and MB (i, j) dye solutions before (black) and after (orange) filtering through MX (a, c, e, g, i) SFMX (b, d, f, h, j) films……..120

Figure B.1 ATR-FTIR spectra corresponding to those shown in Figures 6.1 (A) and 6.2 (B) meant to show the full length of the spectra taken (left) as well as a zoomed in version (right) showing the amide I and II bands……..124

Figure B.2 Peak deconvolutions (grey) of the amide I bands in ATR-FTIR spectra of suckerin-12 films before and after salt annealing (Figure 6.2). The original background subtracted curve is shown as a black dashed line…….125

Figure B.3 AFM topographical images of spin cast 3 wt% suckerin-12 films after salt annealing for 1 hour with sodium phosphate (A), sodium acetate (B), sodium citrate (C), and sodium sulfate (D). Scale: 1 um. Z range: 33 nm (A), 38 nm (B), 30 nm (C), and 36 nm (D)……..126

Figure B.4 AFM topographical images of spin cast, salt annealed 3 wt% suckerin-12 films before (A, C, E, G) and after (B, D, F, H) immersion in water. The samples shown were neat (A, B) and annealed with sodium phosphate (C, D), sodium acetate (E, F), sodium citrate (G, H), and sodium sulfate (I, J). Scale: 1 um. Z range: 20 nm (A-H) ……127

Figure B.5 AFM topographical images displaying overall morphology (a, c, e, g, i) and isolated fibrils (b, d, f, h, j) of suckerin-12 films drop cast from 0.1 wt% solution, rinsed, and then salt annealed for 16 hours with 100 mM of sodium sulfate (c, d), sodium citrate (e, f), sodium phosphate (g, h), and sodium acetate (i, j). Scale bars are 100 nm and Z scales are 2.5 nm (a, c, e, g, i) and 6 nm (b, d, f, h, j) ……128

LIST OF SYMBOLS AND ABBREVIATIONS

ATR-FTIR	attenuated total reflectance Fourier transform infrared spectroscopy
DLS	dynamic light scattering
HRAFM	high resolution atomic force microscopy
MX	MXene
PDMS	Polydimethylsiloxane
SEM	scanning electron microscopy
SF	silk fibroin
SFMX	silk encapsulated MXene
UV-Vis	ultraviolet-visible light spectroscopy
VAF	vacuum assisted filtration
XPS	x-ray photoelectron spectroscopy
ζ-potential	zeta potential

SUMMARY

Organized bionanocomposites are promising new materials since they are biocompatible, biodegradable, and can be used in a variety of applications such as flexible electronics, wearable sensors, and molecular sieving membranes. However, their mechanical and functional performance is not up to theoretical predictions due to a gap in understanding fundamental interactions between the biopolymeric and synthetic components of multilayered composite films. This work will focus on chemical and morphological changes of structural proteins in intimate contact with two-dimensional nanofillers when exposed to differing chemical environments and the resulting mechanical and conductive properties of multilayers composites.

The first task aims to unveil the mechanisms behind silk fibroin's natural morphological reorganization in direct contact with the surface of $Ti_3C_2T_x$ MXene over time in aqueous solution. In the second task, the mechanical properties of silk-MXene multilayered composite films were investigated. Finally, suckerin-12 protein encapsulated MXene flakes are fabricated and their morphological reorganization in response to salt annealing was studied. These studies showed that MXene can be uniformly encapsulated by proteins with secondary structures that can be manipulated with non-covalent methods. Organized layered nanocomposites formed from these hybrid materials display enhanced mechanical properties dependent upon protein concentration and secondary structure.

This work will inspire the fabrication of functional bionanocomposites with tailorable properties facilitated through interfacial interaction manipulation via non-covalent methods. These studies provide a framework for understanding interfacial interactions between structural proteins and two-dimensional synthetic materials and outlines techniques with which functional organized protein composites can be designed.

CHAPTER 1. INTRODUCTION

Natural nanocomposites are known for having unique mechanical properties achieved with varying hierarchical structures. Specifically, silk and cellulose have gained attention in recent years as high performance materials for controlled drug delivery, nanocomposite films, bio-sensing applications and more due to their natural abundance, mechanical toughness, and high strength.[1] These natural components have been assembled with other synthetic components such as graphene oxide for increased strength and functionalities in electronic applications.[2–5] The unique characteristics given by the versatility of these components lend a degree of variability and tunability not achieved in traditional composites. Fundamental understanding of interfacial organization and how it pertains to macroscopic mechanical and chemical properties offers insight required to design highly strong and functional composites for different applications.

The future of nanomaterials is in the ability to enhance structural properties and provide added functionalities to enable emerging nanotechnologies and their prospective applications to thrive. Specifically, nanomaterials need to improve upon the mechanical performance of traditional materials while introducing novel functionalities like sensing, self-healing, and energy storage.[1] Examples include UV-protecting coatings on vehicles that provide self-healing functions or clothing that is robust and comfortable while providing chemical sensing useful for detecting toxic chemicals or monitoring the health of the wearer.[1] Specifically, bionanocomposites offer a unique approach to this field due to their ability to enhance mechanical, optical, and electrical properties while simultaneously being responsive, biocompatible, biodegradable, and made from earth-abundant sources.

Aside from providing resources, nature provides an abundance of inspiration for functional materials. Spiders extrude dual functional silk fibers that are adhesive for catching prey and robust for building webs while wood is both strong and tough, which is

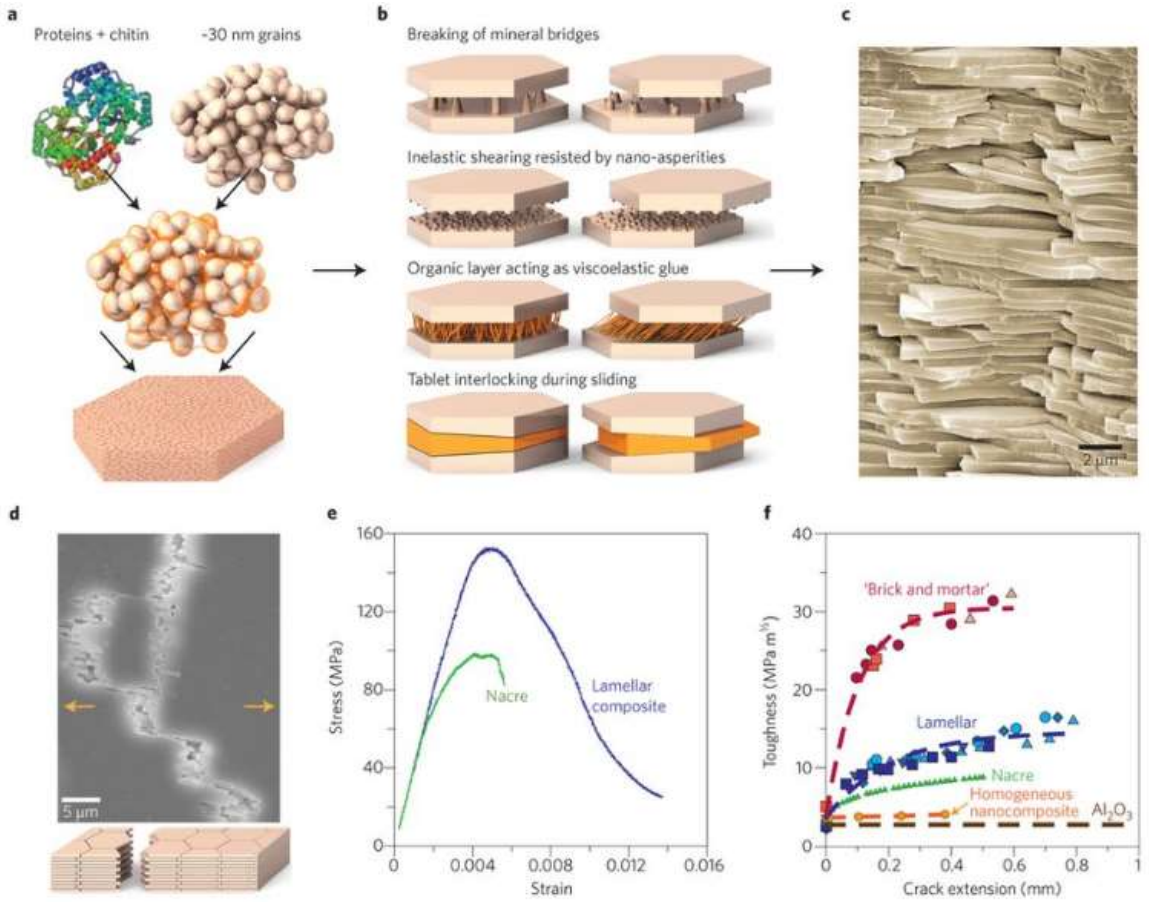

Figure 1.1 Schematics showing (a) grains held together with biopolymers, (b) mechanisms of sliding with and without organic layers, (c) interlocking $CaCO_3$ plates with protein mortar in nacre, (d) crack bridging shown with horizontal tension, as well as comparisons of (e) strength, and (f) toughness of natural nacre and synthetic composites. Figure from ref. [6]

difficult to obtain together, due to hierarchical organization of proteins and nanocelluloses, respectively.[1,7,8] Nacre is a composite material of both hexagonal platelets of inorganic

grains glued by proteins and organic components that make up the shells of some cephalopods, gastropods, and even pearls.[9] These shells gain their strength from the organization of the inorganic platelets and organic proteins, shown in Figure 1.1, giving inspiration to laminated composites.[6] Hard plates like in nacre or 2D flakes like graphene oxide or $Ti_3C_2T_x$ MXene are very strong but are brittle if their movement isn't mediated by some flexible component thus making hybrid materials with strong plates and soft organic constituents good candidates for materials with tunable mechanical properties.

The field of organized bionanocomposites uses inspiration and derivation from natural systems to solve problems in unique ways. Bionanocomposites can be optically active, electrically conductive, and self-healing. These properties can be achieved by incorporating synthetic components with useful properties like conductivity and optical activity into functional biopolymer matrices. Specifically, the natural components can mediate movement of the flakes while providing responsive behavior to external stimuli such as pH changes, temperature, humidity, etc. to achieve tunable properties.[1] While these numerous properties are imperative to the development of responsive and functional composites, the natural components provide a certain complexity that cannot be easily discerned. Thus, it is important to understand how these natural components act in contact with synthetic fillers in different environments to better design bionanocomposites for specific applications.

1.1 Natural Components

Due to the complexity and efficiency of biological systems, nature has inspired the use of bio-derived materials and functional structures. As shown in Figure 1.2, the bio-

derived materials to be used in this work include silk fibroin and suckerin-12 proteins while $Ti_3C_2T_x$ MXene will serve as the synthetic component. Considering that much has been done in this area with graphene oxide, it is important to understand its chemistry and interactions and use the knowledge as a model for systems in this work involving MXene. Both synthetic materials are electrically conductive and mechanically strong 2D flakes with

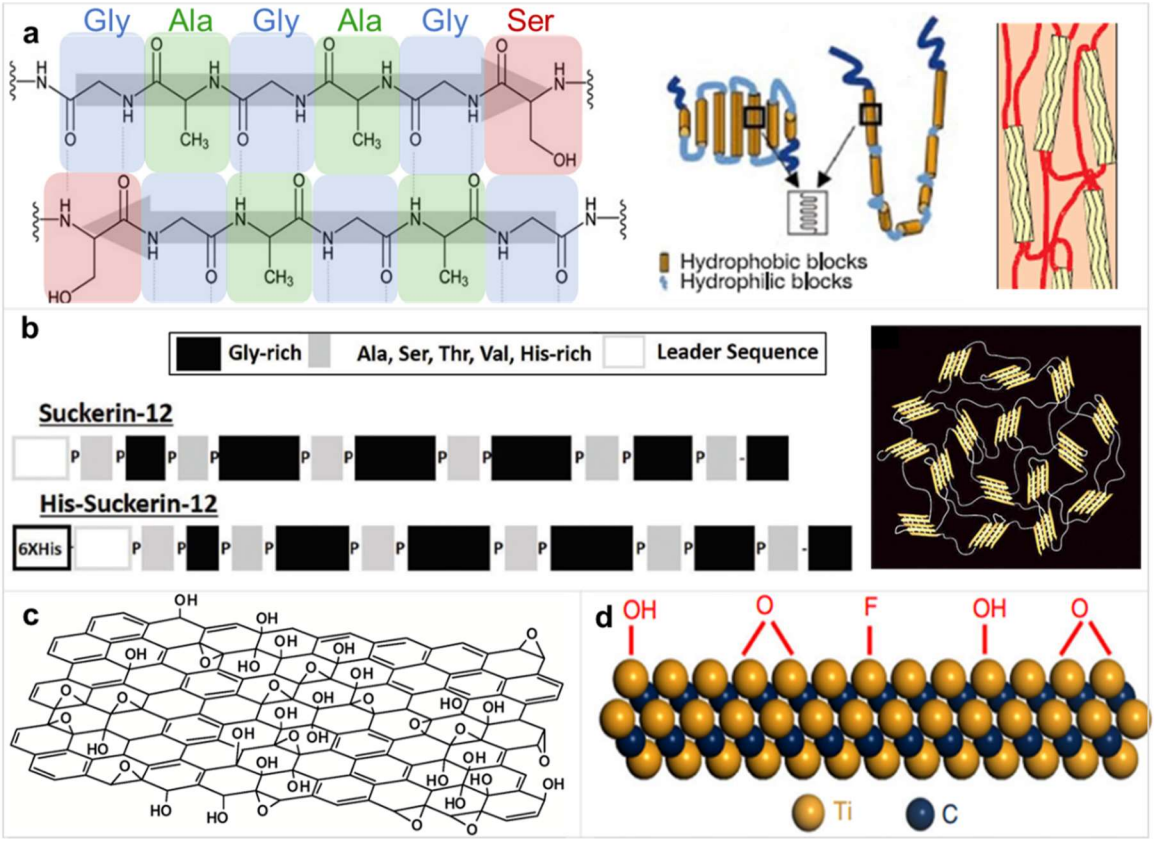

Figure 1.2 Chemical and domain structures of (a) silk fibroin modified from ref.,[10,11] (b) suckerin-12 modified from ref.,[12,13] (c) graphene oxide,[14] and (e) $Ti_3C_2T_x$ MXene where T= O, OH, or F.[15]

surface moieties, containing oxygen, that provide availability for functionalization as well as solvent and chemical interface interactions. Silk fibroin and suckerin-12 materials will

provide strength and tunability to laminated bionanocomposites through secondary structure mediation and adhesion.

1.1.1 Silk Fibroin

Among the most popular biopolymer materials explored for bionanocomposites is silk fibroin. It is created by several species including many types of spiders and *bombyx mori* worms for purposes in protection from prey and sunlight and for movement.[7] The animal itself can choose when and what type of silk to extrude based on its current need such as dragline, cocoon, or web. Due to their ability to form into strong beta sheet structures, silk fibers have proven to be stronger than many conventional materials such as steel and Kevlar making it a massive interest in the scientific community.[16]

The mechanical strength of silk lies in its glycine and alanine rich domains that create anti-parallel beta-sheets, modeled in Figure 2a, while its bendability its attributed to the helices and random coils comprised of glycine and tyrosine domains.[7,16–18] Even after extrusion, some modification can take place when annealed with water vapor, methanol, or heat making them useful for applications in sensors and responsive materials.[19] While reconstituted silk is solution processible, it lacks the hierarchical structure and strength of raw silk since it requires the use of chaotropic agents to cut the fibrils.[20,21] However, it has been shown that the secondary structure of recombinant silk can change in response to mechanical shearing, chemical environment changes, and solvent annealing allowing for tunability in post processing.[17,18]

Specifically, silk from *Bombyx Mori* worms contain both hydrophilic blocks rich in tyrosine and glycine and hydrophobic blocks of alanine and glycine that give rise to the

overall hierarchical design of a fibroin (Figure 4.1b).[16] These blocks are composed of various secondary structures brought on by hydrogen bonding between chains such as β-sheets and random coils that determine the size of each block and also the ultimate mechanical strength. Due to its unique chemical design with diverse multidomain composition, silk fibroin can interact with heterogeneous inorganic fillers through electrostatic, van der Waals, hydrophobic, and hydrogen bonding of different blocks.[22] This makes it an attractive material for nanocomposites with enhanced interfacial strength as demonstrated with graphene oxide at different reduced states such as biographene papers.[11,19,23] Many of these nanocomposites can be made into ultrathin, transparent, strong, electrically conductive, and optically active films or fibers.[1,24–26]

1.1.2 Sucker Ring Protein

Recently, another family of proteins with similar structures to silk has been discovered in the sucker ring teeth (SRT) of cephalopods and are aptly named suckerins. These teeth were found to be all protein and comprised of different isoforms held together with hydrophobic and hydrogen-bonding interations.[27] These proteins provide high hydrated and dry moduli of 4 GPa and 8 GPa, respectively, to the SRT.[28] The suckerin protein family consists of 35 isoforms with unique amino acid sequences and molecular weights. Great scientific interest has been sparked in this family of proteins due to their β-sheet dominated structure that creates strong nanoscale constructs by self-assembling without the need of crosslinking mineralization.[29,30]

Despite their similarity to silk, suckerins are modular proteins that can be expressed with monodisperse molecular weights from 5 to 60 kDa.[13,31] The block-copolymer like

proteins form structures consisting of isotropically oriented β-sheets, typically composed of histidine, alanine, and threonine in an amorphous matrix of glycine, tyrosine, and leucine.[13] β-sheets are brought on by intermolecular bonding and strong pH sensitive peptide-peptide bonds are formed in histidine and alanine rich segments.[32] The isoform used in this study is a histidine tagged form of the smaller suckerin-12 isoform with a molecular weight of only 27 kDa and a chemical structure consisting largely of 29%, 15%, 12%, and 8% of glycine, tyrosine, alanine, and histidine, respectively.[12] Given histidine's propensity for deprotonation at higher pH, it can aid the self-assembly of the protein while alternatively increasing solubility at a low pH. This allows for tunable control in secondary structure manipulation that could prove useful in composite materials.

1.2 Two-Dimensional Flakes

Two-dimensional (2D) functional materials such as graphene, transition metal dichalcogenides, and hexagonal boron nitride have garnered much interest in the scientific community due to their unique chemical, electrical, photonic, and structural properties as pure materials and as components of composites.[1,14,33–38]

1.2.1 Graphene Oxide

Two-dimensional materials like graphene are of considerable interest as bionanocomposite fillers due to their unique geometry that allows for high strength, electrical conductivity, and high light transmittance. This unique geometry specifically allows graphene to have a transmittance as high as 97%, a low electrical sheet resistance of 125 ohm m^{-1}, and a Young's modulus of 1TPa even at less than a nanometer in thickness.[39] However, the lack of surface functionalities creates enormous difficulty in

processing, giving rise to graphene oxide (GO), a 2D sheet of graphene with a high concentration of oxygen moieties that makes it dispersible in water.

Like graphene, GO is transparent due to its single-atom thick layer and strong due to the honeycomb basal plane structure. Perhaps the most interesting part of GO is the surface hydroxyl, epoxy, and oxygen groups that make it hydrophilic, dispersible in water, and capable of hydrogen bonding.[14] GO has been found to have use in many applications in strong composites, sensors, and even biological imaging due to its unique chemical structure. GO is frequently paired with biopolymers like cellulose and silk to make robust, electrically conductive, and flexible nanocomposites.[2,5,40]

1.2.2 $Ti_3C_2T_x$ MXene

In recent years, a novel family of 2D materials known as MXenes[41,42] has become the subject of intense research due to their high electrical conductivity upwards of 15,000 S cm^{-1} (Ti_3C_2)[43] coupled with the high Young's modulus values, 330 ± 30 GPa for Ti_3C_2[44] and 386 ± 13 GPa for Nb_4C_3,[45] among solution-processed 2D materials.[44,46,47] Their rich surface chemistries and chemical functionalities make MXenes viable for a large variety of applications in electronics, separation membranes, wearable sensors, and biomaterials for medical use.[48,49]

As shown in Figure 1.3a, MXenes are created by etching the A component from a MAX phase where M is an early transition metal, A is usually a group IIIA or IVA element, and X is nitrogen and/or carbon.[49] These materials consist of $M_{n+1}X_nT_X$ layers (n=1, 2, or 3) where T_x represents a surface terminal functional group of either -OH, =O, or -F that is formed as a result of the etching process.

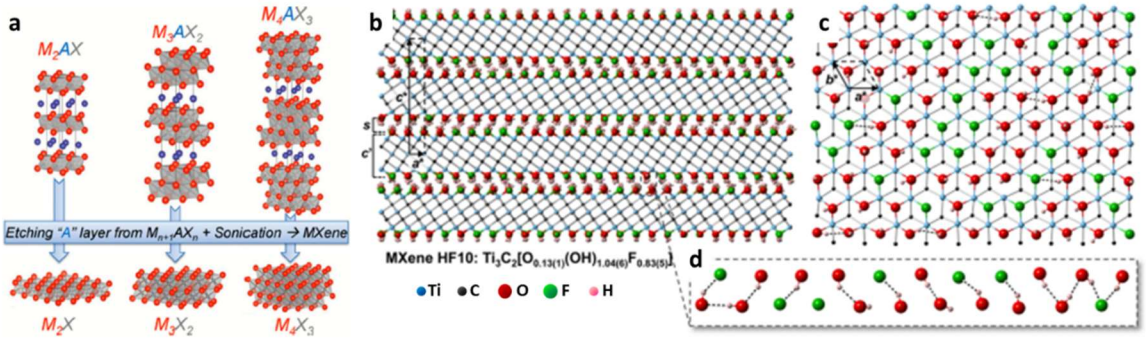

Figure 1.3 Schematic of (a) MXenes and their corresponding MAX phases,[49] and the structure of $Ti_3C_2T_x$ with varying degrees of T= -O, OH, and F groups in the (b) stacking direction, (c) top view, and (d) illustration of hydrogen bonding (black dotted lines) between layers. Figure b-d modified from ref.[50]

For this study, $Ti_3C_2T_X$, etched from Ti_3AlC_2 using LiF and HCl, was obtained from collaborator Prof. Gogotsi's group at Drexel University. Our collaborators have extensive experience in synthesis and study of MXenes for various applications from electrically conductive films to molecular sieving membranes.[48,49,51,52] Due to the nature of the synthesis, MXenes typically have O, OH, and F pendant groups giving it a slightly amphiphilic nature allowing for solution processing.[49] Despite having surface functional groups that allow for dispersion in various polar solvents and reduce oxidation upon storage and use, without proper surface modification, a propensity for oxidation in humid environments and restacking in aqueous suspensions may cause significant reduction of conductivity and mechanical performance over time.[34] Unlike graphene oxide, these groups do not reduce the conductivity of the flake so much that it cannot compete with others of its type making it an obvious choice for applications in electronics.

The surface chemistry of MXenes is difficult to determine however, some studies suggest that the ratio of =O, -OH, and -F groups on the surface of the flakes can be changed

using different synthesis methods.[53] Modeling has been used to show more detailed structures of atoms in MXene flakes with emphasis on the surface terminations. Figure 3b shows one of the more stable structures of MXene with an approximate ratio of 3:24:19 for oxygen, hydroxyl, and fluorine groups, respectively.[50] While modeling proves to be useful, experimental results are necessary for confirmation.

1. 3 Hybrid Materials

1.3.1 Modified Graphene Oxides

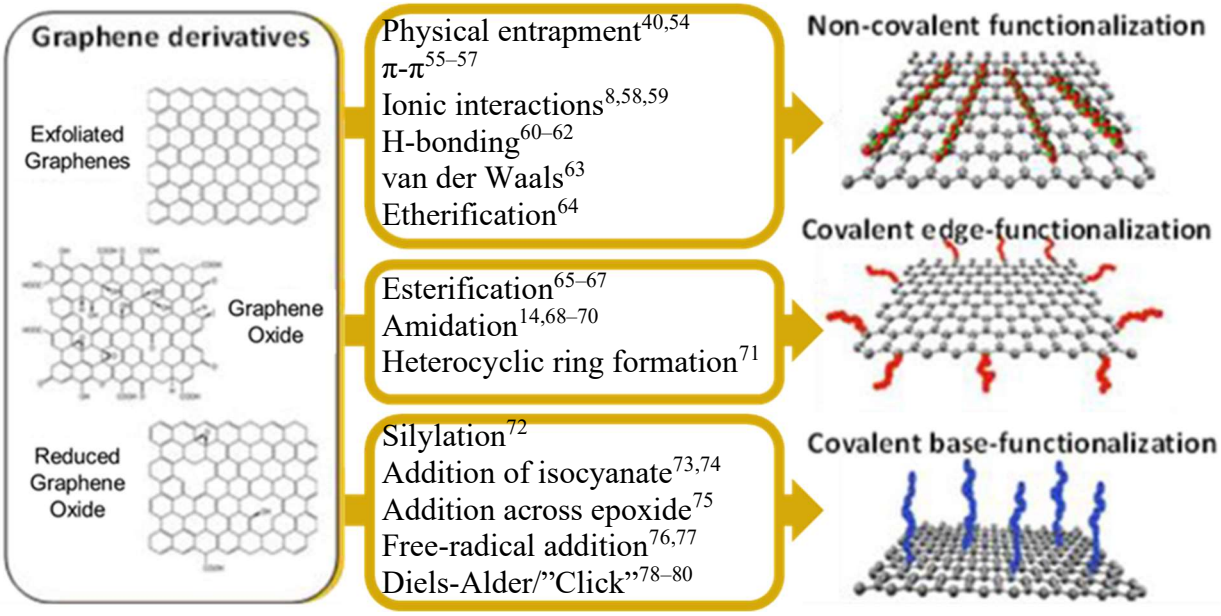

Figure 1.4 Graphene oxide functionalization routes through non-covalent and covalent interactions on basal planes and sheet edges.[76]

Although there has been extensive recent research interest in the modification of graphene derivatives and MXenes, there does not yet exist a commensurate research effort into the incorporation of modified flakes into novel, functional composite materials.

However, in the past few years some studies have shown that modified flake-based bionanocomposites can be used for a variety of functional applications.

Because these composites consist of bio-derived materials, they are often capable of degradation, reduced cytotoxicity, and enhanced biocompatibility making them eco-friendly and viable for biomedical applications. Modified graphene oxide (MGO) is central to the desired mechanisms of these bionanocomposites. These studies show that MGO

Table 1.1 Bionanocomposites containing functionalized graphene oxides and biomaterials.

Bio-derived material	Surface Modification	Method of assembly	Reported Application	Issues	Ref
Chitosan	Nitrene chemical reduction and grafted chitosan	Drop cast	Biosensors, tissue engineering, separation membranes, and food and biomedical packaging	Poor MGO ordering and low mechanical strength	[81,82]
Poly (lactic acid)	Starch	Compression molding	Thermally stable, structural film with gas barrier	Low mechanical strength and gas barrier	[83]
Cellulose acetate	Sulfonated poly (ether-ether-ketone)	Drop cast	Strong films with gas barrier and thermal stability	Low mechanical strength and gas barrier	[64]
Sodium Alginate	Tetraethylene pentamine	Drop cast	Strong, thermally stable, biodegradable films	Low mechanical strength	[84]
Polylactide	Grafted polylactide	Drop cast	Bone replacement and packaging	Aggregations and low optical transparency	[60]

containing bionanocomposites can be well functionalized and tuned to be useful for very specific applications. Many of these bionanocomposites have dual functionalities such as artificial muscles used for actuator applications or mechanically enhanced composites with antimicrobial properties. GO and MGO have been shown to also increase the oxygen barrier of composites so it is expected that various combinations of modified flakes and biopolymers could arise and be useful in several fields not obviously related. Since MGO bionanocomposites have increased mechanical properties and biocompatibility it is also reasonable to expect even more studies on these composites for biomedical applications.

1.3.2 Modified MXenes

Scientists have begun to modify the surface of MXene flakes in recent years as well. Typically, small molecules such as aluminum ions and metal nanoparticles are investigated with a distinct lack of large molecule attachment.[85,86] MXene is welcome to the addition of such materials since it has an abundance of surface =O, -OH, and -F pendant groups. Modification of 2D flakes can add functionality to the already great material as well as offer stability in solution and against oxidation and aggregation, a current issue with $T_3C_2T_X$ MXenes.

Due to their numerous pendant groups, MXenes and graphene oxides are solution processable and therefore can be modified in aqueous solution. Previously, scientists have attached polydopamine by mixing dopamine and graphene oxide in aqueous solution while polymerization takes place. Hydrophilic and amphiphilic copolymers have been shown to graft directly to the surface of graphene oxide in water.[3] These 2D flakes can be dispersed in water and mixed with an aqueous solution of biopolymer to form uniform coatings of

said biopolymer. Excess material can be washed away with simple centrifugation steps since these biopolymers are more attracted to the surface of the 2D flakes than the surrounding solution.

1.4 Nanocomposite Systems

1.4.1 Nanocomposite Assembly

The organization of individual components in nanocomposites is of vital importance to its mechanical, electrical, and chemical performance. As such, it's no surprise there are numerous ways of assembling the components including layer-by-layer (LbL) assembly via dip, spray, and spin casting onto various substrates.[87] This method is frequently used to create organized and ultra-thin films with nanoscale precision for

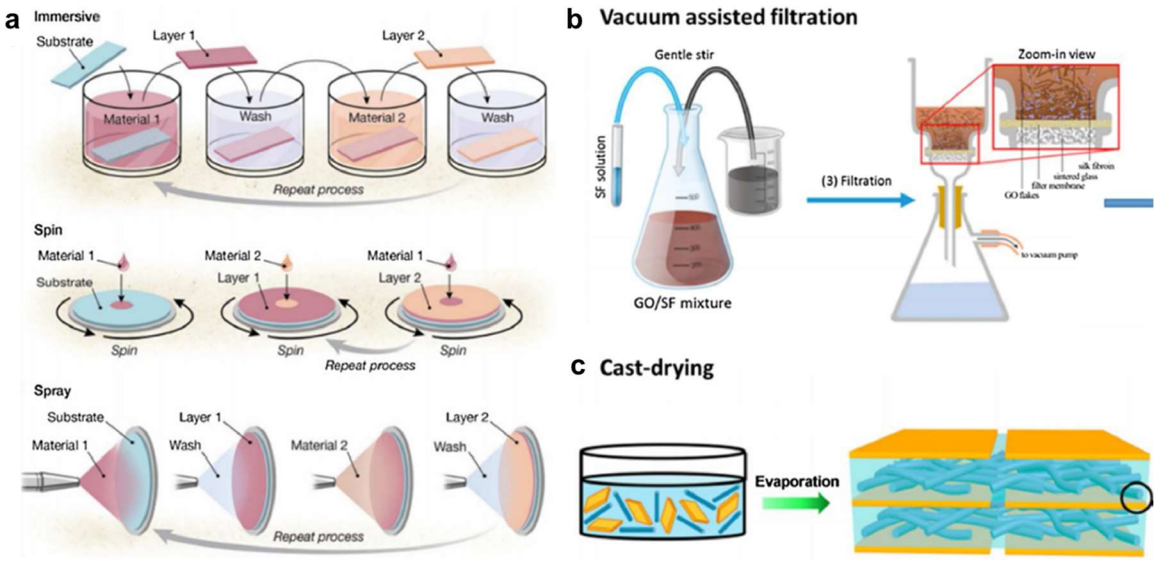

Figure 1.5 Fabrication of ordered bionanocomposites via (a) layer-by-layer assembly, (b) vacuum assisted filtration, and (c) cast drying.[1] (Figure modified from ref [87–89])

various applications. Using the unique chemistries of the components, one can alternately layer positively charged material with a negatively charged material to make a film held together by electrostatic attraction. Specifically, mechanically strong and robust laminated structures inspired by nature's nacre design can be made with this method. While the components discussed in the previous section are highly useful, they can be combined in variations that afford useful characteristics. Biopolymers provide an option for tunability, increased strength, and glue for strong, functional, and electrically conductive 2D materials.

Precision and high degrees of ordering are extremely useful in retaining good functionality but LbL is time consuming and is difficult to scale up leading to another methods of assembly called one-pot assembly. In this technique the components are mixed before fabrication via drop casting, Meyer bar coating, or vacuum filtration. While the components discussed in the previous section are highly useful, they can be combined in variations that afford useful characteristics. Biopolymers provide an option for tunability, increased strength, and glue for strong, functional, and electrically conductive 2D materials.

1.4.2 Silk and Graphene Nanocomposites

Silk and graphenes have frequently been paired to make robust, electrically conductive, and flexible nanocomposites in the form of films, hydrogels, and aerogels with tunable properties.[5,24] Specifically, the silk can mediate movement of the flakes via effective load transfer through an array of hydrophobic, van der Waals, electrostatic, and hydrogen bonding interactions while providing responsive behavior to external stimuli

such as pH changes, temperature, humidity, etc. to achieve tunable properties.[1] The 2D flakes in these composites typically provide structural stability and electrically conductive properties useful in applications ranging from biosensors to photothermal heating.

Wang et al. reported that silk fibers, which are loaded with traces of CNT and graphene components by directly feeding Bombyx mori larval silkworms with CNT and graphene solutions, demonstrated remarkable mechanical enhancement. Further pyrolyzation of these nanocarbon-loaded silk fibers resulted in carbonized nanocomposites with greatly enhanced electrical conductivity.[90] In some cases, it is suggested the interfacial interactions between NPs and SF play a dominant role in improved toughness. For example, graphene oxide and silk nanocomposite membranes have been fabricated with varying ratios using the spin assisted layer-by-layer technique. When the volume ratio of GO (0.04 wt% in concentration) reached 23.5%, the tensile modulus, ultimate stress, and toughness of the nanocomposites reached 145 GPa, over 300 MPa, and above 2.2 MJ m^{-3}, respectively, which far exceed other SF-based materials.[24] The extraordinary mechanical properties were ascribed to the interphase reinforcement mechanism in which the complementary heterogeneous surface functionalities of GO and SF made them intimately connect via a dense network of various interactions including hydrogen bonding, polar, and hydrophobic interactions promoting the formation of a strong molecular interphase zone. These ultrathin and ultrarobust GO-SF nanocomposite membranes have the potential application in bio-sensing devices or protective molecular coatings due to the GO provided strength and conductivity and SF provided reinforcement and biocompatibility.

The assembly of SF and GO is vitally important to the mechanical properties of these films.[26] These systems often have a "brick-and-mortar"[91] structure inspired by nature

where the GO serves as the strong "bricks" and the silk is the flexible component that is the "mortar" that connects them. This form has been produced using various methods including vacuum filtration, but layer-by-layer assembly has proven to be best for nanoscale manipulation of structure via deposition of single monolayers of components at a time. Using this method, films with elastic modulus up to 76.8 GPa have been made by improving the interfacial strength of silk and GO via pH manipulation adding ballistic armor to the growing list of applications for these systems.[92]

1.4.3 MXene Nanocomposites

Though new to studies in combination with proteins, few papers have shown MXenes to create electrically tunable[93] and stimuli-responsive electromagnetic interference shielding[94] membranes in combination with various proteins. Mixing of proteins with differing repetitive sequences, inspired by squid sucker ring proteins, with MXene at different ratios has been used to vary solution viscosity for inkjet printing[94] and dry volume for controlling thin film conductivity.[93] These proteins allow for interface mediation between the conductive component with themselves and various substrates while still having high conductivity. Surface modification with collagen[95] and polypeptides[93] have allowed for better biocompatibility and solution stability. These studies show MXene as a promising filler in protein nanocomposites for several useful applications.

1.5 Limitations in Bionanocomposites

Designing novel nanocomposites with synthetic and bio-derived components with unique functionalities requires fundamental understanding of system organization and how

it affects overall performance. There have been numerous studies of the combination of synthetic and natural components for functional nanocomposites but these materials haven't achieved theoretical functionalities and mechanical properties.[1] This gap is caused by a distinct lack of understanding of the complicated interactions, mechanisms, and organization driving the performance of these materials.

1.6 References

(1) Xiong, R.; Grant, A. M.; Ma, R.; Zhang, S.; Tsukruk, V. V. Naturally-Derived Biopolymer Nanocomposites: Interfacial Design, Properties and Emerging Applications. *Materials Science and Engineering R: Reports* **2018**, *125*, 1–41. https://doi.org/10.1016/j.mser.2018.01.002.

(2) Guin, T.; Stevens, B.; Krecker, M.; D'Angelo, J.; Humood, M.; Song, Y.; Smith, R.; Polycarpou, A.; Grunlan, J. C. Ultrastrong, Chemically Resistant Reduced Graphene Oxide-Based Multilayer Thin Films with Damage Detection Capability. *ACS Applied Materials and Interfaces* **2016**, *8* (9), 6229–6235. https://doi.org/10.1021/acsami.5b12596.

(3) Savchak, M.; Borodinov, N.; Burtovyy, R.; Anayee, M.; Hu, K.; Ma, R.; Grant, A.; Li, H.; Cutshall, D. B.; Wen, Y.; Koley, G.; Harrell, W. R.; Chumanov, G.; Tsukruk, V.; Luzinov, I. Highly Conductive and Transparent Reduced Graphene Oxide Nanoscale Films via Thermal Conversion of Polymer-Encapsulated Graphene Oxide Sheets. *ACS Applied Materials and Interfaces* **2018**, *10* (4), 3975–3985. https://doi.org/10.1021/acsami.7b16500.

(4) Xiong, R.; Kim, H. S.; Zhang, L.; Korolovych, V. F.; Zhang, S.; Yingling, Y. G.; Tsukruk, V. V. Wrapping Nanocellulose Nets around Graphene Oxide Sheets. *Angewandte Chemie - International Edition* **2018**, *57* (28), 8508–8513. https://doi.org/10.1002/anie.201803076.

(5) Yin, Y.; Hu, K.; Grant, A. M.; Zhang, Y.; Tsukruk, V. V. Biopolymeric Nanocomposites with Enhanced Interphases. *Langmuir* **2015**, *31* (39), 10859–10870. https://doi.org/10.1021/acs.langmuir.5b02744.

(6) Wegst, U. G. K.; Bai, H.; Saiz, E.; Tomsia, A. P.; Ritchie, R. O. Bioinspired Structural Materials. *Nature Materials* **2015**, *14* (1), 23–36. https://doi.org/10.1038/nmat4089.

(7) Gosline, J. M.; Guerette, P. A.; Ortlepp, C. S.; Savage, K. N. The Mechanical Design of Spider Silks: From Fibroin Sequence to Mechanical Function. *J. Exp. Biol.* **1999**, *202* (Pt 23), 3295–3303.

(8) Klemm, D.; Kramer, F.; Moritz, S.; Lindström, T.; Ankerfors, M.; Gray, D.; Dorris, A. Nanocelluloses: A New Family of Nature-Based Materials. *Angewandte Chemie International Edition* **2011**, *50* (24), 5438–5466.

(9) Abba, M. T.; Hunger, P. M.; Kalidindi, S. R.; Wegst, U. G. K. Nacre-like Hybrid Films: Structure, Properties, and the Effect of Relative Humidity. *Journal of the Mechanical Behavior of Biomedical Materials* **2015**, *55*, 140–150. https://doi.org/10.1016/j.jmbbm.2015.10.013.

(10) Murphy, A. R.; Kaplan, D. L. Biomedical Applications of Chemically-Modified Silk Fibroin. *J. Mater. Chem.* **2009**, *19* (36), 6443–6450. https://doi.org/10.1039/B905802H.

(11) Jin, H.-J.; Kaplan, D. L. Mechanism of Silk Processing in Insects and Spiders. *Nature* **2003**, *424* (6952), 1057–1061. https://doi.org/10.1038/nature01809.

(12) Buck, C. C.; Dennis, P. B.; Gupta, M. K.; Grant, M. T.; Crosby, M. G.; Slocik, J. M.; Mirau, P. A.; Becknell, K. A.; Comfort, K. K.; Naik, R. R. Anion-Mediated Effects on the Size and Mechanical Properties of Enzymatically Crosslinked Suckerin Hydrogels. *Macromolecular Bioscience* **2019**, *19* (3). https://doi.org/10.1002/mabi.201800238.

(13) Guerette, P. A.; Hoon, S.; Ding, D.; Amini, S.; Masic, A.; Ravi, V.; Venkatesh, B.; Weaver, J. C.; Miserez, A. Nanoconfined β-Sheets Mechanically Reinforce the Supra-Biomolecular Network of Robust Squid Sucker Ring Teeth. *ACS Nano* **2014**, *8* (7), 7170–7179. https://doi.org/10.1021/nn502149u.

(14) Dreyer, D. R.; Park, S.; Bielawski, C. W.; Ruoff, R. S. The Chemistry of Graphene Oxide. *Chemical Society Reviews* **2010**, *39* (1), 228–240. https://doi.org/10.1039/b917103g.

(15) Ding, L.; Wei, Y.; Li, L.; Zhang, T.; Wang, H.; Xue, J.; Ding, L.-X.; Wang, S.; Caro, J.; Gogotsi, Y. MXene Molecular Sieving Membranes for Highly Efficient Gas Separation. *Nature Communications* **2018**, *9* (1). https://doi.org/10.1038/s41467-017-02529-6.

(16) Omenetto, F. G.; Kaplan, D. L. New Opportunities for an Ancient Material. *Science* **2010**, *329* (5991), 528–531. https://doi.org/10.1126/science.1188936.

(17) Keten, S.; Xu, Z.; Ihle, B.; Buehler, M. J. Nanoconfinement Controls Stiffness, Strength and Mechanical Toughness of Beta-Sheet Crystals in Silk. *Nat Mater* **2010**, *9* (4), 359–367. https://doi.org/10.1038/nmat2704.

(18) Inoue, S.; Tanaka, K.; Arisaka, F.; Kimura, S.; Ohtomo, K.; Mizuno, S. Silk Fibroin of Bombyx Mori Is Secreted, Assembling a High Molecular Mass Elementary Unit Consisting of H-Chain, L-Chain, and P25, with a 6:6:1 Molar Ratio. *J. Biol. Chem.* **2000**, *275* (51), 40517–40528. https://doi.org/10.1074/jbc.M006897200.

(19) Grant, A. M.; Kim, H. S.; Dupnock, T. L.; Hu, K.; Yingling, Y. G.; Tsukruk, V. V. Silk Fibroin–Substrate Interactions at Heterogeneous Nanocomposite Interfaces. *Advanced Functional Materials* **2016**, *26* (35), 6380–6392. https://doi.org/10.1002/adfm.201601268.

(20) Koebley, S. R.; Thorpe, D.; Pang, P.; Chrisochoides, P.; Greving, I.; Vollrath, F.; Schniepp, H. C. Silk Reconstitution Disrupts Fibroin Self-Assembly. *Biomacromolecules* **2015**, *16* (9), 2796–2804. https://doi.org/10.1021/acs.biomac.5b00732.

(21) Tao, H.; Kaplan, D. L.; Omenetto, F. G. Silk Materials - A Road to Sustainable High Technology. *Advanced Materials* **2012**, *24* (21), 2824–2837. https://doi.org/10.1002/adma.201104477.

(22) Ayutsede, J.; Gandhi, M.; Sukiraga, S.; Ye, H.; Hsu, C.-M.; Gogotsi, Y.; Ko, F. Carbon Nanotube Reinforced Bombyx Mori Silk Nanofibers by the Electrospinning Process. *Biomacromolecules* **2006**, *7* (1), 208–214. https://doi.org/10.1021/bm0505888.

(23) Koh, L.-D.; Cheng, Y.; Teng, C.-P.; Khin, Y.-W.; Loh, X.-J.; Tee, S.-Y.; Low, M.; Ye, E.; Yu, H.-D.; Zhang, Y.-W.; Han, M.-Y. Structures, Mechanical Properties and Applications of Silk Fibroin Materials. *Progress in Polymer Science* **2015**, *46*, 86–110. https://doi.org/10.1016/j.progpolymsci.2015.02.001.

(24) Hu, K.; Gupta, M. K.; Kulkarni, D. D.; Tsukruk, V. V. Ultra-Robust Graphene Oxide-Silk Fibroin Nanocomposite Membranes. *Advanced Materials* **2013**, *25* (16), 2301–2307. https://doi.org/10.1002/adma.201300179.

(25) Zhu, B.; Wang, H.; Leow, W. R.; Cai, Y.; Loh, X. J.; Han, M.-Y.; Chen, X. Silk Fibroin for Flexible Electronic Devices. *Advanced Materials* **2016**, *28* (22), 4250–4265. https://doi.org/10.1002/adma.201504276.

(26) Wang, Y.; Ma, R.; Hu, K.; Kim, S.; Fang, G.; Shao, Z.; Tsukruk, V. V. Dramatic Enhancement of Graphene Oxide/Silk Nanocomposite Membranes: Increasing Toughness and Strength via Annealing of Interfacial Structures. *ACS Appl. Mater. Interfaces* **2016**. https://doi.org/10.1021/acsami.6b08610.

(27) Demirel, M. C.; Cetinkaya, M.; Pena-Francesch, A.; Jung, H. Recent Advances in Nanoscale Bioinspired Materials. *Macromolecular Bioscience* **2015**, *15* (3), 300–311. https://doi.org/10.1002/mabi.201400324.

(28) Miserez, A.; Weaver, J. C.; Pedersen, P. B.; Schneeberk, T.; Hanlon, R. T.; Kisailus, D.; Birkedal, H. Microstructural and Biochemical Characterization of the Nanoporous Sucker Rings from Dosidicus Gigas. *Advanced Materials* **2009**, *21* (4), 401–406. https://doi.org/10.1002/adma.200801197.

(29) Broomell, C. C.; Khan, R. K.; Moses, D. N.; Miserez, A.; Pontin, M. G.; Stucky, G. D.; Zok, F. W.; Waite, J. H. Mineral Minimization in Nature's Alternative Teeth. *Journal of the Royal Society Interface* **2007**, *4* (12), 19–31. https://doi.org/10.1098/rsif.2006.0153.

(30) Guerette, P. A.; Hoon, S.; Seow, Y.; Raida, M.; Masic, A.; Wong, F. T.; Ho, V. H. B.; Kong, K. W.; Demirel, M. C.; Pena-Francesch, A.; Amini, S.; Tay, G. Z.; Ding, D.; Miserez, A. Accelerating the Design of Biomimetic Materials by Integrating RNA-Seq with Proteomics and Materials Science. *Nature Biotechnology* **2013**, *31* (10), 908–915. https://doi.org/10.1038/nbt.2671.

(31) Miserez, A.; Weaver, J. C.; Chaudhuri, O. Biological Materials and Molecular Biomimetics-Filling up the Empty Soft Materials Space for Tissue Engineering Applications. *Journal of Materials Chemistry B* **2015**, *3* (1), 15–24. https://doi.org/10.1039/c4tb01267d.

(32) Mu, Y.; Tang, B.; Yu, M. Length-Dependent β-Sheet Growth Mechanisms of Polyalanine Peptides in Water and on Hydrophobic Surfaces. *Physical Review E - Statistical, Nonlinear, and Soft Matter Physics* **2014**, *89* (3). https://doi.org/10.1103/PhysRevE.89.032711.

(33) *2D Metal Carbides and Nitrides (MXenes): Structure, Properties and Applications*; Anasori, B., Gogotsi, Y., Eds.; Springer International Publishing, 2019. https://doi.org/10.1007/978-3-030-19026-2.

(34) Zhang, C. J.; Pinilla, S.; McEvoy, N.; Cullen, C. P.; Anasori, B.; Long, E.; Park, S.-H.; Seral-Ascaso, A.; Shmeliov, A.; Krishnan, D.; Morant, C.; Liu, X.; Duesberg, G. S.; Gogotsi, Y.; Nicolosi, V. Oxidation Stability of Colloidal Two-Dimensional Titanium Carbides (MXenes). *Chemistry of Materials* **2017**, *29* (11), 4848–4856. https://doi.org/10.1021/acs.chemmater.7b00745.

(35) Miró, P.; Audiffred, M.; Heine, T. An Atlas of Two-Dimensional Materials. *Chemical Society Reviews* **2014**, *43* (18), 6537–6554. https://doi.org/10.1039/c4cs00102h.

(36) Gupta, A.; Sakthivel, T.; Seal, S. Recent Development in 2D Materials beyond Graphene. *Progress in Materials Science* **2015**, *73*, 44–126. https://doi.org/10.1016/j.pmatsci.2015.02.002.

(37) Nicolosi, V.; Chhowalla, M.; Kanatzidis, M. G.; Strano, M. S.; Coleman, J. N. Liquid Exfoliation of Layered Materials. *Science* **2013**, *340* (6139), 1226419. https://doi.org/10.1126/science.1226419.

(38) Naguib, M.; Mashtalir, O.; Carle, J.; Presser, V.; Lu, J.; Hultman, L.; Gogotsi, Y.; Barsoum, M. W. Two-Dimensional Transition Metal Carbides. *ACS Nano* **2012**, *6* (2), 1322–1331. https://doi.org/10.1021/nn204153h.

(39) Suk, J. W.; Piner, R. D.; An, J.; Ruoff, R. S. Mechanical Properties of Monolayer Graphene Oxide. *ACS Nano* **2010**, *4* (11), 6557–6564. https://doi.org/10.1021/nn101781v.

(40) Xiong, R.; Hu, K.; Grant, A. M.; Ma, R.; Xu, W.; Lu, C.; Zhang, X.; Tsukruk, V. V. Ultrarobust Transparent Cellulose Nanocrystal-Graphene Membranes with High Electrical Conductivity. *Advanced Materials* **2016**, *28* (7), 1501–1509. https://doi.org/10.1002/adma.201504438.

(41) Gogotsi, Y.; Anasori, B. The Rise of MXenes. *ACS Nano* **2019**, *13* (8), 8491–8494. https://doi.org/10.1021/acsnano.9b06394.

(42) Anasori, B.; Lukatskaya, M. R.; Gogotsi, Y. 2D Metal Carbides and Nitrides (MXenes) for Energy Storage. *Nature Reviews Materials* **2017**, *2* (2). https://doi.org/10.1038/natrevmats.2016.98.

(43) Zhang, J.; Kong, N.; Uzun, S.; Levitt, A.; Seyedin, S.; Lynch, P. A.; Qin, S.; Han, M.; Yang, W.; Liu, J.; Wang, X.; Gogotsi, Y.; Razal, J. M. Scalable Manufacturing of Free-Standing, Strong Ti3C2Tx MXene Films with Outstanding Conductivity. *Advanced Materials* **2020**. https://doi.org/10.1002/adma.202001093.

(44) Lipatov, A.; Lu, H.; Alhabeb, M.; Anasori, B.; Gruverman, A.; Gogotsi, Y.; Sinitskii, A. Elastic Properties of 2D Ti 3 C 2 T x MXene Monolayers and Bilayers. *Science Advances* **2018**, *4* (6). https://doi.org/10.1126/sciadv.aat0491.

(45) Lipatov, A.; Alhabeb, M.; Lu, H.; Zhao, S.; Loes, M. J.; Vorobeva, N. S.; Dall'Agnese, Y.; Gao, Y.; Gruverman, A.; Gogotsi, Y.; Sinitskii, A. Electrical and Elastic Properties of Individual Single-Layer Nb4C3Tx MXene Flakes. *Advanced Electronic Materials* **2020**, *6* (4). https://doi.org/10.1002/aelm.201901382.

(46) Hantanasirisakul, K.; Alhabeb, M.; Lipatov, A.; Maleski, K.; Anasori, B.; Salles, P.; Ieosakulrat, C.; Pakawatpanurut, P.; Sinitskii, A.; May, S. J.; Gogotsi, Y. Effects of Synthesis and Processing on Optoelectronic Properties of Titanium Carbonitride MXene. *Chemistry of Materials* **2019**, *31* (8), 2941–2951. https://doi.org/10.1021/acs.chemmater.9b00401.

(47) Sarycheva, A.; Polemi, A.; Liu, Y.; Dandekar, K.; Anasori, B.; Gogotsi, Y. 2D Titanium Carbide (MXene) for Wireless Communication. *Science Advances* **2018**, *4* (9). https://doi.org/10.1126/sciadv.aau0920.

(48) Hart, J. L.; Hantanasirisakul, K.; Lang, A. C.; Anasori, B.; Pinto, D.; Pivak, Y.; van Omme, J. T.; May, S. J.; Gogotsi, Y.; Taheri, M. L. Control of MXenes' Electronic Properties through Termination and Intercalation. *Nature Communications* **2019**, *10* (1). https://doi.org/10.1038/s41467-018-08169-8.

(49) Naguib, M.; Mochalin, V. N.; Barsoum, M. W.; Gogotsi, Y. 25th Anniversary Article: MXenes: A New Family of Two-Dimensional Materials. *Advanced Materials* **2014**, *26* (7), 992–1005. https://doi.org/10.1002/adma.201304138.

(50) Wang, H.-W.; Naguib, M.; Page, K.; Wesolowski, D. J.; Gogotsi, Y. Resolving the Structure of Ti3C2Tx MXenes through Multilevel Structural Modeling of the Atomic Pair Distribution Function. *Chemistry of Materials* **2016**, *28* (1), 349–359. https://doi.org/10.1021/acs.chemmater.5b04250.

(51) Alhabeb, M.; Maleski, K.; Anasori, B.; Lelyukh, P.; Clark, L.; Sin, S.; Gogotsi, Y. Guidelines for Synthesis and Processing of Two-Dimensional Titanium Carbide (Ti 3 C 2 T x MXene). *Chemistry of Materials* **2017**, *29* (18), 7633–7644. https://doi.org/10.1021/acs.chemmater.7b02847.

(52) Maleski, K.; Ren, C. E.; Zhao, M.-Q.; Anasori, B.; Gogotsi, Y. Size-Dependent Physical and Electrochemical Properties of Two-Dimensional MXene Flakes. *ACS Applied Materials and Interfaces* **2018**, *10* (29), 24491–24498. https://doi.org/10.1021/acsami.8b04662.

(53) Lipatov, A.; Alhabeb, M.; Lukatskaya, M. R.; Boson, A.; Gogotsi, Y.; Sinitskii, A. Effect of Synthesis on Quality, Electronic Properties and Environmental Stability of Individual

Monolayer Ti3C2 MXene Flakes. *Advanced Electronic Materials* **2016**, *2* (12). https://doi.org/10.1002/aelm.201600255.

(54) Yoo, B. M.; Shin, H. J.; Yoon, H. W.; Park, H. B. Graphene and Graphene Oxide and Their Uses in Barrier Polymers. *J. Appl. Polym. Sci.* **2014**, *131* (1), n/a-n/a. https://doi.org/10.1002/app.39628.

(55) Habibi, Y.; Lucia, L. A.; Rojas, O. J. Cellulose Nanocrystals: Chemistry, Self-Assembly, and Applications. *Chem. Rev.* **2010**, *110* (6), 3479–3500. https://doi.org/10.1021/cr900339w.

(56) Yang, Q.; Saito, T.; Berglund, L. A.; Isogai, A. Cellulose Nanofibrils Improve the Properties of All-Cellulose Composites by the Nano-Reinforcement Mechanism and Nanofibril-Induced Crystallization. *Nanoscale* **2015**, *7* (42), 17957–17963. https://doi.org/10.1039/C5NR05511C.

(57) Barthelat, F.; Yin, Z.; Buehler, M. J. Structure and Mechanics of Interfaces in Biological Materials. *Nature Reviews Materials* **2016**, *1*, 16007.

(58) Wicklein, B.; Kocjan, A.; Salazar-Alvarez, G.; Carosio, F.; Camino, G.; Antonietti, M.; Bergström, L. Thermally Insulating and Fire-Retardant Lightweight Anisotropic Foams Based on Nanocellulose and Graphene Oxide. *Nat Nano* **2015**, *10* (3), 277–283. https://doi.org/10.1038/nnano.2014.248.

(59) Moon, R. J.; Martini, A.; Nairn, J.; Simonsen, J.; Youngblood, J. Cellulose Nanomaterials Review: Structure, Properties and Nanocomposites. *Chemical Society Reviews* **2011**, *40* (7), 3941–3994.

(60) Campos, J. M.; Ferraria, A. M.; Botelho do Rego, A. M.; Ribeiro, M. R.; Barros-Timmons, A. Studies on PLA Grafting onto Graphene Oxide and Its Effect on the Ensuing Composite Films. *Materials Chemistry and Physics* **2015**, *166*, 122–132. https://doi.org/10.1016/j.matchemphys.2015.09.036.

(61) Wegst, U. G. K.; Bai, H.; Saiz, E.; Tomsia, A. P.; Ritchie, R. O. Bioinspired Structural Materials. *Nat Mater* **2015**, *14* (1), 23–36. https://doi.org/10.1038/nmat4089.

(62) Iwamoto, S.; Kai, W.; Isogai, A.; Iwata, T. Elastic Modulus of Single Cellulose Microfibrils from Tunicate Measured by Atomic Force Microscopy. *Biomacromolecules* **2009**, *10* (9), 2571–2576.

(63) Sydney Gladman, A.; Matsumoto, E. A.; Nuzzo, R. G.; Mahadevan, L.; Lewis, J. A. Biomimetic 4D Printing. *Nat Mater* **2016**, *15* (4), 413–418. https://doi.org/10.1038/nmat4544.

(64) Uddin, M. E.; Layek, R. K.; Kim, H. Y.; Kim, N. H.; Hui, D.; Lee, J. H. Preparation and Enhanced Mechanical Properties of Non-Covalently-Functionalized Graphene Oxide/Cellulose Acetate Nanocomposites. *Composites Part B: Engineering* **2016**, *90*, 223–231. https://doi.org/10.1016/j.compositesb.2015.12.008.

(65) Zhu, H.; Luo, W.; Ciesielski, P. N.; Fang, Z.; Zhu, J. Y.; Henriksson, G.; Himmel, M. E.; Hu, L. Wood-Derived Materials for Green Electronics, Biological Devices, and Energy Applications. *Chemical Reviews* **2016**.

(66) Hu, K.; Kulkarni, D. D.; Choi, I.; Tsukruk, V. V. Graphene-Polymer Nanocomposites for Structural and Functional Applications. *Progress in Polymer Science* **2014**, *39* (11), 1934–1972. https://doi.org/10.1016/j.progpolymsci.2014.03.001.

(67) Hummers Jr, W. S.; Offeman, R. E. Preparation of Graphitic Oxide. *Journal of the American Chemical Society* **1958**, *80* (6), 1339–1339.

(68) Steed, J. W.; Atwood, J. L. *Supramolecular Chemistry*; John Wiley & Sons, 2013.

(69) Christian Kemp, K.; Cho, Y.; Chandra, V.; Kim, K. S. Noncovalent Functionalization of Graphene. In *Functionalization of Graphene*; Georgakilas, V., Ed.; Wiley-VCH Verlag GmbH & Co. KGaA, 2014; pp 199–218.

(70) Long, B.; Manning, M.; Burke, M.; Szafranek, B. N.; Visimberga, G.; Thompson, D.; Greer, J. C.; Povey, I. M.; MacHale, J.; Lejosne, G.; Neumaier, D.; Quinn, A. J. Non-Covalent Functionalization of Graphene Using Self-Assembly of Alkane-Amines. *Adv. Funct. Mater.* **2012**, *22* (4), 717–725. https://doi.org/10.1002/adfm.201101956.

(71) Wang, H.; Maiyalagan, T.; Wang, X. Review on Recent Progress in Nitrogen-Doped Graphene: Synthesis, Characterization, and Its Potential Applications. *Acs Catalysis* **2012**, *2* (5), 781–794.

(72) Joshi, R. K.; Carbone, P.; Wang, F. C.; Kravets, V. G.; Su, Y.; Grigorieva, I. V.; Wu, H. A.; Geim, A. K.; Nair, R. R. Precise and Ultrafast Molecular Sieving Through Graphene Oxide Membranes. *Science* **2014**, *343* (6172), 752–754. https://doi.org/10.1126/science.1245711.

(73) Rein, M.; Richter, N.; Parvez, K.; Feng, X.; Sachdev, H.; Kläui, M.; Müllen, K. Magnetoresistance and Charge Transport in Graphene Governed by Nitrogen Dopants. *ACS nano* **2015**, *9* (2), 1360–1366.

(74) Cheng, C.; Jiang, G.; Garvey, C. J.; Wang, Y.; Simon, G. P.; Liu, J. Z.; Li, D. Ion Transport in Complex Layered Graphene-Based Membranes with Tuneable Interlayer Spacing. *Science advances* **2016**, *2* (2), e1501272.

(75) Liu, J.; Cui, L.; Losic, D. Graphene and Graphene Oxide as New Nanocarriers for Drug Delivery Applications. *Acta Biomaterialia* **2013**, *9* (12), 9243–9257. https://doi.org/10.1016/j.actbio.2013.08.016.

(76) Compton, O. C.; Cranford, S. W.; Putz, K. W.; An, Z.; Brinson, L. C.; Buehler, M. J.; Nguyen, S. T. Tuning the Mechanical Properties of Graphene Oxide Paper and Its Associated Polymer Nanocomposites by Controlling Cooperative Intersheet Hydrogen Bonding. *ACS Nano* **2012**, *6* (3), 2008–2019. https://doi.org/10.1021/nn202928w.

(77) Kawai, S.; Benassi, A.; Gnecco, E.; Söde, H.; Pawlak, R.; Feng, X.; Müllen, K.; Passerone, D.; Pignedoli, C. A.; Ruffieux, P.; others. Superlubricity of Graphene Nanoribbons on Gold Surfaces. *Science* **2016**, *351* (6276), 957–961.

(78) Berman, D.; Erdemir, A.; Sumant, A. V. Few Layer Graphene to Reduce Wear and Friction on Sliding Steel Surfaces. *Carbon* **2013**, *54*, 454–459.

(79) Yang, K.; Feng, L.; Shi, X.; Liu, Z. Nano-Graphene in Biomedicine: Theranostic Applications. *Chem. Soc. Rev.* **2013**, *42* (2), 530–547. https://doi.org/10.1039/C2CS35342C.

(80) Georgakilas, V.; Otyepka, M.; Bourlinos, A. B.; Chandra, V.; Kim, N.; Kemp, K. C.; Hobza, P.; Zboril, R.; Kim, K. S. Functionalization of Graphene: Covalent and Non-Covalent Approaches, Derivatives and Applications. *Chemical reviews* **2012**, *112* (11), 6156–6214.

(81) Yadav, S. K.; Jung, Y. C.; Kim, J. H.; Ko, Y.-I.; Ryu, H. J.; Yadav, M. K.; Kim, Y. A.; Cho, J. W. Mechanically Robust, Electrically Conductive Biocomposite Films Using Antimicrobial Chitosan-Functionalized Graphenes. *Particle and Particle Systems Characterization* **2013**, *30* (8), 721–727. https://doi.org/10.1002/ppsc.201300044.

(82) Jeon, J.-H.; Cheedarala, R. K.; Kee, C.-D.; Oh, I.-K. Dry-Type Artificial Muscles Based on Pendent Sulfonated Chitosan and Functionalized Graphene Oxide for Greatly Enhanced

Ionic Interactions and Mechanical Stiffness. *Adv. Funct. Mater.* **2013**, *23* (48), 6007–6018. https://doi.org/10.1002/adfm.201203550.

(83) Xu, H.; Xie, L.; Wu, D.; Hakkarainen, M. Immobilized Graphene Oxide Nanosheets as Thin but Strong Nanointerfaces in Biocomposites. *ACS Sustainable Chemistry and Engineering* **2016**, *4* (4), 2211–2222. https://doi.org/10.1021/acssuschemeng.5b01703.

(84) Nie, L.; Liu, C.; Wang, J.; Shuai, Y.; Cui, X.; Liu, L. Effects of Surface Functionalized Graphene Oxide on the Behavior of Sodium Alginate. *Carbohydr Polym* **2015**, *117*, 616–623. https://doi.org/10.1016/j.carbpol.2014.08.104.

(85) Zhang, X.; Wang, H.; Hu, R.; Huang, C.; Zhong, W.; Pan, L.; Feng, Y.; Qiu, T.; Zhang, C. J.; Yang, J. Novel Solvothermal Preparation and Enhanced Microwave Absorption Properties of Ti 3 C 2 T x MXene Modified by in Situ Coated Fe 3 O 4 Nanoparticles. *Applied Surface Science* **2019**, *484*, 383–391. https://doi.org/10.1016/j.apsusc.2019.03.264.

(86) Zhao, K.; Wang, H.; Zhu, C.; Lin, S.; Xu, Z.; Zhang, X. Free-Standing MXene Film Modified by Amorphous FeOOH Quantum Dots for High-Performance Asymmetric Supercapacitor. *Electrochimica Acta* **2019**, *308*, 1–8. https://doi.org/10.1016/j.electacta.2019.03.225.

(87) Richardson, J. J.; Björnmalm, M.; Caruso, F. Technology-Driven Layer-by-Layer Assembly of Nanofilms. *Science* **2015**, *348* (6233). https://doi.org/10.1126/science.aaa2491.

(88) Hu, K.; Tsukruk, V. V. Tuning the Electronic Properties of Robust Bio-Bond Graphene Papers by Spontaneous Electrochemical Reduction: From Insulators to Flexible Semi-Metals. *Chemistry of Materials* **2015**, *27* (19), 6717–6729. https://doi.org/10.1021/acs.chemmater.5b02750.

(89) Wang, J.; Cheng, Q.; Lin, L.; Jiang, L. Synergistic Toughening of Bioinspired Poly(Vinyl Alcohol)-Clay- Nanofibrillar Cellulose Artificial Nacre. *ACS Nano* **2014**, *8* (3), 2739–2745. https://doi.org/10.1021/nn406428n.

(90) Wang, Q.; Wang, C.; Zhang, M.; Jian, M.; Zhang, Y. Feeding Single-Walled Carbon Nanotubes or Graphene to Silkworms for Reinforced Silk Fibers. *Nano Letters* **2016**, *16* (10), 6695–6700. https://doi.org/10.1021/acs.nanolett.6b03597.

(91) Tang, Z.; Kotov, N. A.; Magonov, S.; Ozturk, B. Nanostructured Artificial Nacre. *Nature Materials* **2003**, *2* (6), 413–418. https://doi.org/10.1038/nmat906.

(92) Xie, W.; Tadepalli, S.; Park, S. H.; Kazemi-Moridani, A.; Jiang, Q.; Singamaneni, S.; Lee, J.-H. Extreme Mechanical Behavior of Nacre-Mimetic Graphene-Oxide and Silk Nanocomposites. *Nano Letters* **2018**, *18* (2), 987–993. https://doi.org/10.1021/acs.nanolett.7b04421.

(93) Vural, M.; Zhu, H.; Pena-Francesch, A.; Jung, H.; Allen, B. D.; Demirel, M. C. Self-Assembly of Topologically Networked Protein- -Ti3C2Tx MXene Composites. *ACS Nano* **2020**. https://doi.org/10.1021/acsnano.0c01431.

(94) Vural, M.; Pena-Francesch, A.; Bars-Pomes, J.; Jung, H.; Gudapati, H.; Hatter, C. B.; Allen, B. D.; Anasori, B.; Ozbolat, I. T.; Gogotsi, Y.; Demirel, M. C. Inkjet Printing of Self-Assembled 2D Titanium Carbide and Protein Electrodes for Stimuli-Responsive Electromagnetic Shielding. *Advanced Functional Materials* **2018**, *28* (32), 1801972. https://doi.org/10.1002/adfm.201801972.

(95) Rozmysłowska-Wojciechowska, A.; Szuplewska, A.; Wojciechowski, T.; Poźniak, S.; Mitrzak, J.; Chudy, M.; Ziemkowska, W.; Chlubny, L.; Olszyna, A.; Jastrzębska, A. M. A Simple, Low-Cost and Green Method for Controlling the Cytotoxicity of MXenes. *Materials Science and Engineering C* **2020**, *111*. https://doi.org/10.1016/j.msec.2020.110790.

CHAPTER 2. GOALS, OBJECTIVES, AND ORGANIZATION AND COMPOSITION OF DISSERTATION

2.1 Research Goals

The goal of this research is to understand the fundamental mechanisms of organization of proteins when co-assembled with two-dimensional synthetic flakes and leverage the components in ordered, mechanically strong, chemically stable, and functional bionanocomposites by manipulating the interfacial interactions and organization of bio-derived components (Figure 2.1). This can be broken into multiple smaller goals to (1) *understand the interfacial interactions* between components in protein-based functional nanocomposites by studying the influences of secondary structure, morphology, and organization on 2D MXenes and silk fibroin, (2) *fabricate mechanically enhanced multilayered* MXene composites by varying concentration and secondary structure of biomacromolecules elucidated in previous studies for bulk materials, (3) apply the fundamental knowledge gained from the model study to investigate the combination of MXene and a novel protein, suckerin-12.

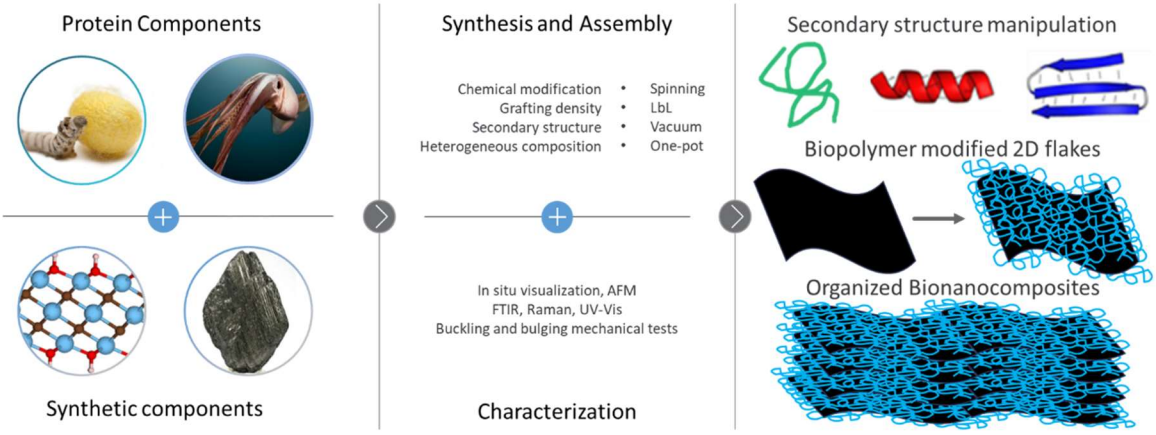

Figure 2.1. Schematic showing material components and research plan.

2.2 Technical Objectives

In this research, two important mechanically robust proteins (silk fibroin and suckerin-12) with tunable secondary structures are assembled with two-dimensional synthetic $Ti_3C_2T_x$ MXenes and used to form multilayered composites with tunable properties. The goals of this research are realized through the following specific tasks:

- Modifying the surface of MXene flakes with silk fibroin and investigating the effects of time and local chemical environment on the biopolymer secondary structure as mediated by direct attachment to a synthetic substrate.
- Fabricating microscale and nanoscale organized composite thin films through vacuum filtration to assemble the materials into the hierarchical organizations of nanocomposites and investigating the resulting enhanced molecular sieving and mechanical performance.
- Use chemical modification techniques founded in previous tasks to modify the surface of MXene with the less studied suckerin-12 protein and elucidate structural changes resulting from exposure to differing salt environments in an effort to determine the possibility mechanically tunable composites.

A model system of silk fibroin and MXene was used to advance these objectives. First, silk fibroin was adhered to the surface of the MXene, and secondary structure change was investigated in response to time and temperature. The components were then used to form bulk multilayered composites with varying ratios of to determine the relationship between secondary structural changes and mechanical properties. The information gleaned from this model system was leveraged in a new system to study

the newer less-understood protein, suckerin-12, in conjunction with MXene. This dissertation provides knowledge on fundamental processes of organization of two protein systems in combination with synthetic MXene and provides techniques for which future scientists may use to similarly investigate new materials.

2.3 Organization and Composition of Dissertation

Chapter 1 introduces the component materials used in this work and a critical review of the assembly and limitations of bionanocomposites.

Chapter 2 outlines the research goals and technical objectives of the studies in this dissertation and provides brief descriptions of the chapters presented.

Chapter 3 describes the experimental techniques used in the studies composing this dissertation. It includes details of methods of synthesis, processing, and characterization of the materials presented.

Chapter 4 reports that $Ti_3C_2T_x$ MXene flakes can be co-assembled with recombinant silk fibroin in aqueous suspensions with silk fibroin nanolayers uniformly covering individual flakes. These bioencapsulated flakes evolve with time due to the gradual growth of silk bundles having β-sheet secondary organization with unique nanofibrillar morphologies extending across flake edges and forming long fringes around individual MXene flakes. This spontaneous reorganization of recombinant silk suggests surface template-initiated formation of intramolecular hydrogen bonding of silk backbones assisted by intermolecular electrostatic and hydrogen bonding with the MXene flake. The formation of dense and hydrophobic β-sheets results in development of a protective shell that hinders the surface

oxidation of Ti3C2Tx in colloidal solution in water and significantly extends the storage life of the individual MXene flakes. Moreover, assembly into organized laminated composites with individual bioencapsulated flakes tightly interconnected via biopolymer bundles and hairs produces robust freestanding electrically conductive membranes with enhanced transport properties.

Chapter 5 presents extended studies on the system described in chapter 4 including micro- and macro-mechanical properties of the hybrid material. Micrometer thick films produced from amorphous silk encapsulated MXene flakes display moduli and ultimate stress of 22.6 ± 3.9 GPa and 109.2 ± 56.9 MPa, respectively, that is double the values of pristine MXene film. Multilayered composites made from simple mixing of silk and MXene at different weight compositions reveal that adding amounts of silk as small as 2.5 wt% can increase the extensibility of the composites. Moreover, manipulation of incubation temperature and time can be used to include secondary structure changes in the templated assembly of attached silk fibroin.

Chapter 6 displays studies on the secondary structure changes of the silk-like protein, suckerin-12, brought on by concentration and deposition differences as well as exposure to kosmotropic salt solutions. Using techniques founded in chapter 4, suckerin-12 encapsulated MXene was fabricated. The morphology of this new system was manipulated via salt exposure and investigated using high resolution AFM.

Chapter 7 is a summary of the results and general conclusions gained from the studies presented in chapters 4-6. Also discussed is the broader impact of the work in this

dissertation on the scientific community and possible applications and studies based on the work.

CHAPTER 3. EXPERIMENTAL DETAILS

3.1 Synthesis, Assembly, and Processing

3.1.1 Synthesis of 2D $Ti_3C_2T_x$

Two-dimensional $Ti_3C_2T_x$ MXenes were supplied by Prof. Yury Gogotsi's group (MSE, Drexel University) and synthesized following the previously reported "clay method."[1,2] First, 20 mL of 9M hydrochloric acid (HCl) was mixed with 2 g of lithium fluoride (LiF), to produce *in-situ* HF required for etching the Ti_3AlC_2 MAX phase precursor. Then, 2 g of Ti_3AlC_2 MAX phase was slowly added to the etchant solution and magnetically stirred for 24 h at 35°C at 400 rpm. The resultant suspension was then split into two 50 mL centrifuge tubes and dispersed in 40 - 45 mL of deionized (DI) water. The mixture was then centrifuged at 3500 rpm for 2 - 3 min and the clear supernatant was decanted. This process was repeated until reaching neutral pH. Sediment containing multilayer MXene and residual MAX phase was then dispersed in 18 MΩm Millipore water, hand shaken, and centrifuged at 3500 rpm for 1 hour. The resulting supernatant containing single- and few-layer MXene flakes of 1.6 ± 0.1 nm average height and lateral size around 1 μm (0.4 – 1.8 μm) was collected and used for SFMX dispersion and the sediment was frozen and kept for future use.

3.1.2 Preparation of Silk Fibroin Solution

Solutions of silk fibroin were prepared mostly via previously studied methods.[3] Silk cocoons were cut into small pieces and placed into a bath of boiling sodium carbonate for 30 min to remove the sericin coating. The silk was then rinsed in deionized (DI) water three

times for 20 minutes each. Approximately 0.5 g of dried silk was dissolved in 4.5 mL of 9.4 M lithium bromide solution (made with Millipore water) and placed in an oven for 30 minutes at 80 °C. The resulting solution was allowed to cool, centrifuged at 6000 rpm for 10 minutes to remove impurities and placed into a 10,000 MW cutoff dialysis cassette. The cassette was placed into 2 L of Millipore water and stirred gently for 15 minutes before the water was removed and replaced with clean water. This was repeated for longer periods of time until the water was changed six times over the course of 24 hours. The resulting solution was kept at 4°C to prevent premature aggregation or for fast fibril formation and used within a month of preparation.

3.1.3 Preparation of Silk-Encapsulated MXene

The concentrations of all silk and initial MXene suspensions were determined by measuring out 200 μL of solution in aluminum weigh boats. Once dry, the boats were measured again to obtain dry weight per cent. Newer MXene suspension concentrations were henceforth determined via comparison with a previously measured suspension of known MXene concentration. The two components were mixed in water for 30 minutes at an 8:1 silk to MXene weight percent ratio and then rinsed via centrifugation to remove unbound silk, leaving silk modified MXene (SFMX). To limit MXene oxidation, the dispersion of SFMX was refrigerated at a temperature of 4 °C for future use. The SFMX dispersions were diluted to 0.1 wt%, 0.05 wt%, and 0.01 wt% AFM and XPS, FTIR, and UV-Vis measurements, respectively. SFMX films were also prepared via vacuum assisted filtration to investigate its ability to self-assemble into ordered structures.

3.1.4 Membrane fabrication via vacuum assisted filtration

Vacuum filtration of aqueous mixtures over nanoporous membranes was used to create ordered bionanocomposites containing modified 2D flakes. This technique works well for aqueous dispersions of 2D materials due to concentration induced alignment.[5,6] As the vacuum pulls solution, the concentration of the dispersion increases causing 2D flakes to order horizontally before drying resulting in ordered laminated composites. Solutions were diluted to 0.02 mg mL^{-1} and 0.5 mg mL^{-1} and vacuum filtered over track-etched polycarbonate filters (200 nm pore size, 47 mm diameter; Whatman) supported by similar nylon filters to make 9.62 cm^2 area films for dye filtration and mechanical testing, respectively. Films used for tensile testing were peeled off the substrate, placed between two glass slides, and dried in vacuum overnight. UV-Vis was used to match MXene concentration of both the pristine MXene and SFMX suspensions to ensure the same amount of MXene was deposited.

3.2 Characterization

3.2.1 High Resolution Atomic Force Microscopy

Atomic force microscopy (AFM) images were obtained on the Veeco Dimension Icon microscope with light tapping mode in air, 512 samples per line, and an aspect ratio of 1 with tips of radius 8 nm and 2 nm for exploratory and high-resolution imaging, respectively.[7] Samples were deposited onto freshly Piranha treated thermally oxidized silicon wafers via spin casting at 3000 rpm for 30 seconds or dropped onto the wafer for one minute and rinsed. The silicon wafers used were cleaned via rinsing in DI water several times, soaking in a Piranha solution of 2:1 sulfuric acid to hydrogen peroxide ratio for 1

hour, and rinsed again with clean water before drying off with an air gun. Heights and roughness of features were analyzed in the NanoScope software via the section or absolute depth function to obtain height histograms of the topography images.

3.2.2 Attenuated Total Reflectance Fourier Transform Infrared Spectroscopy

ATR-FTIR was conducted on a Bruker Vertex 70 spectrometer using crystal substrate for attenuated total reflectance (ATR). To investigate the secondary structures seen in AFM imaging, ATR-FTIR was done on drop cast samples in the range of 4000 – 400 cm^{-1} at a resolution of 4 cm^{-1} with 100 scans per sample and 200 scans per background.[8–10] The resulting spectra were smoothed, background subtracted, and fitted in Origin software using second derivative analysis for 6 peaks in the Amide I region from 1600 cm^{-1} to 1680 cm^{-1} using known peak assignments to account for silk secondary structures of β-sheets, random coils, helices, and turns.[8,9,11]

3.2.3 UV-Vis Spectroscopy

UV-vis spectroscopy measurements were carried out with a Shimadzu UV-3600 Plus Spectrophotometer with a quartz cuvette. Prior to the measurements, a background was taken using water in the same cuvette. For concentration determination measurements, the cuvette was dried with air before the solution was added. All measurements were taken with at medium speed with 0.5 nm intervals from 1000 nm to 180 nm.

3.2.4 X-ray Photoelectron Spectroscopy

XPS was done using a Thermo K-Alpha XPS. Survey spectra were obtained with two scans and high-resolution spectra of titanium, carbon, oxygen, and nitrogen were taken

of each sample with five scans. All spectra were fitted using Origin 8.5 software with the Fit Peaks (Pro) function.

3.2.5 Scanning Electron Microscopy

A Hitachi SU8010 Ultra-High Resolution (1.0 nm) Scanning Electron Microscope FE-SEM was used to view the cross sections of the layered structures. Strips of prepared films were cut to about 3 mm wide using a blade, pulled apart uniaxially by hand, and the newly exposed cross section was imaged.

3.2.6 Conductivity Measurements

Vacuum filtered films were cut into 15 mm by 5 mm strips and measured using the four-point probe method. The four probes, spring loaded to reduce sample damage, were 2.54 mm apart and connected to a Keithley 2400 source meter with 4 wire sense operation. Five measurements were taken, averaged, and used to calculate the conductivity.

3.2.7 Tensile Mechanical Testing

Vacuum assisted filtration fabricated films were cut into 3 mm by 27 mm strips and glued to precut paper substrates dried overnight. The substrates cut into 34 mm X 20 mm pieces and hole punched to have a square were made to have 2.54 cm^2 squares in the center. Samples were placed on a Shimadzu EZ-SX tester machine, the edges of the supports were cut, and the samples were pulled uniaxially at a rate of 1 mm min^{-1} until break. The length and width of the samples were measured individual after each test while SEM imaging was used to determine the thicknesses.

3.2.8 Buckling Mechanical Testing

Since the size of 2D flakes is on the micron scale, buckling must be used to elucidate mechanical properties of single flakes. Flakes are deposited onto acid treated PDMS, imaged using AFM to determine thickness, then compressed 30% and imaged again using AFM.[12] The thickness of the flakes and the distance between wrinkles induced upon compression can be used to calculate the modulus of few to single flakes.[13]

3.3 References

(1) Ghidiu, M.; Lukatskaya, M. R.; Zhao, M.-Q.; Gogotsi, Y.; Barsoum, M. W. Conductive Two-Dimensional Titanium Carbide "clay" with High Volumetric Capacitance. *Nature* **2015**, *516* (7529), 78–81. https://doi.org/10.1038/nature13970.

(2) Alhabeb, M.; Maleski, K.; Anasori, B.; Lelyukh, P.; Clark, L.; Sin, S.; Gogotsi, Y. Guidelines for Synthesis and Processing of Two-Dimensional Titanium Carbide (Ti 3 C 2 T x MXene). *Chemistry of Materials* **2017**, *29* (18), 7633–7644. https://doi.org/10.1021/acs.chemmater.7b02847.

(3) Rockwood, D. N.; Preda, R. C.; Yücel, T.; Wang, X.; Lovett, M. L.; Kaplan, D. L. Materials Fabrication from Bombyx Mori Silk Fibroin. *Nature Protocols* **2011**, *6* (10), 1612–1631. https://doi.org/10.1038/nprot.2011.379.

(4) Yin, Y.; Hu, K.; Grant, A. M.; Zhang, Y.; Tsukruk, V. V. Biopolymeric Nanocomposites with Enhanced Interphases. *Langmuir* **2015**, *31* (39), 10859–10870. https://doi.org/10.1021/acs.langmuir.5b02744.

(5) Xiong, R.; Grant, A. M.; Ma, R.; Zhang, S.; Tsukruk, V. V. Naturally-Derived Biopolymer Nanocomposites: Interfacial Design, Properties and Emerging Applications. *Materials Science and Engineering R: Reports* **2018**, *125*, 1–41. https://doi.org/10.1016/j.mser.2018.01.002.

(6) Hu, K.; Tsukruk, V. V. Tuning the Electronic Properties of Robust Bio-Bond Graphene Papers by Spontaneous Electrochemical Reduction: From Insulators to

Flexible Semi-Metals. *Chemistry of Materials* **2015**, *27* (19), 6717–6729. https://doi.org/10.1021/acs.chemmater.5b02750.

(7) McConney, M. E.; Singamaneni, S.; Tsukruk, V. V. Probing Soft Matter with the Atomic Force Microscopies: Imaging and Force Spectroscopy. *Polymer Reviews* **2010**, *50* (3), 235–286. https://doi.org/10.1080/15583724.2010.493255.

(8) Grant, A. M.; Kim, H. S.; Dupnock, T. L.; Hu, K.; Yingling, Y. G.; Tsukruk, V. V. Silk Fibroin–Substrate Interactions at Heterogeneous Nanocomposite Interfaces. *Advanced Functional Materials* **2016**, *26* (35), 6380–6392. https://doi.org/10.1002/adfm.201601268.

(9) Belton, D. J.; Plowright, R.; Kaplan, D. L.; Perry, C. C. A Robust Spectroscopic Method for the Determination of Protein Conformational Composition – Application to the Annealing of Silk. *Acta Biomaterialia* **2018**, *73*, 355–364. https://doi.org/10.1016/j.actbio.2018.03.058.

(10) Hu, X.; Kaplan, D.; Cebe, P. Determining Beta-Sheet Crystallinity in Fibrous Proteins by Thermal Analysis and Infrared Spectroscopy. *Macromolecules* **2006**, *39* (18), 6161–6170. https://doi.org/10.1021/ma0610109.

(11) Hu, X.; Shmelev, K.; Sun, L.; Gil, E.-S.; Park, S.-H.; Cebe, P.; Kaplan, D. L. Regulation of Silk Material Structure by Temperature-Controlled Water Vapor Annealing. *Biomacromolecules* **2011**, *12* (5), 1686–1696. https://doi.org/10.1021/bm200062a.

(12) Xiong, R.; Kim, H. S.; Zhang, L.; Korolovych, V. F.; Zhang, S.; Yingling, Y. G.; Tsukruk, V. V. Wrapping Nanocellulose Nets around Graphene Oxide Sheets. *Angewandte Chemie - International Edition* **2018**, *57* (28), 8508–8513. https://doi.org/10.1002/anie.201803076.

(13) Iguiñiz, N.; Frisenda, R.; Bratschitsch, R.; Castellanos-Gomez, A. Revisiting the Buckling Metrology Method to Determine the Young's Modulus of 2D Materials. *Advanced Materials* **2019**, *31* (10), 1807150. https://doi.org/10.1002/adma.201807150.

CHAPTER 4. BIO-ENCAPSULATED MXENE FLAKES FOR ENHANCED STABILITY AND COMPOSITE PRECURSORS

4.1 Introduction

Polymer coating or incorporation of $Ti_3C_2T_x$ MXene (Figure 4.1a) into polymer matrices can address issues of environmental stability discussed previously and allow fabrication of robust and stable materials and devices. There have been numerous studies on the combination of these synthetic 2D materials with polymers to create nanocomposites with enhanced mechanical properties, preservation of conductivity, and stable or added functionalities.[1] Specifically, the natural components, such as proteins, polysaccharides, and amino acids, have been explored for various synthetic and bionanocomposites based upon proteins and various 2D functional materials.[2] However, there are very few published research on MXene-biopolymer composites.[3,4] Prior studies on biopolymer-based composites using other 2D materials, specifically graphene oxides, have shown they can be modified in aqueous suspension with various materials including block co-polymers[5] and biomaterials such as cellulose[6] and silk protein.[7]

Understanding the interfaces between the polymer and MXene nanosheets is required for manipulating physical properties of the functional composites. Specifically, the structure of proteins like silk when combined with 2D sheets has proven to be more complicated due to the balance of van der Waals interactions, hydrogen bonding, and electrostatic interference. Herein, we report direct co-assembly of $Ti_3C_2T_x$ MXene flakes with silk fibroins in aqueous suspension with formation of individual flakes tightly encapsulated with biopolymer nanoscale coatings controlled by weak interactions (Figure

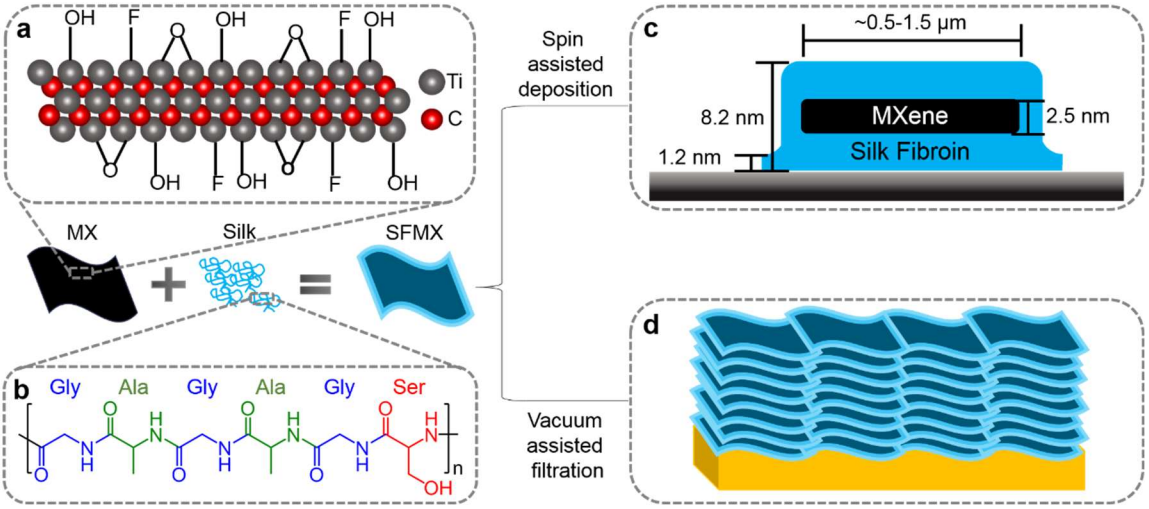

Figure 4.1 Surface modification of MXene flakes with silk fibroin: (a) Single flake of $Ti_3C_2T_x$ MXene with surface functional groups (T_x = O, OH, F) and co-assembly of silk fibroin on flake surfaces; (b) typical amino acid composition of silk backbones.[8,9] (c) Schematic representation of individual encapsulated flake on silicon substrate with parameters derived from high resolution atomic force microscopy (HRAFM) imaging; (d) layered morphology of a thin bio-MXene film assembled via vacuum assisted filtration of SFMX dispersions.

4.1). Due to the similarity of surface pendant groups of these 2D flakes, silk co-assembly can be done on MXene similar to that observed for graphene oxide but with unique features caused by evolution of the silk secondary organization. Indeed, encapsulated MXene flakes show unique nanofibrillar fringes around the flakes that facilitate their improved oxidation stability. Their assembly into freely standing robust laminated bio-nanocomposites with enhanced transport properties and significant electrical conductivity allows for potential applications in energy storage, selective transport and sensing fields.

4.2 Experimental Details

4.2.1 Synthesis of Materials

Two-dimensional $Ti_3C_2T_x$ MXenes and silk fibroin were synthesized according to procedures previously mentioned (Chapter 3). Dispersions of MXene post centrifugation were purged with argon and frozen at -80 °C if not used immediately. Silk fibroin solutions (2.4 wt% - 4 wt%) were kept at 4 °C and used within a month of synthesis.

4.2.4 Suspension Stability Studies

To study the stability of the MXene and SFMX dispersions over time, suspensions of each at 0.1 wt%, 0.05 wt%, and 0.01 wt% concentrations were made and kept at 4 °C for 22 days and used for AFM, FTIR, and UV-Vis measurements, respectively. The remaining initial suspension (typically ~0.2 wt% SFMX) was split so some solution could be kept at both 4 °C and room temperature for XPS measurements. Over the course of three weeks, the suspensions were deposited on wafers or an ATR crystal every other day so that AFM, FTIR, and UV-Vis measurements could be taken at different time points. XPS measurements were only done for films deposited from fresh and 22 - day old suspensions. Control samples were made by spin or drop casting silk from solution kept at 4 °C for six days and 105 days. The films made from six-day old silk solution were placed in vials of water and kept at 4 °C and 50 °C for three days and then allowed to dry at room temperature.

4.2.5 Transport Properties

Filtration experiments were carried out on thin membranes using a separate 2.27 cm^2 area vacuum filtration setup to avoid errors associated with membrane edges. Aqueous solutions (2 mL) of 0.01 mg mL^{-1} rhodamine 6G (R6G), methylene blue (MB), Coomassie brilliant blue (BB), and pyranine (P) were filtered through the films using a 17 mm diameter filtration setup. UV-Vis measurements were taken of all solute and filtered solutions to determine dye concentration before and after filtering.

4.2.6 Characterizations

Atomic force microscopy images of the modified flakes were obtained using tips of radium 2 nm for high resolution scans of fibrils.[10] To test the affinity of MXene and silk fibroin, we spin cast MXene flakes onto a thermally oxidized silicon wafer and then ~50 μL of silk fibroin solution was drop cast onto the sample directly, allowed to sit for one minute, and then rinsed with water and air dried. To ensure the same flake could be measured before and after the silk drop, the silicon wafer was patterned with a gold marked TEM grid before deposition, flakes were imaged, then treated, and imaged again. Histograms shown of flakes have a peak associated with the height given by AFM scans of the silicon substrate (lowest height peak) as well as the heights given of the flakes (highest height peak). SFMX flakes with a silk corona show either a distinct peak or slight shoulder between the lowest and highest height peaks. *Attenuated total reflectance Fourier transform infrared spectroscopy* was used on drop cast samples of 0.05 wt% SFMX dispersions to investigate the secondary structures seen in AFM imaging. *Scanning electron microscopy* was used to image free-standing films for thickness determination.

DLS measurements using a Malvern Instruments Nano series Zetasizer were taken of the dye solutions to investigate the surface charges. The zeta potentials were averaged over five scans with 10 – 100 runs each on the dye solutions using a dip cell.

4. 3 Results and Discussion

4.3.1 Morphology of silk-MXene flakes

AFM images show pristine MXene flakes with lateral dimensions around 1 micrometer (0.5 – 1.5 μm) and nanometer scale thickness (Figure 4.2a). First, we studied how silk is absorbed from solution onto MXene flakes and silicon oxide surfaces by directly comparing the same flake before and after silk absorption by conducting repeated measurements of exactly the same flake which can be identified after return from exposure to dispersion by grid-controlled optical visualization (Figure 4.2). MXene flakes were spun cast onto a silicon wafer and then silk fibroin solution was drop-cast onto the sample, allowed to sit for one minute, gently rinsed with water, and carefully air dried to avoid shear induced changes.

Imaging of the same flake reveals an increase in rms micro-roughness (as measured within 150 nm x 150 nm selected surface area) from R_q: 0.272 nm to 0.505 nm while the surrounding wafer has an increase from R_q: 0.167 nm to 0.534 nm (Figure 4.2b). Such an increase is caused by the presence of globular silk protein on the flake and the surrounding wafer surfaces with heights of 0.96 ± 0.18 nm and 1.61 ± 0.65 nm, respectively.

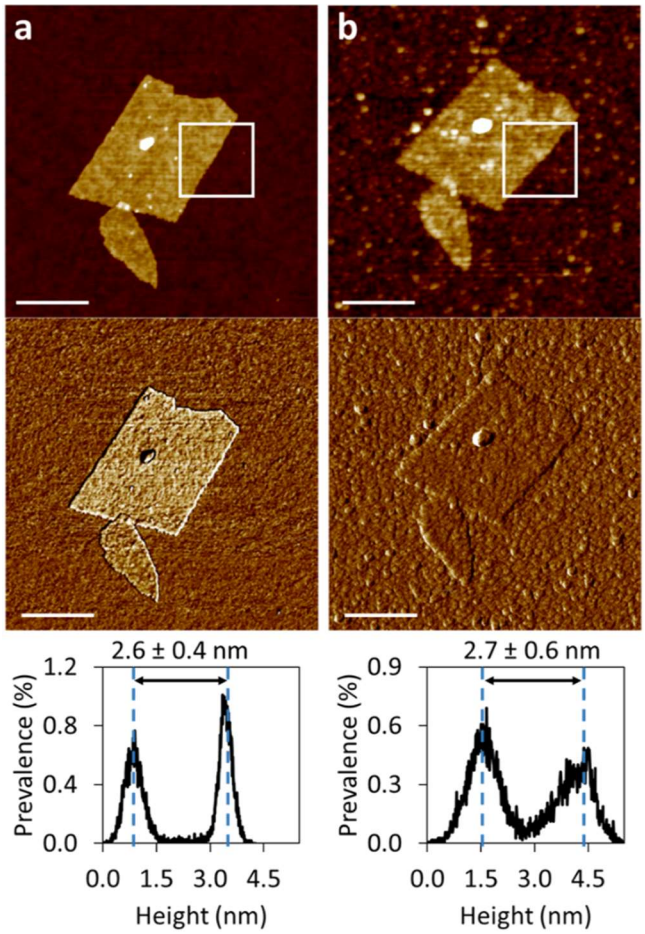

Figure 4.2 AFM topography images (top), corresponding phase images (middle), and height histograms (bottom) from the selected white boxes of a pristine $Ti_3C_2T_x$ MXene flake (a) and after silk deposition and rinsing (b). Z-scale is 7 nm for topography and 6° scale for phase images (all scale bars are 200 nm).

The average flake heights are calculated from the difference in corresponding peaks (substrate surface and flake surface) on the height histograms taken from 0.04 μm^2 boxes placed half on and off the flake (Figure 4.2a). The apparent flake thickness of 2.6 ± 0.4 nm suggest that in this case, we observe MXene bilayer considering the average flake thickness of 1.6 ± 0.1 nm (Figure A.1a) consistent with literature values for individual flakes with pre-absorbed layers.[11–14] The same thickness after silk deposition suggests a similar affinity

of the silk to both the flake and silicon wafer surfaces, each containing hydrogen-bonding surface groups.[15]

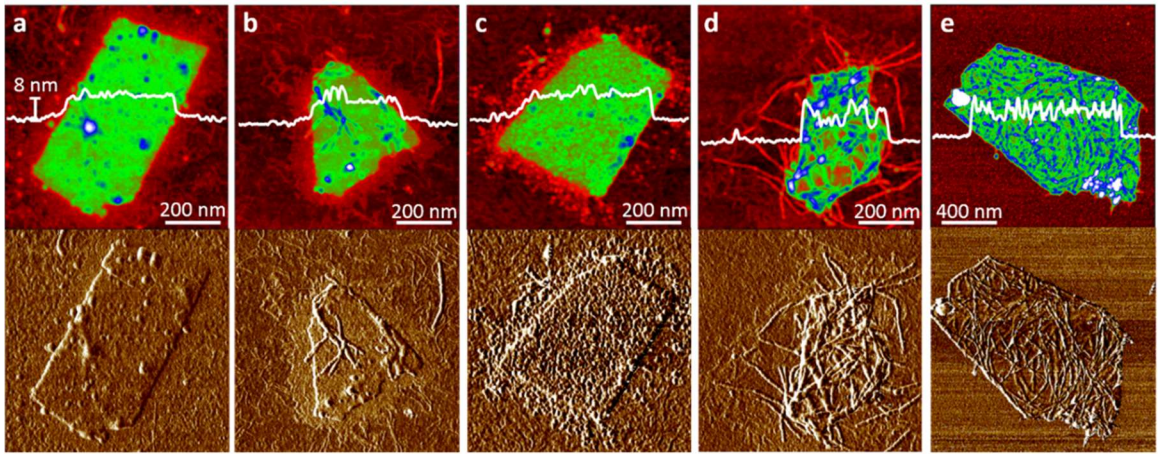

Figure 4.3 AFM topography images (top) and corresponding phase images (bottom) of co-assembled SFMX on days one (a), three (b), five (c), seven (d), and 19 (e) with 20 nm Z-scale for topography, and 6° scale for phase images. Topography images are provided in false color to better show silk corona morphology.

Next, we conducted AFM measurements on representative silk-co-assembled flakes from silk-MXene water suspensions held for different times (up to 19 days) at 4 °C (Figure 4.3). Modified flakes show increased thickness and evolving surface morphology indicating complex processes of absorption and assembly of silk materials onto MXene surfaces in mixed suspensions. AFM reveals that the silk-modified MXenes show smooth surface with occasional globular protein structures (Figure 4.3a) followed by gradual reorganization of the secondary structure into long nanofibrils with a beads-on-a-string morphology over the course of three weeks (Figure 4.3, for all AFM images for varying days, Figure A.1-5). The flake and silk corona heights were determined by calculating the

differences between peaks in height histograms taken from 0.25 μm^2 boxes (see representative example in Figure A.6).

The dimensions of individual features such as globules, nanofibers, and fibers were measured via cross sections as shown in Figure A.6. Overall, the global model of the initial silk-modified MXene flake with all dimensions derived in the current study show an individual MXene bilayer encapsulated in a silk shell with the effective thickness of around 2.5 nm, thus providing estimation of silk volume content in surrounding shell of about 68% (Figure 4.1c). More complex co-assembly with distinct time related morphology evolution is discussed below.

Freshly made suspension yielded 7.63 ± 0.32 nm thick MXene flakes with a bed of globular silk of height 0.74 ± 0.23 nm and a 1.28 ± 0.35 nm thick silk corona extending 81.6 ± 16.9 nm off the sides of the flake (Figure 4.3a). These flakes also showed to have some isolated globules measuring 1.25 ± 0.1 nm and 4.12 ± 0.3 nm in eight similar to the spin cast silk control films shown in Figure A.7. The height on the flake may be slightly skewed due to the uneven surface of silk globules underneath. The most prominent features, extended fringes of the silk corona resemble that of irregularly shaped nanofibrils with some measuring 1.33 ± 0.1 nm and some 0.86 ± 0.08 nm in height, which are similar to those seen on conventional drop cast silk films (Figure A.7) as well as those reported in literature.[14–16] Those structures measuring near 0.8 nm are similar to the expected dimensions of a single silk backbone[17–19] and closely resemble nanofibers formed in response to shear applied by spin casting low concentration silk solutions on mica[20] as well as those observed of silicon dioxide and graphene oxide substrates, rich in hydrogen-bond surface groups.[7,21]

It is clear from the analysis of these images that, as early as day two and three, isolated silk nanofibrils with the beads-on-a-string morphology start to form on a uniform bed of silk on top of MXene flakes. These nanofibrils have apparent heights 2.46 ± 0.54 nm on top of the flakes while those that extend off of the flake measure 3.99 ± 0.6 nm in height, similar to those reported in literature for silk nanofibers formed on oxidized surfaces of different nature.[20,22,23] These flakes also display a well-developed corona from silk nanofibers in sharp contrast with initial minor corona composed of small bundles seen after day one (Figure 4.3).

Interestingly, day five aging shows a mix of flakes with a coating of large (1.65 ± 0.93 nm) globules, some with amorphous silk coatings and nanofibrils, and some with all three coexisting morphologies. Some of these flakes do not have a uniform silk corona and displayed a morphology consisting of only large silk globules like that seen on spin cast silk samples after being stored in water for three days. On day seven, the flakes show coverage with mostly fibrils on the flake with some extending off the flake edges. The silk corona, at this time point, no longer uniformly surrounds the flake and instead more closely resembles loose packs of extended nanofibrils. Finally, by day 19, all flakes have lost their silk nanofibrillar corona and show a relatively uniform coverage of the flake surface with densely packed nanofibrils with little extending across the flake edges (Figure 4.3). This morphology is only shared by the control silk films made by drop casting of silk that was kept in water.

This behavior is revealed during "real-time" monitoring of silk-MXene co-assembly in contrast to those observed for other 2D materials.[1,24,25] A study on modifying graphene oxide with silk at high temperature and pH showed rigid silk fibroin formation

on a short timeline with no evidence of a silk corona.[7] Previous studies have shown that the β-sheet organization and nanofibrillar morphology of silk is the energetically favored structure.[26] However, van der Waals interactions between multi-block amphiphilic silk fibroins and hydrophobic materials like graphene disrupt intramolecular hydrogen bonding interactions in favor of intermolecular bonding with the hydrophobic species.[27] Molecular dynamics simulations show that electrostatic interactions bring the silk backbones close to hydrophilic and oxidized surfaces, while hydrogen bonding is responsible for binding.[15] Considering that nanofibrils form as early as day three, it is most likely that the MXene surface is serving as a nucleation site for organized nanobundles to form. Finally, we suggest that similar composition of oxygen terminated surface groups causes silk to bind to MXene flakes similar to those observed for graphene oxide flakes. However, stronger affinity and stronger surface and predominant hydrophobicity of the MXene edge initiate the formation of the longer silk nanofibrils extending across the edges that is not usually observed for graphene oxides. To further consider the role of surface chemistries and secondary organization, we monitored structural changes with various spectroscopies.

4.3.2. Monitoring of secondary structure and surface chemistry of silk-MXene flakes

Attenuated total reflectance Fourier-transform infrared spectroscopy (ATR-FTIR) measurements show a broadening around the amine I and II peaks centered around 1530 cm^{-1} and 1690 cm^{-1} that may be due to increased hydrogen bonding (Figure A.8).[20,22] Further measurements were taken in higher resolution in limited window to monitor how slight changes in the amide I peaks correspond to increases in β-sheets with co-assembly time (Figure 4.4).[15,26,28] The analysis of the fractions of each type of secondary structure typically seen in silk fibroin (random coils, α-helices, turns, and β-sheets) shows the

amount of β-sheets in the system increasing while the other possible secondary structures decrease. The increase of the β-sheet content corresponds to the expansion of the nanofibrillar morphology at the expense of the disordered silk surrounding observed in AFM studies and support the conclusions made upon the morphological observations (Figure 4.3). However, the fraction of random coils in silk matrix increases only until day seven and then decreases after. These changes correspond to the increased presence of bead-like features that have increased content of random coils before restructuring into extended nanofibrils.[22]

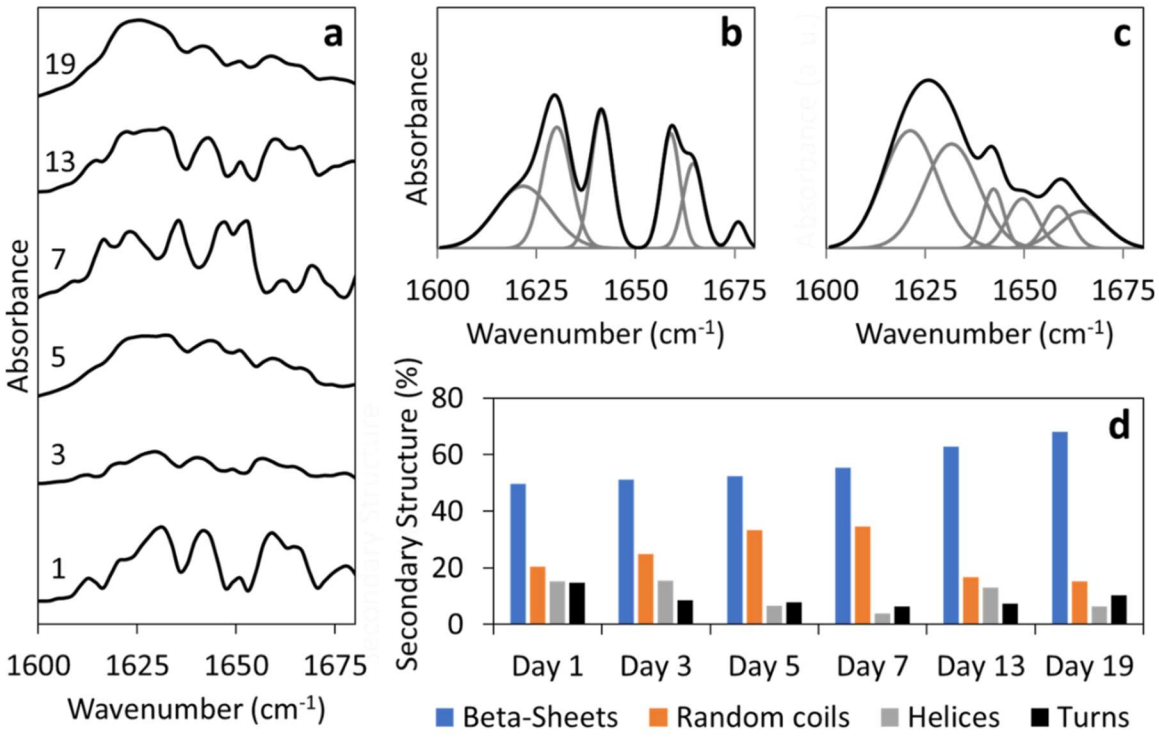

Figure 4.4. ATR-FTIR spectra of SFMX over time (a), examples of deconvolution for day one (b) and day 19 (c), and the secondary structure of the silk evolution in SFMX after different co-assembly time (d).

Furthermore, to investigate the effect of silk encapsulation on the surface oxidation of MXene flakes, the chemical composition and light absorption features of the silk-modified MXenes on the first and following days after modification have been analyzed by using X-ray Photoelectron Spectroscopy (XPS) (Figures 4.5 and A.9) and UV-vis spectroscopies (Figures 4.6 and A.10).

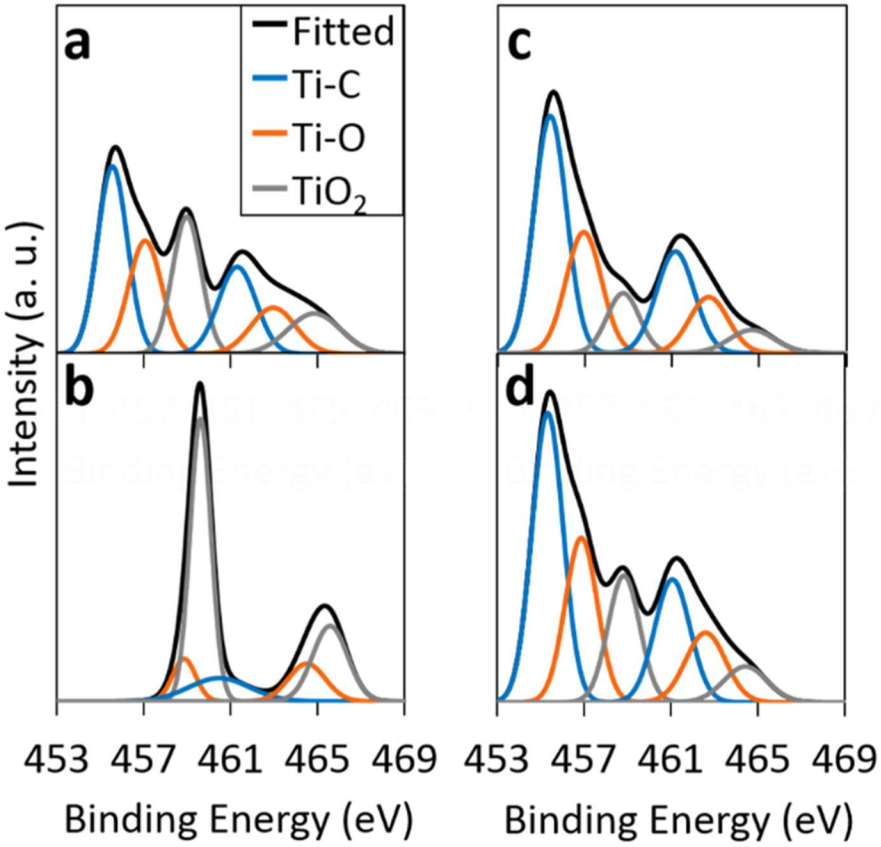

Figure 4.5. Ti 2p XPS spectra of MXene (a, b) and Silk modified MXene (c, d) on day one (a, c) and after being kept in water for 22 days at room temperature (b, d).

As expected, survey XPS spectra confirm the presence of titanium (Ti), carbon (C), fluorine (F), oxygen (O), and nitrogen (N) thus high-resolution spectra (Ti2p, C1s, O1s, and N1s) of each were obtained and deconvoluted to determine specific origins of the peaks

(Figures 4.5, A.9). Some survey spectra showed very minor traces of silicon, chlorine, and sodium that can be attributed to impurities from water, the substrate, and glass containers compromised by fluorine groups.

The Ti 2p spectra contain three doublets representing Ti-C at 455.8 and 461.5 eV, Ti-O at 457.5 and 463.3 eV, and TiO_2 at 459.4 and 464.7 eV. The data shows MXene having 29.3 % TiO_2, 27.9 Ti-O, and 42.8% Ti-C while the silk modified flakes are shown to have 14.3 % TiO_2, 30.8 Ti-O, and 54.9% Ti-C bonds on just the first day after modification. After 22 days, the MXene surface composition was 69.3% TiO_2, 19.1% Ti-O, and 11.6% Ti-C while the SFMX composition was 20.7% TiO_2, 29.9% Ti-O, and 49.4% Ti-C.

As previously reported, pristine $Ti_3C_2T_x$ MXene surfaces contain =O, -OH, and -F surface terminations as a result of synthesis conditions.[1,23,23,29] After exposure to water at room temperature, the Ti-C bonds reduce in number while Ti(IV) oxide bonds increase.[29] Within 10 days, larger amounts of Ti(II) and Ti(III) suboxides and hydroxides can be found via XPS and after 25 days, the MXene is thought to contain only Ti (III) suboxides and TiO_2 resulting in agglomeration and falling out of suspension. Reducing the temperature of the suspension and filling the containers with argon decreased the overall oxidation rate.[29] Argon gas helps to reduce oxidation more compared to decreased storage temperature suggesting dissolved oxygen in water accelerates oxidation at the edges of MXene flakes causing smaller flakes to oxidize faster.[29] The XPS measurements in this study show a similar result for the pristine MXene suspension. In contrast, the SFMX dispersion shows minimal reduction in Ti-C and little increase in TiO_2 content. Therefore,

we can conclude that encapsulating MXene flakes in silk shells effectively dampens oxidation of MXene in an aqueous environment.

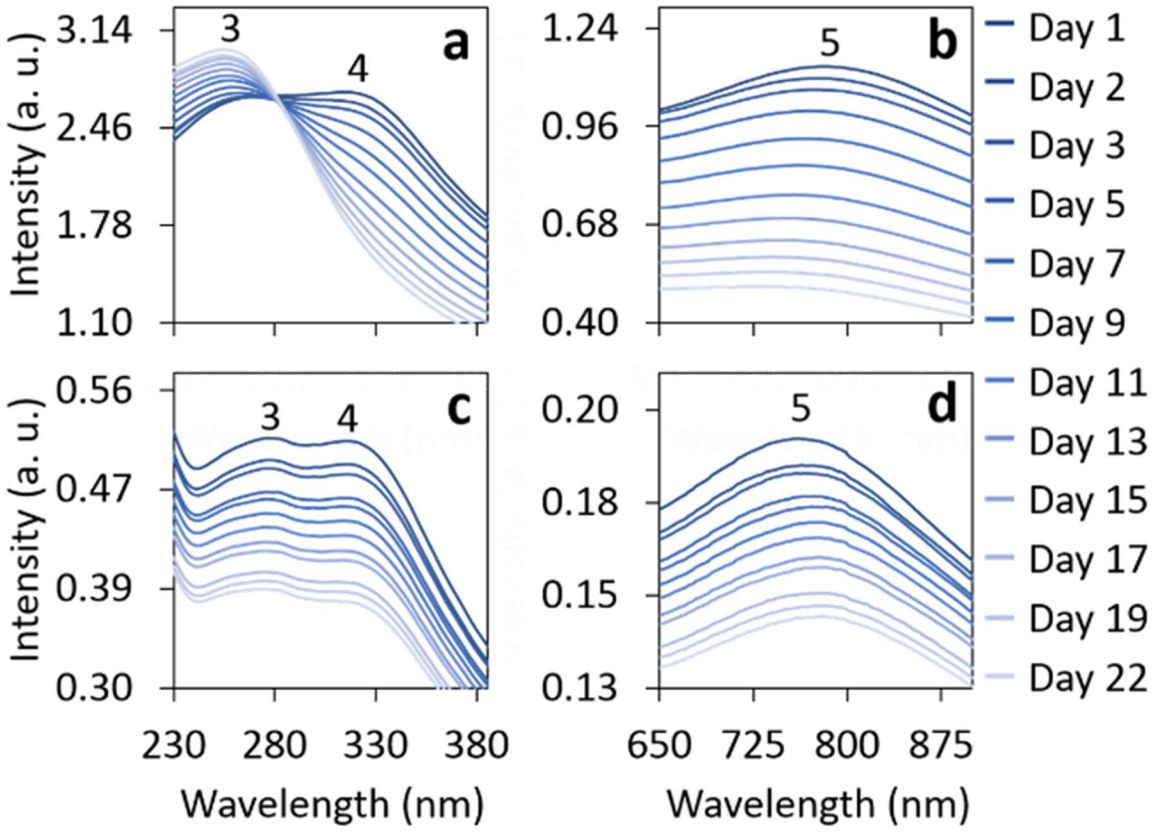

Figure 4.6. UV-Vis spectra of pristine MXene (a, b) and silk modified MXene (c, d) at 0.01 wt% in water showing 2 peaks between 235 and 385 nm (a, c) and one between 650 to 900 nm (b, d).

To further investigate the evolution of silk-encapsulated MXenes, UV-Vis spectra were obtained from 0.01 wt% silk, MXene, and SFMX suspensions over the course of three weeks (Figure A.10). UV-Vis spectra of SFMX suspensions show a $Ti_3C_2T_x$ characteristic peak between 750 nm and 800 nm (5) as well as a peak at 188 nm (1), a shoulder around 227 nm (2), and peaks at 270 nm (3) and 307 nm (4) (Figure A.10). Peaks 1 and 2 can be attributed to the silk materials since both silk and SFMX display them but pristine MXene

does not. All suspensions show a peak 3, and this peak is not changed significantly from that of pristine MXene suggesting MXene is the major contributor to this peak.

Peaks 3, 4, and 5 are frequently examined in literature to determine the size of flakes and degree of oxidation.[29,30] Close ups of peaks 3, 4, and 5 show a reduction in intensity for SFMX while only peaks 4 and 5 show a reduction of intensity for pristine MXene (Figure 4.6). The decrease in peak 3 to 4 intensity ratio has been reported as due to a reduction of flake size or oxidation induced rounding of flakes while the absorbance reduction in peak 5 has been attributed to increased oxidation.[31]

The summaries of changes in peak position and intensity are provided in Figure A.11. Peak 5 in pristine MXene suspension shows a large decrease in intensity (by 60%) from the first to the 22nd day while SFMX shows a much lower decrease (by only 5%). During this time, the pristine MXene oxidizes and falls out of suspension while the silk-encapsulated flakes remain more stable.

Peak 5 shows slight blue shifting over time in the MXene and slight red shifting in the SFMX suspension (Figure 4.7). Typically, a reduction in intensity signifies oxidation of MXene flakes due to oxidation-induced edge rounding. However, AFM shows no significant signs of oxidation of SFMX with a silk coating (Figure A.1-5).

Considering the changes of silk secondary structures on the MXene flakes takes place in suspension over time and a lack of clear topological evidence of MXene flake oxidation if encapsulated, it is possible to suggest that the silk is blocking surface groups on MXene flakes available for oxygenation. Silk has proven to form ordered structures like those observed in this study due to diverse electrostatic, hydrophobic, and hydrogen

bonding interactions.[15] The hydrophobic β-sheets become more stable when silk chains are in contact with a heterogeneous hydrophilic surface due to weakened van der Waals interactions. The positive charges provided by the amines may grant support through

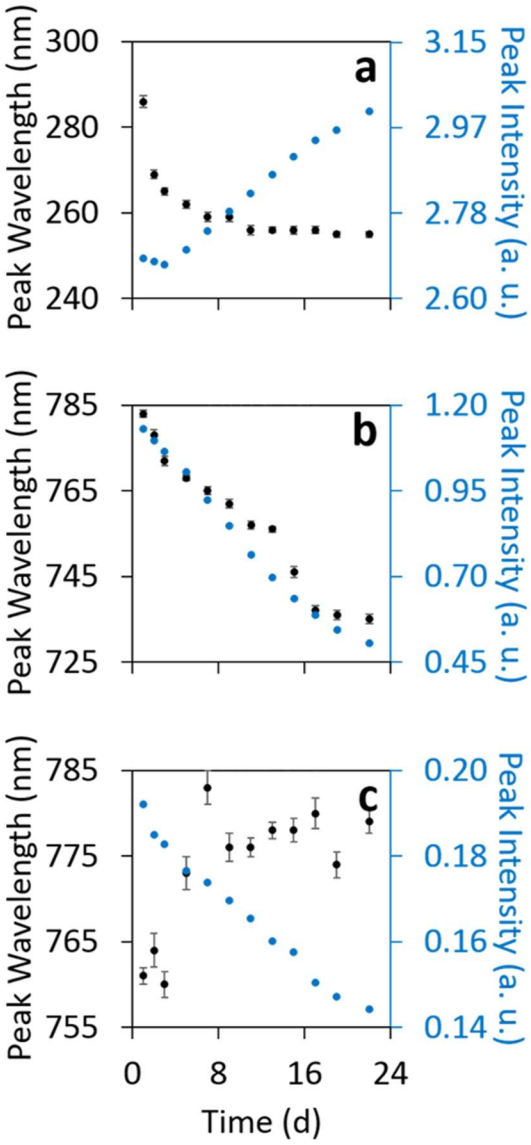

Figure 4.7. Plots of UV-Vis peak position and absorbance intensity for peaks 3 (a) and 5 (b, c) as designated in Figure A.8 for pristine MXene (a, b) and SFMX (c) suspensions.

electrostatic interactions with negatively charged hydroxyls. Hydrogen bonds form between hydrogen and a donor atom with a lone pair of electrons (such as oxygen or nitrogen). In the case of silk, the -NH group hydrogen is partially positive while the C=O is partially negative and provides the lone pair of electrons.[15,26,32] These groups on the amino acids form hydrogen bonds and result in β-sheets that can be linked via van der Waals interactions to form hydrophobic sections and promote nanofibril formation.[12,33,34]

Silk has also shown to reduce oxygenated groups on graphene oxide due to its amino acid reaction, resulting in the disappearance of the C=O bonds and a reduction of C-O, and C-OH content, thus dampening the oxidation rate.[35] An additional factor is the increasing content of hydrophobic bundles, which densely cover the surface and edges of the flakes thus creating a hydrophobic cushion protecting the underlying MXene surface from oxidation, especially at the most vulnerable place, edges. To this end, we suggest that having a unique composite morphology of silk encapsulating the MXene with a unique corona morphology extending over the edges is critical in the unusual oxidation damping observed in this study. It is worth noting that usual treatments with methanol[36] and drying resulted in faster silk nanofibrillar formation on flakes but not extending over the edges preventing the unique silk corona morphology from forming (Figure A.12).[15,37,38]

4.3.3 Morphology and Transport Properties of Silk-Encapsulated MXene Membranes

Finally, we consider if having tightly encapsulated MXene flakes with tethered nanofibrillar silk coronas can be exploited to construct robust bionanocomposite functional materials. Here, we focus on testing if robust organized silk-MXene films can be assembled by common assembling approaches; if the original functionalities important for

constructing functional devices, such as electrical conductivity, can be still preserved; and, finally, how some commonly known applications, such as selective ion transport via MXene membranes, will be altered in silk-modified MXenes.

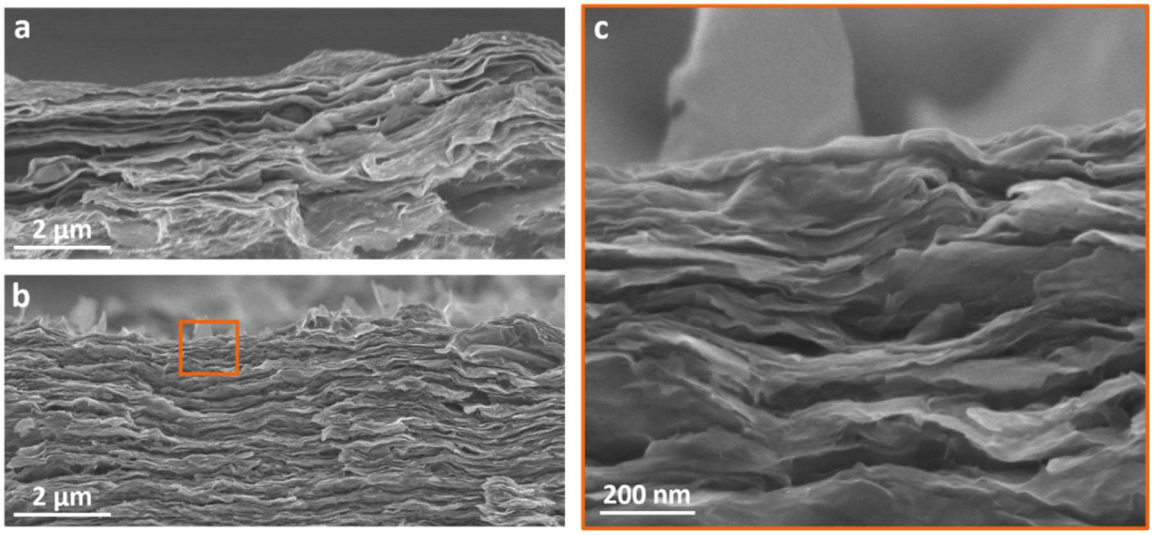

Figure 4.8. SEM micrographs showing cross sections of fractured MXene (a) and SFMX (b, c) membranes assembled via vacuum assisted filtration; (c) shows a magnified image of the area framed in (b).

First, a film of SFMX was prepared using vacuum-assisted filtration in order to form organized laminated films, a common approach for 2D materials such as GO and MXenes (Figure 4.8).[2,39–41] The MXene membrane obtained in this manner displays an ordered lamellar structure (Figure 4.8a) when imaged with scanning electron microscopy (SEM). It is important that the corresponding SFMX membranes also possess highly ordered lamellar organization with an even more dense and uniform laminated packing (Figure 4.8b). A continuous, 2D laminated morphology is clearly visible under higher magnification with delamination of individual lamellae during membrane fracturing under uniaxial tension (Figure 4.8c).

Table 4.1 Table showing resistance measurements obtained via four-point-probe measurements on MXene and SFMX films fabricated using vacuum assisted filtration as well as literature reported values.

Material	Thickness (μm)	Conductivity (S/m)	Ref.
MXene	5.20	$3.64 \pm 0.11 \times 10^5$	This work
MXene	2.09	$1.40 \pm 0.02 \times 10^6$	This work
SFMX	3.14	$5.94 \pm 0.08 \times 10^3$	This work
SFMX	11.9	$5.36 \pm 0.87 \times 10^{-2}$	This work
MXene	3.3	2.4×10^5	[42]
MXene	3.0	4.56×10^5	[40]
MXene		3.2×10^5	[43]
MXene	1.0	1.4×10^6	[44]

Secondly, we found that microscopic silk-MXene membranes remained conductive even if the content of silk matrix was estimated to be around 68% but silk shell having only 2.5 nm thickness (corresponding to 3-4 backbones) (Table 4.1). Electrical resistance measurements were made using the four-point-probe technique[45] and the conductivity was calculated using thicknesses obtained via averaging measured thicknesses from SEM images (examples shown in Figure A.14). These measurements show a high conductivity for pristine MXene films of $10^5 – 10^6$ Sm^{-1} comparable with those reported in literature for MXene films (10^5 Sm^{-1} and above) (Table 4.1).[42,43,45] Most importantly, three and 12 micrometer thick silk-MXene films still maintain modest conductivity values of 5940 Sm^{-1} and 0.054 Sm^{-1}, respectively (Table 4.1). Such a reduction of conductivity is caused by tight encapsulation of MXene flakes with extended silk coronas over flake edges that creates 2-4 nm dielectric gaps between flakes and compromise the low percolation limit for 2D laminated materials. However, these values are comparable to those reported for partially reduced 2D graphene oxide materials which are widely used for various electronic-related applications.[46,47] Overall, in a simple preliminary demonstration, we

observed that the SFMX nanocomposites can serve as a flexible electrode in electrical circuitry able to light up a LED source (Figure 4.9).

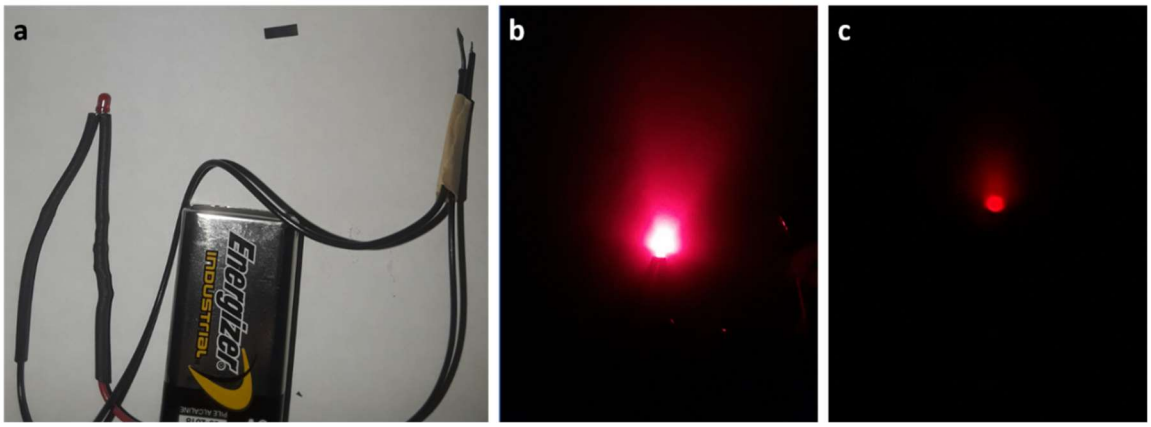

Figure 4.9 Pictures showing an LED set up with a 9V battery (a) lighting up a 5.2 µm thick MXene film (b) and a 10.6 µm thick SFMX film (c).

Finally, we explored if membranes from silk-modified MXene can show selective filtration performance observed for pure MXene components.[48] The good performance of the MXene film has been shown before with a film made using 0.24 mg of pristine MXene in suspension filtering out 100% of BB dye.[49] To test the separation performance of the SFMX films, we used 0.01 mg mL^{-1} solutions of common dyes with diverse dimensions and charges: Coomassie brilliant blue (BB), pyranine (P), para methyl red (PMR), rhodamine 6G (R6G), and methylene blue (MB) with measured zeta potentials of -30.4 ± 0.8, -26.4 ± 1.4, -9.0 ± 1, -0.8 ± 0.8, and 7.0 ± 1 mV, respectively (Figure 4.9).

Each dye and filtrate solution was measured using UV-Vis in order to determine dye rejection based on concentration (Figure A.15). SFMX films fabricated here have shown excellent filtering ability for BB with MXene rejecting 97.9% and SFMX rejecting

100% of the filtrate (Table A.1). The SFMX film was able to filter out 60.3%, 94.6%, 98.8%, and 98.9% of the solutions of P, PMR, R6G, and MB, respectively (Figure 4.10). Control MXene films without the silk encapsulation fabricated under identical conditions

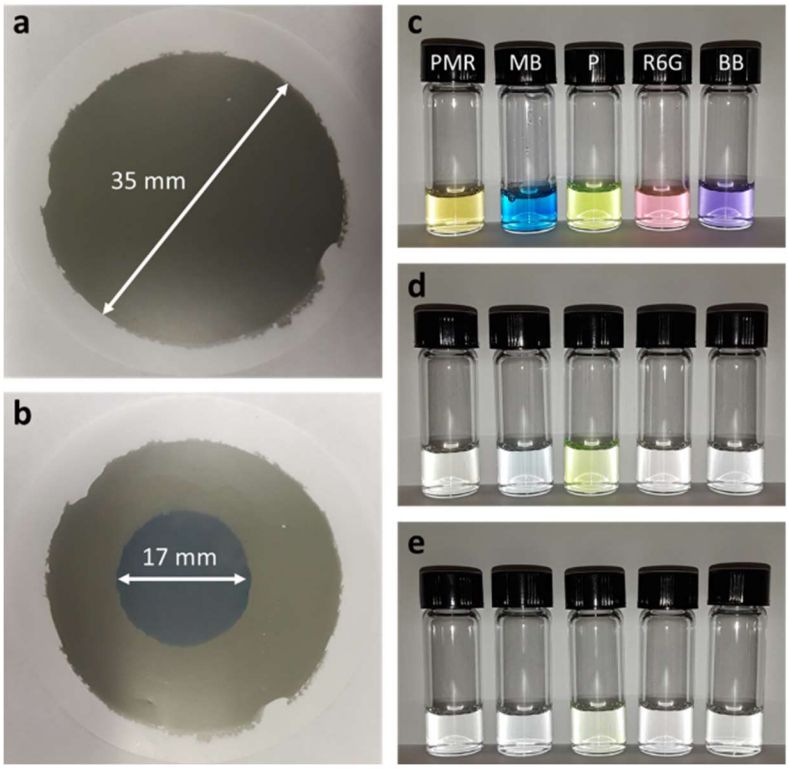

Figure 4.10 Images of a representative SFMX film on track-etched polycarbonate membrane before (a) after (b) filtering out MB dye. Optical images of glass vials containing filtrate solution before (c) and after being filtered with MXene films (d) and SFMX films(e).

and with identical MXene flakes could only filter out 11.5%, 43.2%, 98%, and 88.9% of P, PMR, R6G, and MB, respectively. The dye solutions lost most of their color after being filtered through both MXene and SFMX films (Figure 4.10) with only P retaining enough color to distinguish it from the others. For each of the solutions, the SFMX membranes had

slightly slower permeances than MXene with 1171.6 $Lm^{-2}bar^{-1}h^{-1}$ and 324.7 $Lm^{-2}bar^{-1}h^{-1}$ permeances for clean water, respectively.

From these preliminary results, we can conclude that one-component MXene membranes typically show lower rejection rate and selective filtering for negatively charged dyes due to repulsive Columbic interactions while silk-containing MXene membranes with both cationic and anionic amino acids show much higher rejection rates for negatively charged dyes as well as positively charged dyes selected here making them more "universal" membranes for filtering (Figure 4.10). The reduction in permeance observed across all dyes utilized in this study suggests the presence of a silk shell with thickness of 2-4 nm between MXene flakes and silk corona in gaps between the flake edges hinder overall fluidic flow due to slow relaxation of silk segments and increased resistivity within small pores available (from 7 to 35 nm for different silks).[50–52] The mechanical strength of the SFMX flakes singularly and within larger membranes should be studied to optimize mechanical properties for specific applications.

4.4 Conclusion

In conclusion, we have shown the bioencapsulation of 2D $Ti_3C_2T_x$ MXene flakes with unique silk uniform coatings and hairy morphologies. This study demonstrates the ability of MXene flakes to serve as a nanostructured template for the self-assembly of silk nanofibrils while in mixed aqueous suspension. This selective uniform deposition of silk is a novel approach that effectively protects MXene flakes from surface oxidation allowing for longer storage time in aqueous suspensions. Through time-controlled studies of individual flakes and their suspensions, we have shown the evolution of silk fibril

formation on the $Ti_3C_2T_x$ surface. This change in silk morphology can be used to control the mechanical properties of bio-nanocomposite films and mediate interfaces for different biological applications, which is an important and quickly growing area of applications for biocompatible MXenes, like $Ti_3C_2T_x$. This strategy also enables the fine tuning of flake-to-flake interactions for modulating the mechanical and electrical properties of this class of MXene-based bio-2D hybrid materials. Mechanical properties of this system are studied according to procedures established in our group[53,54] and discussed in the following chapter.

4.5 References

(1) Anasori, B.; Lukatskaya, M. R.; Gogotsi, Y. 2D Metal Carbides and Nitrides (MXenes) for Energy Storage. *Nature Reviews Materials* **2017**, *2* (2). https://doi.org/10.1038/natrevmats.2016.98.

(2) Xiong, R.; Grant, A. M.; Ma, R.; Zhang, S.; Tsukruk, V. V. Naturally-Derived Biopolymer Nanocomposites: Interfacial Design, Properties and Emerging Applications. *Materials Science and Engineering R: Reports* **2018**, *125*, 1–41. https://doi.org/10.1016/j.mser.2018.01.002.

(3) Vural, M.; Pena-Francesch, A.; Bars-Pomes, J.; Jung, H.; Gudapati, H.; Hatter, C. B.; Allen, B. D.; Anasori, B.; Ozbolat, I. T.; Gogotsi, Y.; Demirel, M. C. Inkjet Printing of Self-Assembled 2D Titanium Carbide and Protein Electrodes for Stimuli-Responsive Electromagnetic Shielding. *Advanced Functional Materials* **2018**, *28* (32), 1801972. https://doi.org/10.1002/adfm.201801972.

(4) Vural, M.; Zhu, H.; Pena-Francesch, A.; Jung, H.; Allen, B. D.; Demirel, M. C. Self-Assembly of Topologically Networked Protein- -Ti3C2Tx MXene Composites. *ACS Nano* **2020**. https://doi.org/10.1021/acsnano.0c01431.

(5) Savchak, M.; Borodinov, N.; Burtovyy, R.; Anayee, M.; Hu, K.; Ma, R.; Grant, A.; Li, H.; Cutshall, D. B.; Wen, Y.; Koley, G.; Harrell, W. R.; Chumanov, G.; Tsukruk, V.; Luzinov, I. Highly Conductive and Transparent Reduced Graphene Oxide

Nanoscale Films via Thermal Conversion of Polymer-Encapsulated Graphene Oxide Sheets. *ACS Applied Materials and Interfaces* **2018**, *10* (4), 3975–3985. https://doi.org/10.1021/acsami.7b16500.

(6) Xiong, R.; Kim, H. S.; Zhang, L.; Korolovych, V. F.; Zhang, S.; Yingling, Y. G.; Tsukruk, V. V. Wrapping Nanocellulose Nets around Graphene Oxide Sheets. *Angewandte Chemie - International Edition* **2018**, *57* (28), 8508–8513. https://doi.org/10.1002/anie.201803076.

(7) Ling, S.; Li, C.; Adamcik, J.; Wang, S.; Shao, Z.; Chen, X.; Mezzenga, R. Directed Growth of Silk Nanofibrils on Graphene and Their Hybrid Nanocomposites. *ACS Macro Letters* **2014**, *3* (2), 146–152. https://doi.org/10.1021/mz400639y.

(8) Jin, H.-J.; Kaplan, D. L. Mechanism of Silk Processing in Insects and Spiders. *Nature* **2003**, *424* (6952), 1057–1061. https://doi.org/10.1038/nature01809.

(9) Murphy, A. R.; Kaplan, D. L. Biomedical Applications of Chemically-Modified Silk Fibroin. *J. Mater. Chem.* **2009**, *19* (36), 6443–6450. https://doi.org/10.1039/B905802H.

(10) McConney, M. E.; Singamaneni, S.; Tsukruk, V. V. Probing Soft Matter with the Atomic Force Microscopies: Imaging and Force Spectroscopy. *Polymer Reviews* **2010**, *50* (3), 235–286. https://doi.org/10.1080/15583724.2010.493255.

(11) Lipatov, A.; Lu, H.; Alhabeb, M.; Anasori, B.; Gruverman, A.; Gogotsi, Y.; Sinitskii, A. Elastic Properties of 2D Ti 3 C 2 T x MXene Monolayers and Bilayers. *Science Advances* **2018**, *4* (6). https://doi.org/10.1126/sciadv.aat0491.

(12) Lipatov, A.; Alhabeb, M.; Lukatskaya, M. R.; Boson, A.; Gogotsi, Y.; Sinitskii, A. Effect of Synthesis on Quality, Electronic Properties and Environmental Stability of Individual Monolayer Ti3C2 MXene Flakes. *Advanced Electronic Materials* **2016**, *2* (12). https://doi.org/10.1002/aelm.201600255.

(13) Ding, L.; Wei, Y.; Li, L.; Zhang, T.; Wang, H.; Xue, J.; Ding, L.-X.; Wang, S.; Caro, J.; Gogotsi, Y. MXene Molecular Sieving Membranes for Highly Efficient Gas Separation. *Nature Communications* **2018**, *9* (1). https://doi.org/10.1038/s41467-017-02529-6.

(14) Zhong, J.; Liu, X.; Wei, D.; Yan, J.; Wang, P.; Sun, G.; He, D. Effect of Incubation Temperature on the Self-Assembly of Regenerated Silk Fibroin: A Study Using AFM. *International Journal of Biological Macromolecules* **2015**, *76*, 195–202. https://doi.org/10.1016/j.ijbiomac.2015.02.045.

(15) Grant, A. M.; Kim, H. S.; Dupnock, T. L.; Hu, K.; Yingling, Y. G.; Tsukruk, V. V. Silk Fibroin–Substrate Interactions at Heterogeneous Nanocomposite Interfaces. *Advanced Functional Materials* **2016**, *26* (35), 6380–6392. https://doi.org/10.1002/adfm.201601268.

(16) Koebley, S. R.; Thorpe, D.; Pang, P.; Chrisochoides, P.; Greving, I.; Vollrath, F.; Schniepp, H. C. Silk Reconstitution Disrupts Fibroin Self-Assembly. *Biomacromolecules* **2015**, *16* (9), 2796–2804. https://doi.org/10.1021/acs.biomac.5b00732.

(17) Zhong, J.; Ma, M.; Li, W.; Zhou, J.; Yan, Z.; He, D. Self-Assembly of Regenerated Silk Fibroin from Random Coil Nanostructures to Antiparallel β-Sheet Nanostructures. *Biopolymers* **2014**, *101* (12), 1181–1192. https://doi.org/10.1002/bip.22532.

(18) Gong, Z.; Huang, L.; Yang, Y.; Chen, X.; Shao, Z. Two Distinct β-Sheet Fibrils from Silk Protein. *Chemical Communications* **2009**, No. 48, 7506–7508. https://doi.org/10.1039/b914218e.

(19) Greving, I.; Cai, M.; Vollrath, F.; Schniepp, H. C. Shear-Induced Self-Assembly of Native Silk Proteins into Fibrils Studied by Atomic Force Microscopy. *Biomacromolecules* **2012**, *13* (3), 676–682. https://doi.org/10.1021/bm201509b.

(20) Belton, D. J.; Plowright, R.; Kaplan, D. L.; Perry, C. C. A Robust Spectroscopic Method for the Determination of Protein Conformational Composition – Application to the Annealing of Silk. *Acta Biomaterialia* **2018**, *73*, 355–364. https://doi.org/10.1016/j.actbio.2018.03.058.

(21) Shulha, H.; Po Foo, C. W.; Kaplan, D. L.; Tsukruk, V. V. Unfolding the Multi-Length Scale Domain Structure of Silk Fibroin Protein. *Polymer* **2006**, *47* (16), 5821–5830. https://doi.org/10.1016/j.polymer.2006.06.002.

(22) Joseph, J.; Jemmis, E. D. Red-, Blue-, or No-Shift in Hydrogen Bonds: A Unified Explanation. *Journal of the American Chemical Society* **2007**, *129* (15), 4620–4632. https://doi.org/10.1021/ja067545z.

(23) Schultz, T.; Frey, N. C.; Hantanasirisakul, K.; Park, S.; May, S. J.; Shenoy, V. B.; Gogotsi, Y.; Koch, N. Surface Termination Dependent Work Function and Electronic Properties of Ti3C2Tx MXene. *Chem. Mater.* **2019**. https://doi.org/10.1021/acs.chemmater.9b00414.

(24) Hantanasirisakul, K.; Alhabeb, M.; Lipatov, A.; Maleski, K.; Anasori, B.; Salles, P.; Ieosakulrat, C.; Pakawatpanurut, P.; Sinitskii, A.; May, S. J.; Gogotsi, Y. Effects of Synthesis and Processing on Optoelectronic Properties of Titanium Carbonitride MXene. *Chemistry of Materials* **2019**, *31* (8), 2941–2951. https://doi.org/10.1021/acs.chemmater.9b00401.

(25) Sarycheva, A.; Polemi, A.; Liu, Y.; Dandekar, K.; Anasori, B.; Gogotsi, Y. 2D Titanium Carbide (MXene) for Wireless Communication. *Science Advances* **2018**, *4* (9). https://doi.org/10.1126/sciadv.aau0920.

(26) Hu, X.; Kaplan, D.; Cebe, P. Determining Beta-Sheet Crystallinity in Fibrous Proteins by Thermal Analysis and Infrared Spectroscopy. *Macromolecules* **2006**, *39* (18), 6161–6170. https://doi.org/10.1021/ma0610109.

(27) Chen, J.; Wang, X.; Dai, C.; Chen, S.; Tu, Y. Adsorption of GA Module onto Graphene and Graphene Oxide: A Molecular Dynamics Simulation Study. *Physica E: Low-Dimensional Systems and Nanostructures* **2014**, *62*, 59–63. https://doi.org/10.1016/j.physe.2014.04.021.

(28) Hu, X.; Shmelev, K.; Sun, L.; Gil, E.-S.; Park, S.-H.; Cebe, P.; Kaplan, D. L. Regulation of Silk Material Structure by Temperature-Controlled Water Vapor Annealing. *Biomacromolecules* **2011**, *12* (5), 1686–1696. https://doi.org/10.1021/bm200062a.

(29) Zhang, C. J.; Pinilla, S.; McEvoy, N.; Cullen, C. P.; Anasori, B.; Long, E.; Park, S.-H.; Seral-Ascaso, A.; Shmeliov, A.; Krishnan, D.; Morant, C.; Liu, X.; Duesberg, G. S.; Gogotsi, Y.; Nicolosi, V. Oxidation Stability of Colloidal Two-Dimensional Titanium Carbides (MXenes). *Chemistry of Materials* **2017**, *29* (11), 4848–4856. https://doi.org/10.1021/acs.chemmater.7b00745.

(30) Maleski, K.; Ren, C. E.; Zhao, M.-Q.; Anasori, B.; Gogotsi, Y. Size-Dependent Physical and Electrochemical Properties of Two-Dimensional MXene Flakes. *ACS Applied Materials and Interfaces* **2018**, *10* (29), 24491–24498. https://doi.org/10.1021/acsami.8b04662.

(31) Kumar, A.; Khandelwal, M. Amino Acid Mediated Functionalization and Reduction of Graphene Oxide-Synthesis and the Formation Mechanism of Nitrogen-Doped Graphene. *New Journal of Chemistry* **2014**, *38* (8), 3457–3467. https://doi.org/10.1039/c4nj00308j.

(32) Ming, J.; Zuo, B. Silk i Structure Formation through Silk Fibroin Self-Assembly. *Journal of Applied Polymer Science* **2012**, *125* (3), 2148–2154. https://doi.org/10.1002/app.36354.

(33) Khalil, H. A.; Davoudpour, Y.; Islam, M. N.; Mustapha, A.; Sudesh, K.; Dungani, R.; Jawaid, M. Production and Modification of Nanofibrillated Cellulose Using Various Mechanical Processes: A Review. *Carbohydrate Polymers* **2014**, *99*, 649–665.

(34) Kuila, T.; Mishra, A. K.; Khanra, P.; Kim, N. H.; Lee, J. H. Recent Advances in the Efficient Reduction of Graphene Oxide and Its Application as Energy Storage Electrode Materials. *Nanoscale* **2013**, *5* (1), 52–71. https://doi.org/10.1039/c2nr32703a.

(35) Xu, S.; Yong, L.; Wu, P. One-Pot, Green, Rapid Synthesis of Flowerlike Gold Nanoparticles/Reduced Graphene Oxide Composite with Regenerated Silk Fibroin as Efficient Oxygen Reduction Electrocatalysts. *ACS Applied Materials and Interfaces* **2013**, *5* (3), 654–662. https://doi.org/10.1021/am302076x.

(36) Jiang, C.; Wang, X.; Gunawidjaja, R.; Lin, Y.-H.; Gupta, M. K.; Kaplan, D. L.; Naik, R. R.; Tsukruk, V. V. Mechanical Properties of Robust Ultrathin Silk Fibroin Films. *Advanced Functional Materials* **2007**, *17* (13), 2229–2237. https://doi.org/10.1002/adfm.200601136.

(37) Keten, S.; Xu, Z.; Ihle, B.; Buehler, M. J. Nanoconfinement Controls Stiffness, Strength and Mechanical Toughness of Beta-Sheet Crystals in Silk. *Nat Mater* **2010**, *9* (4), 359–367. https://doi.org/10.1038/nmat2704.

(38) Chen, X.; Shao, Z.; Marinkovic, N. S.; Miller, L. M.; Zhou, P.; Chance, M. R. Conformation Transition Kinetics of Regenerated Bombyx Mori Silk Fibroin Membrane Monitored by Time-Resolved FTIR Spectroscopy. *Biophysical Chemistry* **2001**, *89* (1), 25–34. https://doi.org/10.1016/S0301-4622(00)00213-1.

(39) Cheng, L.; Thomas, A.; Glancey, J. L.; Karlsson, A. M. Mechanical Behavior of Bio-Inspired Laminated Composites. *Composites Part A: Applied Science and Manufacturing* **2011**, *42* (2), 211–220. https://doi.org/10.1016/j.compositesa.2010.11.009.

(40) Yan, J.; Ren, C. E.; Maleski, K.; Hatter, C. B.; Anasori, B.; Urbankowski, P.; Sarycheva, A.; Gogotsi, Y. Flexible MXene/Graphene Films for Ultrafast Supercapacitors with Outstanding Volumetric Capacitance. *Advanced Functional Materials* **2017**, *27* (30). https://doi.org/10.1002/adfm.201701264.

(41) Putz, K. W.; Compton, O. C.; Segar, C.; An, Z.; Nguyen, S. T.; Brinson, L. C. Evolution of Order during Vacuum-Assisted Self-Assembly of Graphene Oxide Paper and Associated Polymer Nanocomposites. *ACS Nano* **2011**, *5* (8), 6601–6609. https://doi.org/10.1021/nn202040c.

(42) Ling, Z.; Ren, C. E.; Zhao, M.-Q.; Yang, J.; Giammarco, J. M.; Qiu, J.; Barsoum, M. W.; Gogotsi, Y. Flexible and Conductive MXene Films and Nanocomposites with High Capacitance. *Proceedings of the National Academy of Sciences of the United States of America* **2014**, *111* (47), 16676–16681. https://doi.org/10.1073/pnas.1414215111.

(43) Zhao, X.; Vashisth, A.; Prehn, E.; Sun, W.; Shah, S. A.; Habib, T.; Chen, Y.; Tan, Z.; Lutkenhaus, J. L.; Radovic, M.; Green, M. J. Antioxidants Unlock Shelf-Stable Ti3C2Tx (MXene) Nanosheet Dispersions. *Matter* **2019**, *1* (2), 513–526. https://doi.org/10.1016/j.matt.2019.05.020.

(44) Mirkhani, S. A.; Shayesteh Zeraati, A.; Aliabadian, E.; Naguib, M.; Sundararaj, U. High Dielectric Constant and Low Dielectric Loss via Poly(Vinyl Alcohol)/Ti3C2Tx MXene Nanocomposites. *ACS Applied Materials and Interfaces* **2019**, *11* (20), 18599–18608. https://doi.org/10.1021/acsami.9b00393.

(45) Zhang, J.; Kong, N.; Uzun, S.; Levitt, A.; Seyedin, S.; Lynch, P. A.; Qin, S.; Han, M.; Yang, W.; Liu, J.; Wang, X.; Gogotsi, Y.; Razal, J. M. Scalable Manufacturing

of Free-Standing, Strong Ti3C2Tx MXene Films with Outstanding Conductivity. *Advanced Materials* **2020**, *32* (23). https://doi.org/10.1002/adma.202001093.

(46) Marsden, A. J.; Papageorgiou, D. G.; Vallés, C.; Liscio, A.; Palermo, V.; Bissett, M. A.; Young, R. J.; Kinloch, I. A. Electrical Percolation in Graphene-Polymer Composites. *2D Materials* **2018**, *5* (3). https://doi.org/10.1088/2053-1583/aac055.

(47) Hu, K.; Xiong, R.; Guo, H.; Ma, R.; Zhang, S.; Wang, Z. L.; Tsukruk, V. V. Self-Powered Electronic Skin with Biotactile Selectivity. *Advanced Materials* **2016**, *28* (18), 3549–3556. https://doi.org/10.1002/adma.201506187.

(48) Pandey, R. P.; Rasool, K.; Madhavan, V. E.; Aïssa, B.; Gogotsi, Y.; Mahmoud, K. A. Ultrahigh-Flux and Fouling-Resistant Membranes Based on Layered Silver/MXene (Ti3C2Tx) Nanosheets. *J. Mater. Chem. A* **2018**, *6* (8), 3522–3533. https://doi.org/10.1039/C7TA10888E.

(49) Kang, K. M.; Kim, D. W.; Ren, C. E.; Cho, K. M.; Kim, S. J.; Choi, J. H.; Nam, Y. T.; Gogotsi, Y.; Jung, H.-T. Selective Molecular Separation on Ti3C2Tx-Graphene Oxide Membranes during Pressure-Driven Filtration: Comparison with Graphene Oxide and MXenes. *ACS Applied Materials and Interfaces* **2017**, *9* (51), 44687–44694. https://doi.org/10.1021/acsami.7b10932.

(50) Ling, S.; Jin, K.; Kaplan, D. L.; Buehler, M. J. Ultrathin Free-Standing Bombyx Mori Silk Nanofibril Membranes. *Nano Letters* **2016**, *16* (6), 3795–3800. https://doi.org/10.1021/acs.nanolett.6b01195.

(51) Shchepelina, O.; Drachuk, I.; Gupta, M. K.; Lin, J.; Tsukruk, V. V. Silk-on-Silk Layer-by-Layer Microcapsules. *Advanced Materials* **2011**, *23* (40), 4655–4660. https://doi.org/10.1002/adma.201102234.

(52) Ye, C.; Shchepelina, O.; Calabrese, R.; Drachuk, I.; Kaplan, D. L.; Tsukruk, V. V. Robust and Responsive Silk Ionomer Microcapsules. *Biomacromolecules* **2011**, *12* (12), 4319–4325. https://doi.org/10.1021/bm201246f.

(53) Hu, K.; Gupta, M. K.; Kulkarni, D. D.; Tsukruk, V. V. Ultra-Robust Graphene Oxide-Silk Fibroin Nanocomposite Membranes. *Advanced Materials* **2013**, *25* (16), 2301–2307. https://doi.org/10.1002/adma.201300179.

(54) Wang, Y.; Ma, R.; Hu, K.; Kim, S.; Fang, G.; Shao, Z.; Tsukruk, V. V. Dramatic Enhancement of Graphene Oxide/Silk Nanocomposite Membranes: Increasing Toughness and Strength via Annealing of Interfacial Structures. *ACS Appl. Mater. Interfaces* **2016**. https://doi.org/10.1021/acsami.6b08610.

CHAPTER 5. MULTILAYERED NANOCOMPOSITES FROM SILK MODIFIED MXENES

5.1 Introduction

Nature has continued to provide materials and inspiration for the fabrication of mechanically robust and nanocomposites with enhanced biocompatibility and novel functionalities. Functional bionanocomposites have been designed to have enhanced mechanical robustness and tunable properties by introducing strong two-dimensional materials into matrices of proteins that contain a wealth chemical structures that provide reinforcement through secondary structure changes, hydrogen bonding, and electrostatic interactions..[1,2] While these composites showcase systems for better integration of natural and synthetic components, through this "brick-and-mortar" construction, electrical conductivity is still difficult to maintain.[3] Typically, electrical conductivity is afforded by the two-dimensional component. However, surrounded by insulating mortar materials, the conductivity of the resulting composites is often compromised.

Several studies have shown graphene oxide and silk to be model systems for fabrication of these types of composites due to the tunability of silk structure and the abundance of hydrophilic surface groups providing the ability for aqueous proceesing.[4,5] However, in order to be electrically conductive, the graphene oxide component must be reduces post-processing to retain electrical conductivity.[6,7] In the previous chapter, we explore the use of another two-dimensional component, MXene, in multilayered composites with silk. MXene has an intrinsically high electrical conductivity despite having hydrophilic surface groups making it an ideal candidate for solution processing of

electrically conductive bionanocomposites.[8,9] Despite a composition of nearly 75% silk, the fabricated composite can still retain a conductivity of 5940 S m^{-1} without requiring post processing techniques. Armed with new insights into the secondary structure changes of silk when co-assembled with MXene and retained electrical properties of the resulting composites, we set out to study the mechanical properties of such systems with varied secondary structure and silk content.

5.2 Experimental Details

5.2.1 Solution Processing

Once suspensions of MXene were obtained, the concentrations were determined by filtering a known amount of solution through a previously weighed filter.[10] A solution of 0.4 mg/mL was made using this method and then measured using UV-Vis for future concentration measurements. Solutions of 0.36 mg/mL and 0.15 mg/mL were made for use in spin casting and vacuum filtration, respectively.

MXene solutions of 0.15 mg/mL were altered to have a pH above 10 using 10 wt% sodium hydroxide while stirring. A concentrated silk solution was then added dropwise to the stirring suspension slowly to avoid aggregation. Different amounts of silk solution were added to create solute contents of 2.5 wt%, 5 wt%, and 7.5 wt% of silk while each solution contained 12.1 mg of MXene. After 10 minutes, the solution was used for making vacuum filtered films.

5.2.2 Buckling Mechanical Testing

Since the lateral size of the 2D nanosheets are on the micron scale, buckling must be used to elucidate mechanical properties of single nanosheets. Nanosheets are deposited via spin casting at 3000 rpm for 30 seconds onto acid treated polydimethylsiloxane (PDMS) substrates. PDMS precursor (Dow Corning Sylgard 184) and a curing agent were mixed in a 10:1 weight ratio and poured over a thermally oxidized silicon wafer inside a petri dish. The system was then degassed in vacuum and then placed in an oven a 70 ° for 6 hours to cure. The cured PDMS was cut with free razors into 1cm by 1 cm squares, peeled off the silicon wafer, and placed bottom side up in 10 v/v% hydrochloric acid for 16 hours to induce hydrophilic surface. The PDMS was rinsed in water, placed onto a silicon wafer with double sided tape, and then spin cast at 3000 rpm for 30 seconds with the desired solution.

The deposited nanosheets were imaged using AFM to determine thickness, then compressed 30% and imaged again to determine periodicity.[11–15] The thickness of the nanosheets was obtained using the depth function in NanoScope Analysis 2.0 and the distance between wrinkles induced upon compression was measured using the sectioning tool. Elastic modulus values were obtained by using the following equation:[11]

$$\lambda = 2\pi d \left[\frac{E_f(1-v_s^2)}{3E_s(1-v_f^2)}\right]^{1/3}$$

where λ, d, E_f, E_s, v_f, and v_s are the periodic wavelength, thickness of the nanosheet, elastic modulus of the nanosheet, elastic modulus of the PDMS, Poissan's ratio of the nanosheet, and Poissan's ratio of the PDMS, respectively. The modulus of the PDMS was found to be

3.13 MPa using compression tests. The Poissan's ratio entered for the PDMS and nanosheet are 0.5 and 0.3, respectively.

5.2.3 Tensile Mechanical Testing

Bulk mechanical properties of each material were measured using tensile testing. Composites of each component were made by vacuum filtering solutions of 0.15 mg MX/mL through membranes on a glass setup with nylon membranes for support. Both SFMX films were made with solutions containing 5.23 mg MX confirmed using UV-Vis measurements. The mass deposited for the fresh and older SFMX solutions were 13.67 mg and 14.45 mg, respectively, indicating films of approximately 73 wt% silk. The same amount of MXene in solution without silk proved too little to create films for tensile testing so 19 mg of MXene was used to create a thicker film for comparison to the SFMX systems.

Vacuum assisted filtration fabricated multilayered composites were cut into 3 mm by 27 mm strips and glued to precut paper substrates dried overnight. The substrates cut into 34 mm X 20 mm pieces and hole punched to have 2.54 cm^2 squares in the center. Samples were placed on a Shimadzu EZ-SX tester machine, the edges of the supports were cut, and the samples were pulled uniaxially at a rate of 1 mm min^{-1} until break. The length and width of the samples were measured individually after each test while SEM imaging was used to determine the thicknesses.

5.3 Results and Discussion

5.3.1 Temperature Effects on Hybrid Nanosheets

As shown in the previous chapter, silk self- assembles into fibrils on top of MXene nanosheets while in solution for three weeks. To determine a quicker way of obtaining SFMX nanosheets with different silk morphologies while maintaining low oxidation of MXene, we studied the effects of temperature on their morphology. AFM images of SFMX kept at 35° C and

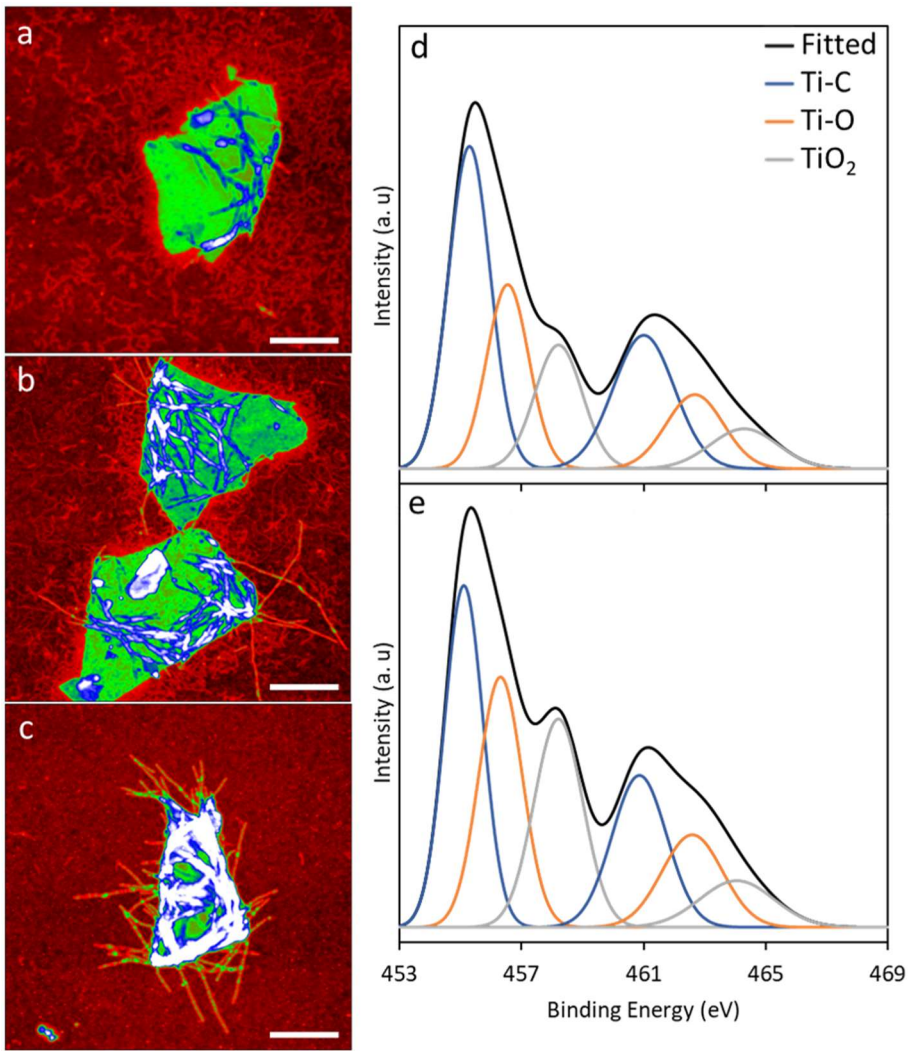

Figure 5.1. AFM images of SFMX nanosheets spun cast from solutions kept at 25°C (a), 35°C (b), and 50°C (c) for 24 hours and high-resolution titanium XPS spectra of fresh SFMX (d) and SFMX after 24 hours at 50°C. AFM image scale bars and z scales are 400 nm and 15 nm, respectively.

50° C (Figure 5.1) show that varying degrees of fibril formation can be obtained by using temperature as well. After just 24 hours in solution at 35°C, SFMX nanosheets have some fibrils formed with a silk corona present similar to SFMX kept at 4° C for three days shown in the last chapter. With 24 hours in solution at 50°C, SFMX shows little to no silk corona with mostly fibrils similar to nanosheets cast from solution after seven days at 4°C. This shows that the secondary structure of the silk on MXene nanosheets can restructure with exposure to elevated temperature as well as with time.

To determine the extent of possible oxidation, XPS spectra were obtained of fresh SFMX and SFMX after 24 hours at 50°C. High resolution scans of the titanium region reveal a composition of 51.2% Ti-C, 28.4% Ti-O, and 20.4% TiO_2 for fresh SFMX and 41.6%, 32%, and 26.4% for SFMX after a day at 50°C. Even at 50°C, the silk corona can still provide protection against oxidation of the MXene in aqueous solution.

5.3.2 Morphology and Mechanical Properties of Multilayered Composites

SEM imaging (Figure 5.2) reveals thicknesses of 4.7 ± 0.4 μm, 7.1 ± 0.6 μm, and 7.1 ± 0.2 μm, for MXene, SFMX, and SFMX D22 respectively indicating mass loads of 3.75 mg mm^{-3}, 1.79 mg mm^{-3}, and 1.88 mg mm^{-3}. All films show ordered lamellar structures in their cross sections. The composites with silk have more dense packing with less distinction between layers due to the addition of the silk protein.

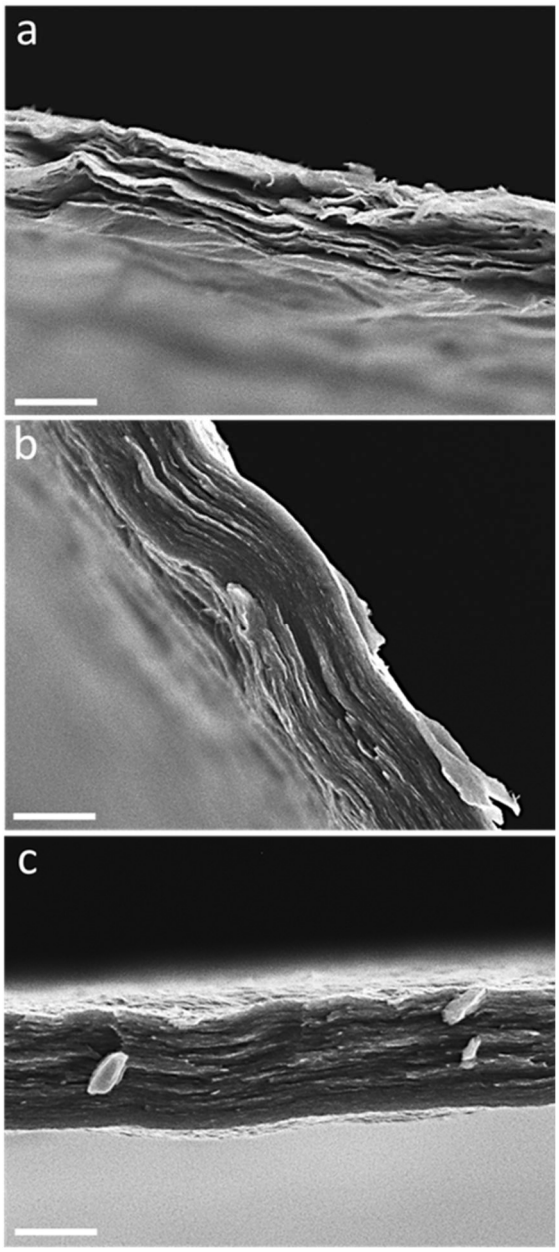

Figure 5.2 SEM images of papers made from pristine MXene (a), fresh SFMX (b) and SFMX after 22 days at 4°C. Scale bars are 5 µm.

Tensile tests of composites made from MXene and the hybrid components (Figure 5.3) show great differences in mechanical properties. Given that these composite films are collections of several nanosheets, the modulus, ultimate strain, and ultimate stress from tensile testing are considered sheared properties. The stress strain curves display properties

resulting from nanosheets moving past each other in a shear motion and do not represent the intrinsic properties of the nanosheets themselves. SFMX films have a shear modulus of 22.6 ± 3.9 GPa and ultimate strength of 109.2 ± 56.9 MPa while the MXene films only show a shear modulus and ultimate stress of 10.2 ± 2.9 GPa and 55.4 ± 14.4 MPa, respectively. Films made from day-22 SFMX show shear modulus and ultimate strength of 15.1 ± 5.2 GPa and 24.0 ± 16.8 MPa, respectively. This shows that the silk encapsulation does enhance the mechanical properties of the films. However, the SFMX films show a lower strain to break than pristine MXene with fibrillar silk-MXene severely reduced. This is likely due to the lack of amorphous silk available to glue the stiffer fibrillar nanosheets together creating more brittle films. Small amounts of silk (less than 10%) have shown to enhance the mechanical properties of graphene oxide films while larger amounts show less of a positive effect.[6]

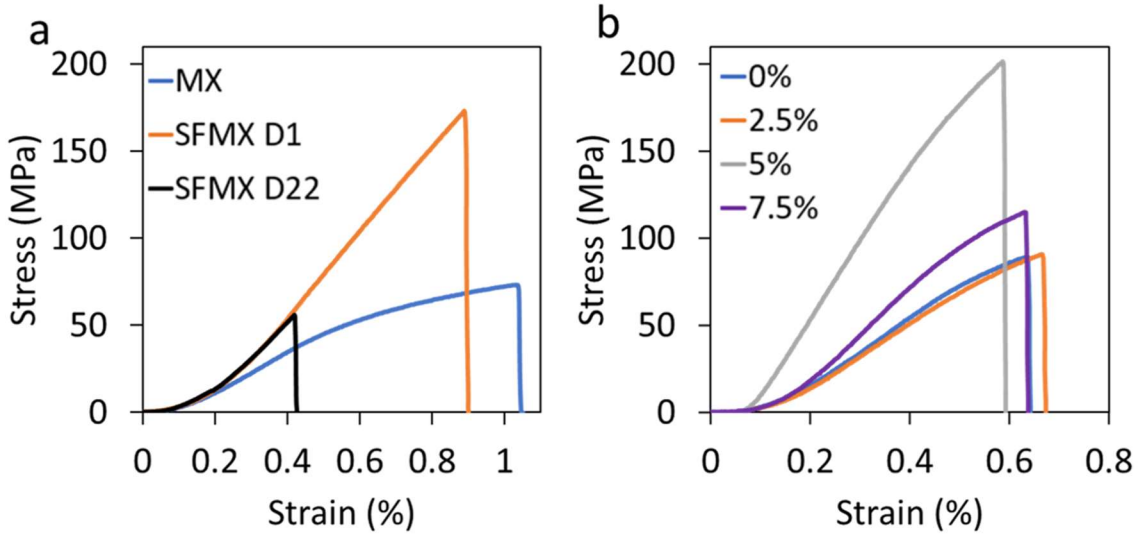

Figure 5.3 Stress-strain curves from tensile tests of pristine MXene, fresh SFMX, and SFMX from day 22 (a) and composites made with varying weight per cent concentrations of silk (b).

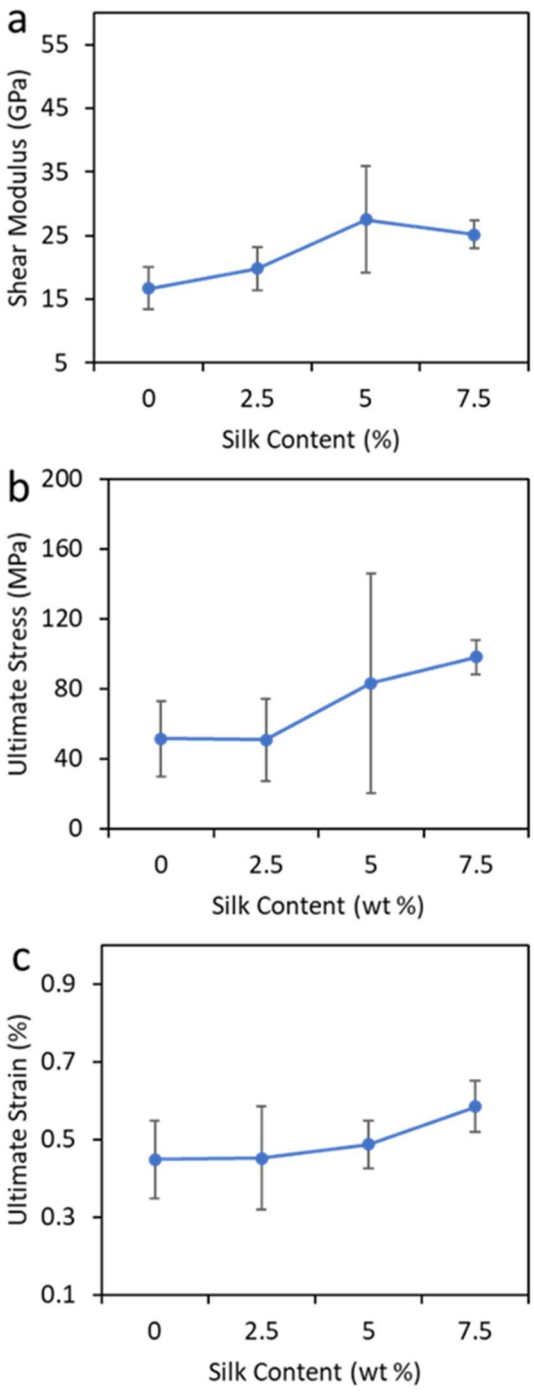

Figure 5.4 Plots containing values of shear modulus (a), ultimate stress (b), and ultimate strain (c) obtained from tensile tests of MXene silk composites at different weight per cents of silk.

To examine the effect of silk concentration on mechanical properties of these composites, MXene composite films were made with varying concentrations of silk (0%, 2.5%, 5%, and 7.5%). Each film was made using 12.1 mg of MXene in solution as confirmed using UV-Vis measurements. The MXene solutions were diluted to 0.15 mg/mL and then their pH was adjusted to above 10 before being mixed with silk fibroin solution.

Tensile tests of films made (Figure 5.3) show that increasing silk concentration increases ultimate stress and strain producing more ductile films. However, the shear modulus only increases with concentration up to 5 wt% silk and then begins to decline again. However, ultimate stress and strain continues to increase up to 7.5 wt% silk (Figure 5.4). This is likely due to the enhanced extensibility brought by the higher concentration of the silk fibroin. During tension, the silk can unravel and extend while still adhering to the synthetic component thus allowing the films to undergo higher strain without irreversible damage.

5.3.2 Mechanical Properties of Individual Nanosheets

To investigate the micromechanical properties of the individual nanosheets, the common buckling test was used to calculate the compressive elastic modulus. Suspensions of MXene and SFMX were spun cast onto PDMS substrates previously treated in 10 v/v% hydrochloric acid for 16 hours to render the surface more hydrophilic. Compression of the PDMS produces periodic wrinkles parallel to the direction of stress.[11,13] AFM images of pristine MXene, fresh SFMX, and 22-day old SFMX on PDMS before compression reveal thicknesses of 5.0 ± 1.4 nm, 8.1 ± 0.7 nm, and 22.7 ± 2.9 nm (Figure 5.5). This is significantly higher than the thicknesses of 1.6 ± 0.1 nm, 7.6 ± 0.3, and 11.6 ± 1.2 nm

obtained in the previous study with MXene, SFMX, and 22-day old SFMX on silicon substrates. Silk encapsulated MXene nanosheets show an average wavelength of 445 ± 61.4 nm which is much larger than the average distance of 209.6 ± 43.8 nm between peaks that pristine MXene presents. Using the equation outlined in the experimental section, the

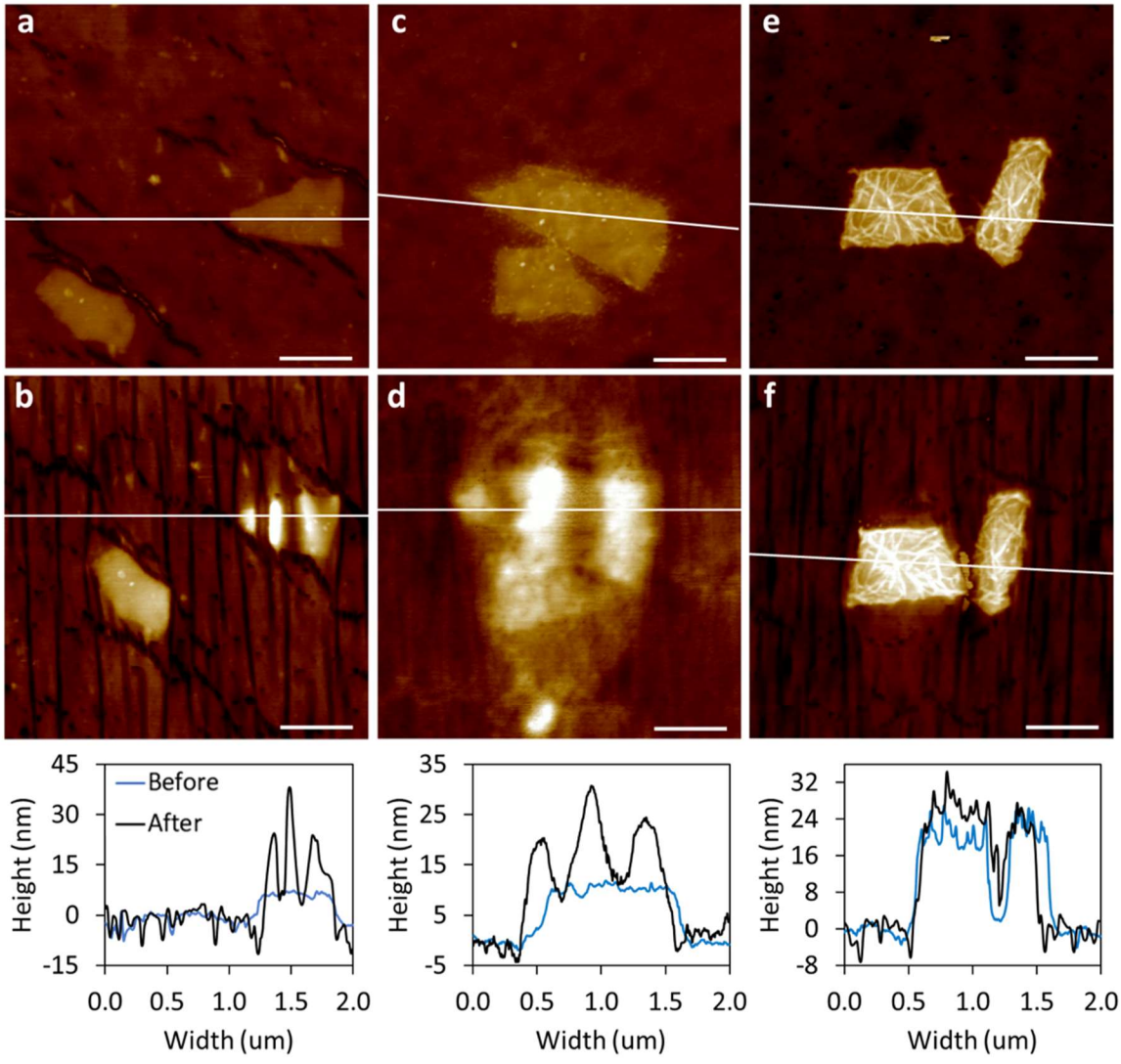

Figure 5.5 AFM images and corresponding height profiles (bottom) of pristine MXene (a, b), fresh SFMX (c, d), and SFMX after day 22 days at 4°C (e, f) on PDMS substrates before (a, c, d) and after (b, d, f) 30% uniaxial compression. Scale bars are 400 nm, and the z scale is 40 nm.

MXene and SFMX nanosheets were calculated to have compressive moduli of 3.7 ± 2.1 GPa and 8.0 ± 3.0 GPa, respectively. The high variability in these values is attributed to the differences in thickness between individual nanosheets. SFMX nanosheets that have formed fibrils do not show a wavelength pattern due to their strength and small lateral size. These results show that the silk encapsulation causes a higher buckling modulus in both cases with fibrils significantly impacting the bendability of the MXene.

5.4 Conclusion

Amorphous silk encapsulated MXene showed enhanced modulus and ultimate stress due to the silk acting as glue for the brick-like 2D nanosheets. Buckling tests revealed moduli values of 3.7 ± 2.1 GPa and 8.0 ± 3.0 GPa, for single MXene and SFMX nanosheets, respectively. These tests also showed that fibrillar silk modified MXene is nearly incompressible on the small length scale. Tensile testing of multilayered composites of MXene encapsulated with amorphous and fibrillar silk displayed shear moduli values of 22.6 ± 3.9 GPa and 15.1 ± 5.2 GPa, respectively, which are 2 and 1.5 times that of 10.2 ± 2.9 GPa obtained from MXene only films. The SFMX films also displayed higher ultimate strength, but those with the fibrillar morphology had a significantly reduced ultimate strength and strain.

Considering the stiffness seen during buckling tests and the lack of amorphous silk seen in AFM imaging, it is likely that the higher modulus is attributed to the increased strength of the individual SFMX nanosheets, but the lack of amorphous silk for adhesion between components reducing efficient load transfer and stress mediation. Typically, proteins enhance mechanical properties of composite films through the stretching and

reorientation of their secondary structure resulting in reduced crack propagation via energy absorption. However, this requires that the protein have strong interfacial interactions with the synthetic component. SFMX nanosheets with most of the silk self-assembled into fibrils on top of the MXene nanosheets cannot form these strong interactions to other nanosheets in the matrix. Thus, it is important to determine the level of silk reorganization before use in fabricating bulk composite films. Bionanocomposites made by simply mixing silk and MXene at different ratios reveal that small amounts of silk, 2.5, 5, and 7.5 wt % can significantly enhance the mechanical properties of organized multilayered MXene composites.

5.5 References

(1) Xiong, R.; Grant, A. M.; Ma, R.; Zhang, S.; Tsukruk, V. V. Naturally-Derived Biopolymer Nanocomposites: Interfacial Design, Properties and Emerging Applications. *Materials Science and Engineering R: Reports* **2018**, *125*, 1–41. https://doi.org/10.1016/j.mser.2018.01.002.

(2) Grant, A. M.; Kim, H. S.; Dupnock, T. L.; Hu, K.; Yingling, Y. G.; Tsukruk, V. V. Silk Fibroin–Substrate Interactions at Heterogeneous Nanocomposite Interfaces. *Advanced Functional Materials* **2016**, *26* (35), 6380–6392. https://doi.org/10.1002/adfm.201601268.

(3) Tang, Z.; Kotov, N. A.; Magonov, S.; Ozturk, B. Nanostructured Artificial Nacre. *Nature Materials* **2003**, *2* (6), 413–418. https://doi.org/10.1038/nmat906.

(4) Wang, Y.; Ma, R.; Hu, K.; Kim, S.; Fang, G.; Shao, Z.; Tsukruk, V. V. Dramatic Enhancement of Graphene Oxide/Silk Nanocomposite Membranes: Increasing Toughness and Strength via Annealing of Interfacial Structures. *ACS Appl. Mater. Interfaces* **2016**. https://doi.org/10.1021/acsami.6b08610.

(5) Yin, Y.; Hu, K.; Grant, A. M.; Zhang, Y.; Tsukruk, V. V. Biopolymeric Nanocomposites with Enhanced Interphases. *Langmuir* **2015**, *31* (39), 10859–10870. https://doi.org/10.1021/acs.langmuir.5b02744.

(6) Hu, K.; Tolentino, L. S.; Kulkarni, D. D.; Ye, C.; Kumar, S.; Tsukruk, V. V. Written-in Conductive Patterns on Robust Graphene Oxide Biopaper by Electrochemical Microstamping. *Angew. Chem. Int. Ed.* **2013**, *52* (51), 13784–13788. https://doi.org/10.1002/anie.201307830.

(7) Ma, R.; Tsukruk, V. V. Seriography-Guided Reduction of Graphene Oxide Biopapers for Wearable Sensory Electronics. *Advanced Functional Materials* **2017**, *27* (10). https://doi.org/10.1002/adfm.201604802.

(8) Naguib, M.; Mochalin, V. N.; Barsoum, M. W.; Gogotsi, Y. 25th Anniversary Article: MXenes: A New Family of Two-Dimensional Materials. *Advanced Materials* **2014**, *26* (7), 992–1005. https://doi.org/10.1002/adma.201304138.

(9) Ling, Z.; Ren, C. E.; Zhao, M.-Q.; Yang, J.; Giammarco, J. M.; Qiu, J.; Barsoum, M. W.; Gogotsi, Y. Flexible and Conductive MXene Films and Nanocomposites with High Capacitance. *Proceedings of the National Academy of Sciences of the United States of America* **2014**, *111* (47), 16676–16681. https://doi.org/10.1073/pnas.1414215111.

(10) Alhabeb, M.; Maleski, K.; Anasori, B.; Lelyukh, P.; Clark, L.; Sin, S.; Gogotsi, Y. Guidelines for Synthesis and Processing of Two-Dimensional Titanium Carbide (Ti 3 C 2 T x MXene). *Chemistry of Materials* **2017**, *29* (18), 7633–7644. https://doi.org/10.1021/acs.chemmater.7b02847.

(11) Stafford, C. M.; Harrison, C.; Beers, K. L.; Karim, A.; Amis, E. J.; Vanlandingham, M. R.; Kim, H.-C.; Volksen, W.; Miller, R. D.; Simonyi, E. E. A Buckling-Based Metrology for Measuring the Elastic Moduli of Polymeric Thin Films. *Nature Materials* **2004**, *3* (8), 545–550. https://doi.org/10.1038/nmat1175.

(12) Hu, K.; Gupta, M. K.; Kulkarni, D. D.; Tsukruk, V. V. Ultra-Robust Graphene Oxide-Silk Fibroin Nanocomposite Membranes. *Advanced Materials* **2013**, *25* (16), 2301–2307. https://doi.org/10.1002/adma.201300179.

(13) Kunz, D. A.; Feicht, P.; Gödrich, S.; Thurn, H.; Papastavrou, G.; Fery, A.; Breu, J. Space-Resolved in-Plane Moduli of Graphene Oxide and Chemically Derived Graphene Applying a Simple Wrinkling Procedure. *Advanced Materials* **2013**, *25* (9), 1337–1341. https://doi.org/10.1002/adma.201204049.

(14) Xiong, R.; Kim, H. S.; Zhang, L.; Korolovych, V. F.; Zhang, S.; Yingling, Y. G.; Tsukruk, V. V. Wrapping Nanocellulose Nets around Graphene Oxide Sheets. *Angewandte Chemie - International Edition* **2018**, *57* (28), 8508–8513. https://doi.org/10.1002/anie.201803076.

(15) Iguiñiz, N.; Frisenda, R.; Bratschitsch, R.; Castellanos-Gomez, A. Revisiting the Buckling Metrology Method to Determine the Young's Modulus of 2D Materials. *Advanced Materials* **2019**, *31* (10), 1807150. https://doi.org/10.1002/adma.201807150.

CHAPTER 6. SUCKERIN-12 ENCAPSULATED MXENE STABILITY VIA HOFMEISTER SALT ANNEALING

6.1 Introduction

After having investigated the interactions between silk fibroin and MXene and the resulting mechanical reinforcements of their combination, we chose to build a similar system with another component to determine if other proteins react similarly to the surface of MXene. We chose to investigate suckerin-12 protein due to its similarity in structure to silk fibroin and high expression from *E. Coli*. Suckerin-12 is one of 35 isoforms in a family of modular proteins with β-sheet dominated structures that form the sucker ring teeth (SRT) of cephalopods through hydrophobic and hydrogen-bonding interations.[1] These suckerin proteins provide high hydrated and dry moduli of 4 GPa and 8 GPa, respectively, to the SRT indicating that they could be used as a reinforcing component in multilayered composites without the need for crosslinking.[2,3,4]

Interestingly, this protein forms heterogeneous structures with isotopically oriented β-sheets from organization of histidine, alanine and threonine components immersed in an amorphous matrix of glycine, tyrosine, and leucine.[5] We used the 27 kDa suckerin-12 isoform tagged with hexahistidine. The chemical of this protein has been shown to contain 29%, 15%, 12%, and 8% of glycine, tyrosine, alanine, and histidine, respectively.[6] Histidine typically aids self-assembly at higher pH and solubility at lower pH allowing for tunable control in secondary structure. Given the relative lack of knowledge on the nanoscale morphology and structural changes in response to external triggers,[6] we first studied the protein by itself on hydrophilic silicon substrates before finally assembling it

with MXene flakes. Considering that the natural environment of the Humboldt squid is the ocean, we contemplate the role of salts on the assembly of suckerin-12.

6.2 Experimental Details

6.2.1 Materials

The Hofmeister salts ($NaC_2H_3O_2$, $Na_3C_6H_5O_7$, Na_3PO_4, Na_2SO_4) were obtained from Sigma Aldrich and the suckerin-12 open reading frame was obtained from Genescript. Suckerin-12 expression and purification were conducted as discussed in prior work.[6] Briefly, the suckerin-12 fraction in purified bacterial inclusion body fractions was solubilized after acidification to pH 3 with HCl. After centrifugation, the resulting supernatant was adjusted to pH 8 with 1 M Tris HCl, pH 8, 100 mM NaCl. After centrifugation, the precipitate was washed twice in 80% ethanol, dried, weighed, and then resuspended in water at a concentration of 6 wt/vol%. Then, the pH was lowered to 3 with glacial acetic acid followed by dialysis overnight in water and then lyophilization. Dried protein was stored at −80 °C and resuspended in water and adjusted to pH 5 with glacial acetic acid for immediate use.

6.2.2 Sample Preparation

Suckerin-12 was either drop or spin-cast at 3000 rpm for 30 s at 1 and 3 wt. % to produce homogenous films. Spin cast films of suckerin-12 were then treated with Hofmeister salts at 100 mM or 200mM for varied periods of time then rinsed off with Millipore water and air dried.

6.2.3 Characterization

Attenuated total reflectance Fourier transform infrared spectroscopy (ATR-FTIR) was used to investigate the chemical composition and secondary structure of the suckerin-12 as deposited on an attenuated total reflectance crystal. OriginPro 8.5 software was used to deconvolute peaks in the amide I (1591 cm^{-1} to 1716 cm^{-1}) region using the "Fit Peaks (Pro)" function. User defined baseline subtraction with points connected by interpolation was completed, the most common 6 peaks found via the second derivative search method were used as starting peaks, and gaussian fits applied (see detailed data on deconvolution in SI).

AFM images of drop and spin cast films from 1 and 3 wt% were acquired using ultra-sharp tips with resonance frequency 325 kHz and spring constant 40 N m^{-1}. A softer ultra-sharp tip with spring constant 2.7 N m^{-1} was used for the samples prepared from 0.1 wt% suckerin-12 and MXenes. Most other AFM associated images were acquired using tapping mode tips whose average spring constants and resonant frequencies were 0.2 - 40 N m-1 and 15 - 350 Hz, respectively.

Sample thickness was measured using AFM of scratched films and with a Woollam M2000U variable-angle spectroscopic ellipsometer.[7] Optical images were obtained using a Leica DM 4000M microscope to evaluate macroscopic morphology changes and large-scale phase separation.

6.3 Results and Discussion

6.3.1 Composition and Deposition Mode Dependent Suckerin-12 Thin Film Formation

Considering its high levels of expression in *E. coli,*[6] suckerin-12 tagged with hexahistidine was used for this study. To begin our studies into this novel protein, we began with drop and spin cast suckerin-12 films from 1 and 3 wt% aqueous solutions. AFM imaging revealed relatively low roughness values of 0.40 ± 0.08 nm and 0.90 ± 0.5 for drop and spin cast films, respectively, from 1 wt% solutions. The films show globular structure with some larger aggregates present in the drop cast films. Spin cast films from 3 wt % solutions displayed larger scale aggregates and globules than films made from 1 wt%. These films also showed de-wetting patterns likely due to the higher viscosity of the more concentrated solution and a resulting larger roughness of 1.8 ± 0.1 nm.

To study the secondary structure changes, we used ATR-FTIR on the films and focused on the amide I peak centered in the range between 1600 and 1700 cm^{-1} (Figure 6.1, B.1). This range, representative of amine bonding, contains absorptions between 1605-1621 cm^{-1}, 1622-1637 cm^{-1}, 1638-1655 cm^{-1}, 1656-1662 cm^{-1}, and 1663-1696 cm^{-1} that are characteristic of β-sheets/aggregates, β-sheets, random coils, α-helices, and β-turns, respectively (Figure 6.1).[8,9] The spectra of each sample was deconvoluted uniformly with user defined background subtraction, consistent selection of six peaks, and fitted with Gaussian functions to determine precise compositions of the various secondary structures (Figure B.2).

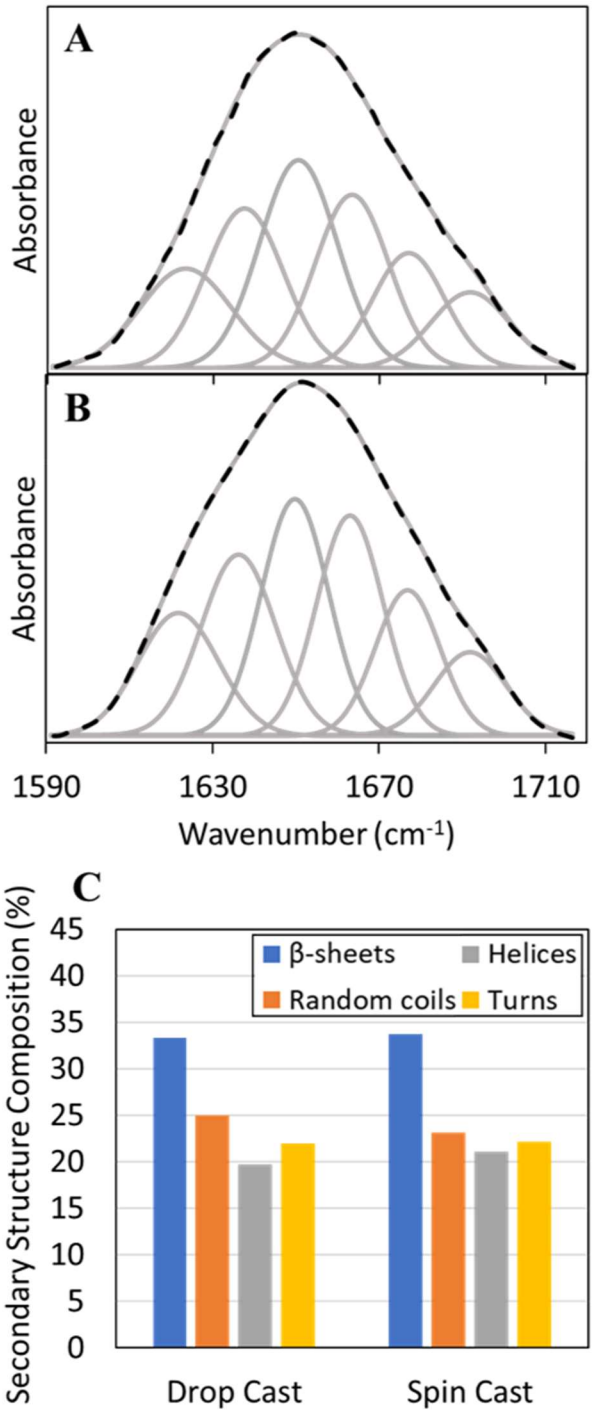

Figure 6.1 ATR-FTIR of drop (A) and spin cast (B) 1 wt% suckerin-12 where deconvoluted peaks are displayed under the overall amide 1 peak to show how ATR-FTIR spectra were analyzed. The secondary structure in each sample calculated from peak area of their respective peaks is given in (C).

The spectra of both drop and spin cast suckerin-12 displayed structures mostly composed of β-sheets and random coils with the spin cast. However, the drop cast film showed slightly less β-sheets than the spin cast film with a much higher percentage of random coils. From this technique, suckerin-12 is shown to have a relatively heterogenous structure as evident in the presence of a peak and a shoulder centered over 1650 cm^{-1} and 1625 cm^{-1} for random coils and β-sheets, respectively (Figure 6.1).

These results suggest that suckerin-12 can be spin cast to induce organization via shear forces similarly to silk fibroin.[10] Considering this similarity, it is reasonable to suggest that suckerin-12 also forms these β-sheets and other order structures from random coils when exposed to shear and rapid solvent removal.[11] Due to this shear induced organization of hydrogen bond enhanced secondary structures brought on by spin casting, the suckerin-12 is rendered more stable and less soluble in water than drop cast forms. Proof of secondary structure reorganization suggests that suckerin-12, despite being a smaller isoform in the suckerin protein family, can form similar structures observed in the native SRT.[29]

6.3.2 Hofmeister Salt Aided Suckerin-12 Stabilization and Assembly

Anions in different salts have shown to have larger affects than cations,[6] we chose to study the effects of different kosmotropic sodium salts in the Hofmeister series on the organization of suckerin-12. Exposure to most of the kosmotropic salts resulted in films with densely packed domains, rougher surfaces, and lower thicknesses than untreated suckerin-12 (Figure B.3). The suckerin-12 films started out with thicknesses of 74 nm, 83 nm, and 116 nm and changed to 70nm, 79 nm, and 102 nm after exposure to sodium

phosphate, sodium citrate, and sodium sulfate, respectively (Figure B.4). However, the film (66 nm thick) exposed to sodium acetate did not display contraction like those of the other salts.

ATR-FTIR of the same systems revealed that exposure to sodium phosphate, acetate, and citrate causes shifting of the major peak to 1642 cm^{-1} from 1650 cm^{-1} indicating increased β-sheet content (Figure 6.2). However, films exposed to sodium sulfate only displayed broadening of the 1650 cm^{-1} centered peak. Deconvolution of the amide I peaks confirmed that the salts had increased β-sheet content for sodium acetate, phosphate, citrate, and sulfate (in order of highest to lowest increase). Conversely, the suckerin-12 showed decreases in random coil content with sodium acetate exposed films showing the biggest decrease in random coils while sodium sulfate treated films had the lowest decrease. This reveals that exposure to these kosmotropic salts results in the random coils reorganizing into β-sheets.

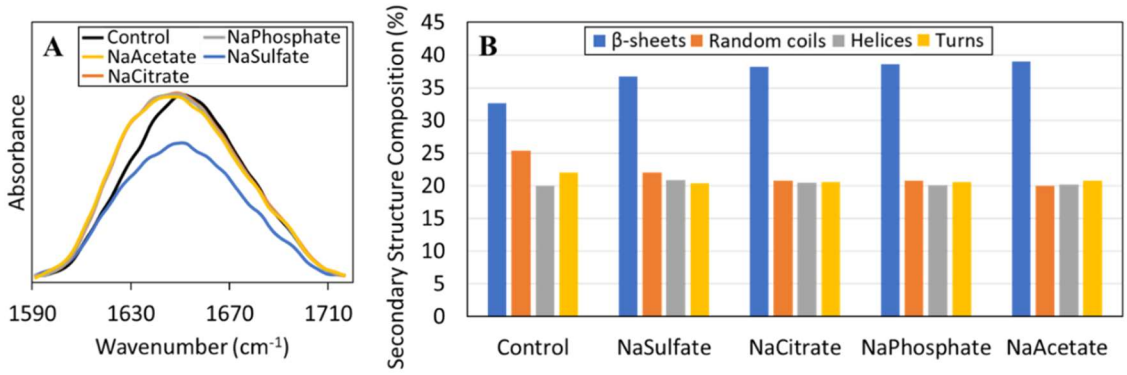

Figure 6.2 ATR-FTIR of the amide 1 peak of spin cast 1 wt% suckerin-12 films before (control) and after salt annealing for 1 hr (A) as well as a graph of the secondary structure composition derived from deconvolution of the spectra (B).

This smaller effect seen with sulfate salts is similar to those reported in literature for sukerin-12 hydrogel systems.[6,12] Similarly, suckerin hydrogels tend to form more β-sheets and display higher roughness and compressive moduli when exposed to salts with stronger conjugate bases.[13] Untreated suckerin-12 films dissolve relatively quickly in water with drop cast films dissolving almost immediately and spin cast films only lasting a few minutes. Treatment with kosmotropic salts, however, prevented the spin cast films from dissolving despite rinsing away excess salt indicating increased stability in aqueous environments.

To study the nanoscale morphology of the suckerin-12, high resolution AFM (HRAFM) imaging was done using a sharp tip with a 2 nm radius. The samples were made by dropping a solution of 0.1 wt% suckerin-12 onto thermally oxidized silicon wafers and then rinsed carefully with water and allowed to dry. HRAFM imaging reveals a bed of amorphous globular structure with a roughness of 0.4 ± 0.1 nm, similar to that measured for the thicker film, and some isolated fibrils measuring 2.5 ± 0.4 nm in height and 112 ± 20 nm in length. Despite previous thoughts that drop cast suckerin-12 fully dissolves when exposed to aqueous solution, this closer look at the morphology of drop cast suckerin-12 reveals this is not the entire story. It is likely that the films made from higher concentration suckerin-12 without rinsing dissolves in water due to a lack of cohesion within the layer but leaves a small layer of protein attached to the silicon substrate.

Using these thinner samples, we investigated the effect of salt annealing on the microstructure of this drop cast suckerin-12. After annealing in sodium sulfate, citrate, phosphate, and acetate, the suckerin-12 surface displayed roughness values of 0.3 ± 0.1 nm, 0.5 ± 0.1 nm, 1.1 ± 0.1 nm, and 0.4 ± 0.1 nm, respectively (Figure B.5). Similar to the

thicker spin cast films, the roughness increases when exposed to most of the salts. However, after soaking in sodium sulfate, the roughness decreases providing contrast to that seen in the spin cast films. When tethered to the surface of the silicon substrate, the phosphate treated films show a much higher roughness than the other salts.

6.3.3 Morphology of Suckerin-12-MXene Nanosheets

Considering that more β-sheet content corresponds to higher stability and modulus, it is reasonable to assume that suckerin-12 can enhance the mechanical properties of multilayered composites similar to silk fibroin. Thus, we studied the effects of suckerin-12 in contact with $Ti_3C_2T_x$ MXene with exposure to these same salts.

Similar to our silk studies, we investigated the affinity of suckerin-12 protein for MXene flakes. AFM imaging of the same flake before and after deposition of suckerin-12 reveals that the MXene flakes have an increased height and roughness with globules covering both the substrate and the flake indicating there is affinity between the two components (Figure 6.3). The apparent thickness of 1.9 ± 0.1 nm for the pristine flake suggests a single flake with interlocked water molecules. The difference in thickness before and after (2.3 ± 0.1 nm) deposition suggests the suckerin-12 has a different affinity for MXene than it does the silicon dioxide surface. The suckerin-12 covered flakes show an increase in roughness from 0.3 ± 0.1 nm to 0.7 ± 0.2 nm while the surrounding substrate only changes to 0.4 ± 0.1 nm from 0.2 ± 0.1 nm. Considering that an increase in roughness corresponds to an increase is β-sheets for pristine suckerin-12 shown in previous sections and literature,[13] it is likely that the MXene surface allows for more β-sheet formation and stability than the silicon dioxide surface of the substrate wafer.

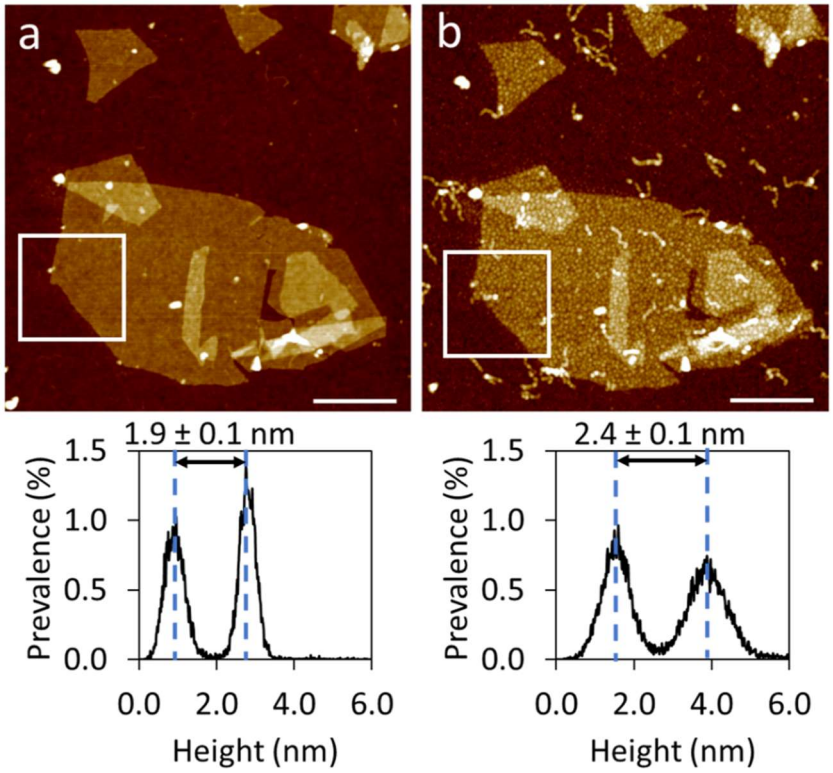

Figure 6.3 AFM topography images (top) and corresponding height histograms (bottom) of a pristine MXene flake before (a) and after (b) suckerin-12 deposition. Scale bars are 400 nm, and the z scale is 9 nm.

6.3.2 Manipulation of Secondary Structure of Suckerin-12 Using Salts

To determine if exposure to salt has a measurable effect using AFM imaging in this manner, we imaged similar flakes after exposure to sodium citrate and sodium sulfate after 1 hour and 11 days (Figure 6.4). After one hour of treatment in sodium citrate and sodium sulfate, the flakes showed thicknesses of 2.99 nm and 3.04 nm, respectively, and roughness values of 0.65 nm and 0.47 nm. After 11 days, the sodium sulfate treated flakes showed to be 2.4 nm thick with a roughness of 0.49 nm while the sodium citrate treated flakes show a decreased roughness of 0.47 nm while the suckerin-12 on the substrate seems to be pulling away from the flakes. Considering the higher roughness value and morphological

changed observed for flakes treated with citrate than those treated with sulfate salt, suckerin-12 adhered to MXene displays similar structural changes in response to salts as those previously studied.[6] This indeed shows that exposure to salt has a measurable effect on the morphology of drop deposited suckerin-12 when adhered to the surface of MXene flakes.

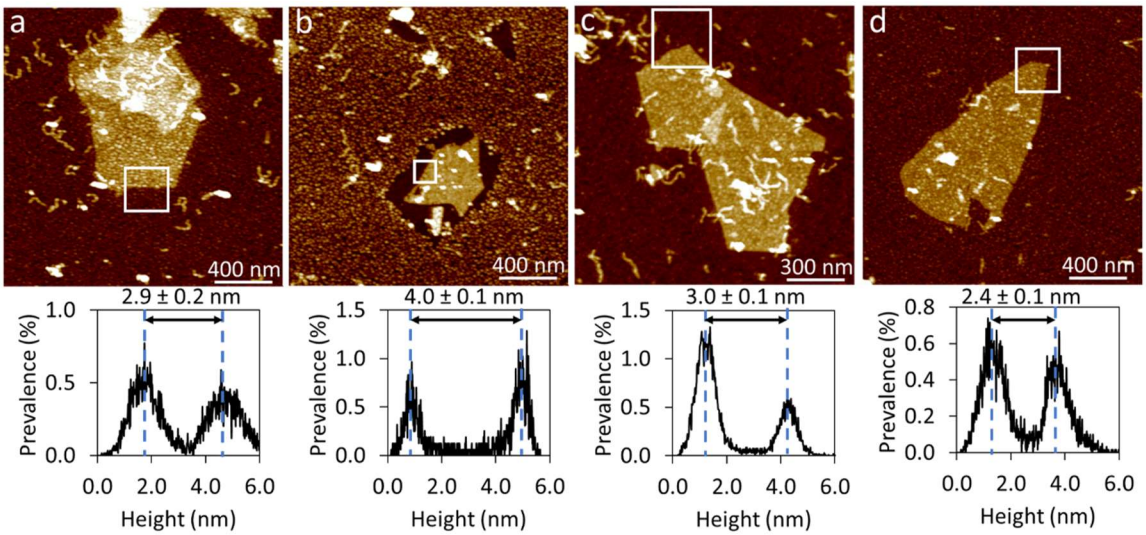

Figure 6.4 AFM topography images (top) and corresponding height histograms (bottom) of MXene flakes with suckerin deposited after soaking in 100m M sodium citrate (a, b) and 100mM sodium sulfate (c, d) for one hour (a, c) and 11 days (b, d). Z scale is 9 nm.

To get a better understanding of the microstructure of suckerin-12 adhered to MXene, we use HRAFM to image the coated flakes when exposed to the different salt environments for 16 hours to compare with similar conditions for suckerin-12 on silicon substrate discussed previously (Figure 6.5). Suckerin-12 adhered to MXene after treatment in sodium sulfate, citrate, phosphate, and acetate have roughness values of 0.26 ± 0.01 nm, 0.50 ± 0.08 nm, 1.10 ± 0.04 nm, and 0.37 ± 0.01 nm, respectively. Sodium sulfate treated

suckerin-12 again has the lowest roughness while sodium phosphate has the highest. The trend is similar for both the silicon substrate and MXene flake, but the roughness is much higher on MXene showing increased inhomogeneity caused by a higher degree of structural changes. All conditions show a decrease in thickness except treatment with sodium acetate. This could be due to contraction of the suckerin-12 as seen in previous studies.[6]

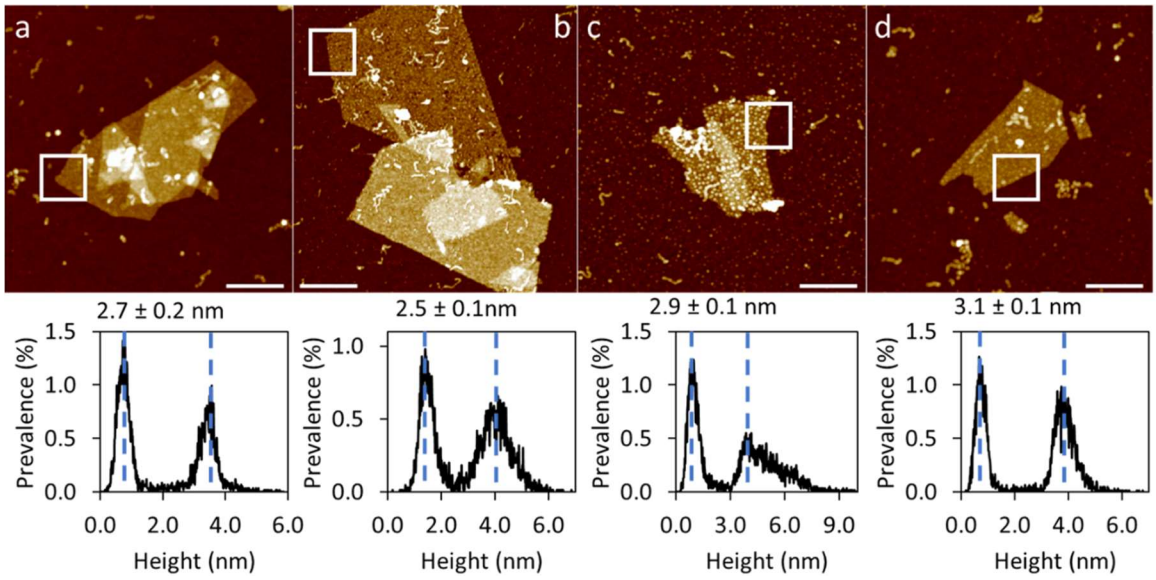

Figure 6.5 AFM topography images (top) taken with an ultrasharp tip and corresponding height histograms (bottom) of MXene flakes with suckerin deposited after soaking in 100 mM sodium sulfate (a) sodium citrate (b), sodium phosphate (c), and sodium acetate (d) for 16 hours. Scale bars are 400 nm, squares are 300 nm X 300 nm, and Z scales are 12 nm.

6.3.4 Morphology of Suckerin-12 Modified MXene Flakes

Next, we conducted AFM measurements of suckerin-12-co-assembled MXene flakes deposited via drop and spin casting. Modified flakes1.5 deposited via drop casting show an average thickness of 4.04 ± 0.01 nm and roughness of 0.27 ± 0.02 while flakes deposited via spin casting show a thickness and roughness of 4.62 ± 0.01 and 0.27 ± 0.01

nm. Assuming average pristine MXene thickness of 1.6 ± 0.01 nm, the suckerin-12 creates a shell with an effective thickness of 1.2 nm and 1.5 nm for drop and spin cast flakes, respectively. The higher thickness and roughness afforded to the spin cast flakes may be correlated to the shear induced self-assembly of the suckerin-12.

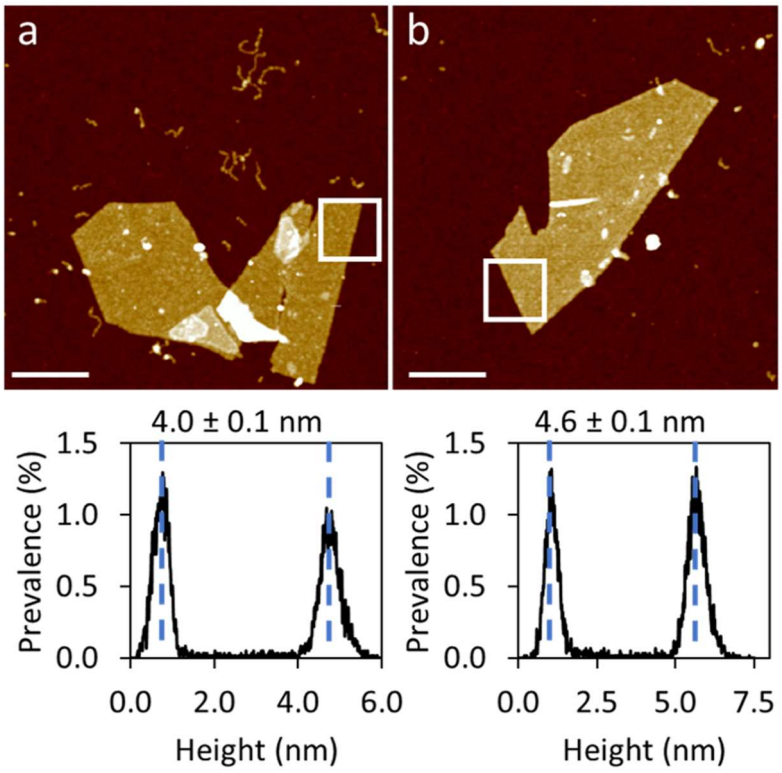

Figure 6.6 AFM topography images (top) taken with an ultrasharp tip and corresponding height histograms (bottom) of drop (a) and spin (b) cast MXene flakes directly modified with suckerin-12 in solution. Scale bars are 400 nm, squares are 300 nm X 300 nm, and Z scales are 12 nm.

The spin cast suckerin-12-modified MXene flakes were similarly treated with 100 mM salt solutions for 16 hours and imaged with HRAFM to determine changes in morphology. Flakes treated with acetate, sulfate, and citrate (in order of lowest to highest) had reduced thicknesses around 4 nm while those treated with phosphate were thicker at

about 4.9 nm. Treatment with sodium citrate induces the most inhomogeneity in the coating with some parts of the flake having larger globules than others.

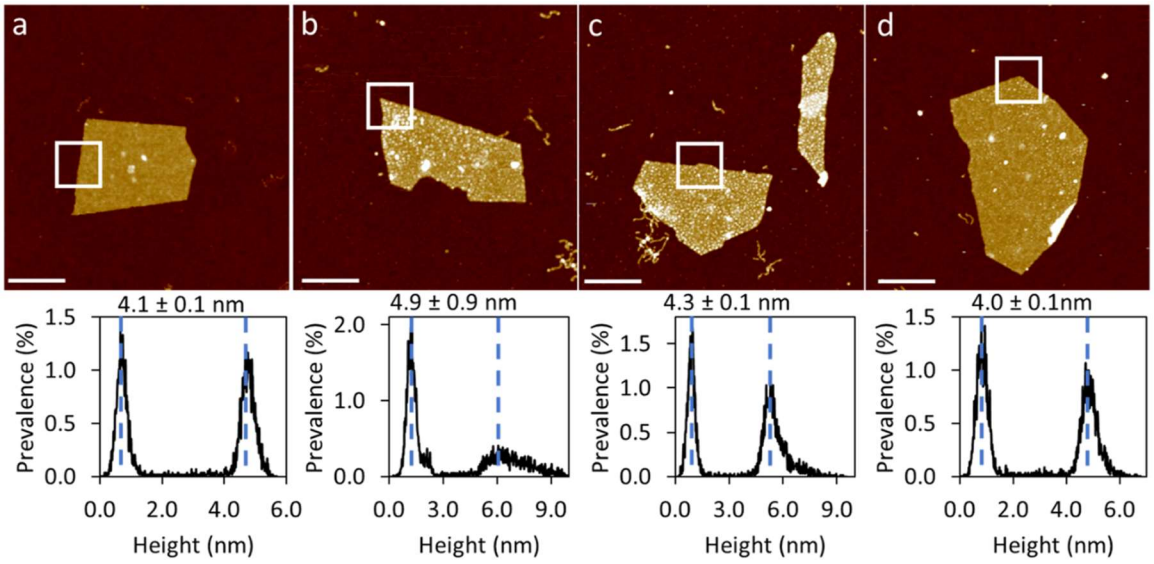

Figure 6.7 AFM topography images (top) taken with an ultrasharp tip and corresponding height histograms (bottom) of MXene flakes directly modified with suckerin-12 in solution deposited via spin casting after soaking in 100 mM sodium sulfate (a) sodium citrate (b), sodium phosphate (c), and sodium acetate (d) for 16 hours. Scale bars are 400 nm, squares are 300 nm X 300 nm, and Z scales are 12 nm.

6.4 Conclusion

We have shown that suckerin assembly takes place with spin casting induced shearing and kosmotropic salt annealing rendering the protein more stable in aqueous environments. Our results suggest that suckerin-12 may have a multi-step self-assembly process in which spin casting lends higher stability to thicker films allowing their further treatment in aqueous salt solutions. For thinner films adhered to silicon substrates and

MXene flakes, the shear induced assembly may hinder homogenous secondary structural change in response to salt solutions.

When spin cast rather than drop cast from higher concentration solutions, suckerin-12 assembled into a fibrous connected network via β-sheet formation.[30] We then characterized the self-assembly suckerin-12 when treated with salts of differing anions. The treatments proved to increase β-sheets formation from random coils and increased film stability. Self-assembly via salt annealing is reasonable considering the high salinity of the natural environment in which the squid live and similar to reports on other species. For example, it was found that the *Nereis virens* sandworm can plasticize and toughen its body via alternating anion infusion.[14] Thus, it is reasonable to assume that aqueous salt annealing is a stabilization methods used in nature.

We then showed that bioencapsulation of 2D $Ti_3C_2T_x$ MXene flakes with novel suckerin-12 protein provides flakes with a uniform coating. The suckerin-12 on the MXene surface showed similar morphological changes in response to salt annealing as those seen on silicon. However, in this case, the suckerin-12-MXene flakes deposited via spin casting developed less homogenous changes in response to salts due to the constrictions provided by the MXene surface and shear assembly of the protein. It is likely that being tethered to the MXene surface while having shear induced organization reduces mobility of the protein and causes heterogeneous annealing in salt solutions. These results indicate that the suckerin-12 morphology can be manipulated via exposure to salts and shearing to fabricate bulk films with tunable mechanical properties similar to our previously studied system of silk and MXene.

6.5 References

(1) Demirel, M. C.; Cetinkaya, M.; Pena-Francesch, A.; Jung, H. Recent Advances in Nanoscale Bioinspired Materials. *Macromolecular Bioscience* **2015**, *15* (3), 300–311. https://doi.org/10.1002/mabi.201400324.

(2) Miserez, A.; Weaver, J. C.; Pedersen, P. B.; Schneeberk, T.; Hanlon, R. T.; Kisailus, D.; Birkedal, H. Microstructural and Biochemical Characterization of the Nanoporous Sucker Rings from Dosidicus Gigas. *Advanced Materials* **2009**, *21* (4), 401–406. https://doi.org/10.1002/adma.200801197.

(3) Broomell, C. C.; Khan, R. K.; Moses, D. N.; Miserez, A.; Pontin, M. G.; Stucky, G. D.; Zok, F. W.; Waite, J. H. Mineral Minimization in Nature's Alternative Teeth. *Journal of the Royal Society Interface* **2007**, *4* (12), 19–31. https://doi.org/10.1098/rsif.2006.0153.

(4) Guerette, P. A.; Hoon, S.; Seow, Y.; Raida, M.; Masic, A.; Wong, F. T.; Ho, V. H. B.; Kong, K. W.; Demirel, M. C.; Pena-Francesch, A.; Amini, S.; Tay, G. Z.; Ding, D.; Miserez, A. Accelerating the Design of Biomimetic Materials by Integrating RNA-Seq with Proteomics and Materials Science. *Nature Biotechnology* **2013**, *31* (10), 908–915. https://doi.org/10.1038/nbt.2671.

(5) Guerette, P. A.; Hoon, S.; Ding, D.; Amini, S.; Masic, A.; Ravi, V.; Venkatesh, B.; Weaver, J. C.; Miserez, A. Nanoconfined β-Sheets Mechanically Reinforce the Supra-Biomolecular Network of Robust Squid Sucker Ring Teeth. *ACS Nano* **2014**, *8* (7), 7170–7179. https://doi.org/10.1021/nn502149u.

(6) Buck, C. C.; Dennis, P. B.; Gupta, M. K.; Grant, M. T.; Crosby, M. G.; Slocik, J. M.; Mirau, P. A.; Becknell, K. A.; Comfort, K. K.; Naik, R. R. Anion-Mediated Effects on the Size and Mechanical Properties of Enzymatically Crosslinked Suckerin Hydrogels. *Macromolecular Bioscience* **2019**, *19* (3). https://doi.org/10.1002/mabi.201800238.

(7) Chen, J.; Chan, Y.-H.; Yang, T.; Wark, S. E.; Son, D. H.; Batteas, J. D. Spatially Selective Optical Tuning of Quantum Dot Thin Film Luminescence. *J. Am. Chem. Soc.* **2009**, *131* (51), 18204–18205. https://doi.org/10.1021/ja906837s.

(8) Yin, Y.; Hu, K.; Grant, A. M.; Zhang, Y.; Tsukruk, V. V. Biopolymeric Nanocomposites with Enhanced Interphases. *Langmuir* **2015**, *31* (39), 10859–10870. https://doi.org/10.1021/acs.langmuir.5b02744.

(9) Hu, X.; Kaplan, D.; Cebe, P. Determining Beta-Sheet Crystallinity in Fibrous Proteins by Thermal Analysis and Infrared Spectroscopy. *Macromolecules* **2006**, *39* (18), 6161–6170. https://doi.org/10.1021/ma0610109.

(10) Hiew, S. H.; Miserez, A. Squid Sucker Ring Teeth: Multiscale Structure-Property Relationships, Sequencing, and Protein Engineering of a Thermoplastic Biopolymer. *ACS Biomaterials Science and Engineering* **2017**, *3* (5), 680–693. https://doi.org/10.1021/acsbiomaterials.6b00284.

(11) Grant, A. M.; Kim, H. S.; Dupnock, T. L.; Hu, K.; Yingling, Y. G.; Tsukruk, V. V. Silk Fibroin–Substrate Interactions at Heterogeneous Nanocomposite Interfaces. *Advanced Functional Materials* **2016**, *26* (35), 6380–6392. https://doi.org/10.1002/adfm.201601268.

(12) Okur, H. I.; Hladílková, J.; Rembert, K. B.; Cho, Y.; Heyda, J.; Dzubiella, J.; Cremer, P. S.; Jungwirth, P. Beyond the Hofmeister Series: Ion-Specific Effects on Proteins and Their Biological Functions. *Journal of Physical Chemistry B* **2017**, *121* (9), 1997–2014. https://doi.org/10.1021/acs.jpcb.6b10797.

(13) Ding, D.; Guerette, P. A.; Fu, J.; Zhang, L.; Irvine, S. A.; Miserez, A. From Soft Self-Healing Gels to Stiff Films in Suckerin-Based Materials Through Modulation of Crosslink Density and β-Sheet Content. *Advanced Materials* **2015**, *27* (26), 3953–3961. https://doi.org/10.1002/adma.201500280.

(14) Oglesby, L. C.; Mangum, C. P.; Heacox, A. E.; Ready, N. E. Salt and Water Balance in the Polychaete Nereis Virens. *Comparative Biochemistry and Physiology -- Part A: Physiology* **1982**, *73* (1), 15–19. https://doi.org/10.1016/0300-9629(82)90085-8.

CHAPTER 7. GENERAL CONCLUSIONS AND BROADER IMPACT

7.1 General Conclusions

This work advances the understanding of how several critical functional biopolymers interact in intimate contact with synthetic 2D MXenes providing an avenue for creating functional bionanocomposites with tunable mechanical and conductive properties. While recent research has shown that the combination of biopolymers and synthetic 2D flakes allows for composites with unique functionalities, there is still a gap between the interfacial processes and overall performance that limits the field of bionanocomposites.

The goal of this study was to help bridge this gap by investigating 2D synthetic flakes in intimate contact with proteins and consider the fundamental mechanisms of organization and leverage them to fabricate ordered, mechanically strong, chemically stable, and functional bionanocomposites. This was achieved through investigating the structural changes of well-studied silk fibroin and novel suckerin-12 proteins while tethered to $Ti_3C_2T_x$ MXene and the resultant conductive and mechanical performance of films made from silk-encapsulated MXene.

First, we co-assembled $Ti_3C_2T_x$ MXene flakes with recombinant silk fibroin in aqueous suspensions resulting in silk fibroin nanolayers uniformly covering individual flakes. These bioencapsulated flakes evolved with time due to the gradual growth of silk bundles having β-sheet secondary organization with unique nanofibrillar morphologies extending across flake edges and forming long fringes around individual MXene flakes. Colloidal dispersions of these MXene-silk hybrid flakes can be used to deposit single flakes

for fundamental characterization or device fabrication onto silicon and other substrates, as well as to manufacture composite films for a variety of applications. The silk coating provides increased stability in suspension allowing for longer storage and ease of processing while preventing restacking of MXene flakes. Due to the nature of the modification, this hybrid may provide strong and flexible membranes for various applications.

It is important to emphasize that silk fibroin can efficiently encapsulate MXene flakes with either uniform shells or hairy coatings, depending on specific interfacial processes. After attachment, silk can reorganize from amorphous globules into nanofibrillar bundles and β-sheets inhibiting surface oxidation and stabilizing MXenes in colloidal solutions and aqueous media in general. This spontaneous reorganization of recombinant silk suggests surface template-initiated formation of intramolecular hydrogen bonding of silk backbones assisted by intermolecular electrostatic and hydrogen bonding with the MXene flake. The formation of dense and hydrophobic β-sheets results in development of a protective shell that hinders the surface oxidation of $Ti_3C_2T_x$ in colloidal solution in water and significantly extends the storage life of the individual MXene flakes.

Despite having a high silk composition of nearly 70 wt %, the multilayered composites made from the silk-encapsulated MXene were still electrically conductive. However, the SFMX composites displayed a conductivity 2-3 orders of magnitude less than that of MXene only films. This is due to the 2-4 nm dielectric gap created between flakes compromising the low percolation limit of 2D laminated materials caused by the tight encapsulation of the individual MXene flakes. Despite this reduction in conductivity, the values measured for the SFMX composites are still comparable to those reported for

partially reduced 2D graphene oxide materials widely used for various electronic-related applications.[45,46] Moreover, assembly into organized laminated composites with individual bioencapsulated flakes tightly interconnected via biopolymer bundles and hairs produces robust freestanding electrically conductive membranes with enhanced transport properties.

Second, we used this system to investigate the mechanical properties of multilayered bionanocomposites with different silk secondary structures and concentrations. Amorphous silk encapsulated MXene showed enhanced modulus and ultimate stress due to the silk acting as glue for the brick like 2D flakes. MXene encapsulated with fibrillar silk showed an increase in modulus (less than that of amorphous silk encapsulated MXene) from the MXene only system but a decrease in ultimate strength and strain. Buckling mechanical tests of individual hybrid flakes revealed similar results but showed fibrillar silk modified MXene to be incompressible on the small length scale. Bionanocomposites made by simply mixing silk and MXene at different ratios reveal that smaller amounts of silk, about 5%, provide better reinforcement than larger amounts similar to systems of silk and graphene oxide. It is important to note that these silk MXene multilayered systems have shown enhanced mechanical performance without significant loss of electrical conductivity.

Last, we used our knowledge of silk and our previous systems to investigate the molecular self-assembly of the suckerin-12 protein derived from the sucker ring teeth of the Humboldt squid. The protein itself behaves similarly to silk in response to shear induced assembly with enhanced β-sheet formation. The protein was exposed to different salt solutions to draw parallels with previous studies on hydrogels of the same protein. Our findings indicate that thin films of the same protein react similarly by having increased β-

sheet formation when exposed to more kosmotropic salts like sodium phosphate, sulfate, and citrate.

Using experience from the previous silk and MXene studies, suckerin-12 was mixed with MXene to form suckerin encapsulated MXene flakes. The results provide more insight into the similarities and differences of the two proteins. Like silk, the suckerin was able to attach to MXene in aqueous solution but it had a slightly different morphology displaying a thinner protein layer with a distinct lack of corona likely attributed to the smaller molecular weight. With exposure to kosmotropic salt solutions, the suckerin-12 reorganized into organized secondary structures with both drop and spin cast films reacting similarly to the different salts. However, spin cast suckerin-12-encapsulated flakes displayed more heterogenous structure reformation than those drop cast. This may be due to the inhomogeneities in MXene surface functionalities nucleating organization in some spots while order induced via shear blocks portions of the protein from aqueous annealing. This study shows that MXene can be encapsulated suckerin-12 protein and the secondary structure can be manipulated using different deposition methods and salt annealing proving there is an ability for these hybrid materials to serve as tunable composite precursors.

7.2 Significance and Broader Impact

The field of organized bionanocomposites has yielded many systems with enhanced capabilities from optically active and conductive films to biocompatible and sensing materials through inspiration and derivation from natural systems. These systems depend on the intimate organization of conductive and mechanically strong fillers and biocompatible and stimuli responsive biological materials.

Due to the inherent complexity of the natural components, much investigation into their fundamental processes of organization and structure is necessary for proper management of the bulk properties of composites made from them. As outlined in this dissertation we have demonstrated that proteins such as silk and suckerin-12 can serve as biological binders for $Ti_3C_2T_x$ MXene flakes resulting in electrically conductive multilayered composites with enhanced mechanical stability. We have also shown that MXene can serve as a template for guiding the self-assembly of proteins thus providing a model with which the nanoscale morphological changes of other proteins be investigated before forming hybrid organized composites.

While these works have provided fundamental knowledge these protein-based nanocomposite systems, there is still much work that can be done. It would be beneficial to directly investigate the resultant mechanical properties of the suckerin-12 MXene hybrid constructs to provide insight for the similarities and differences afforded by materials of such different sizes. These systems could also be used to fabricate devices such as strain sensors, electromagnetic interference shielding films, and separation membranes for which understanding into the long-term stability and degradability of these composites is imperative for ensuring continued performance in flexible functional materials. Overall, the field of protein nanocomposites is promising for the development of biocompatible functional materials for various applications such as flexible electronics, wearable sensors, energy storage, and selective molecular transport.

7.3 Acknowledgements

This material is based upon work supported by Air Force Office for Scientific Research FA9550- 17-1-0297 and FA8650-D-16-5404 awards and the National Science Foundation Graduate Research Fellowship under Grant No. DGE-1650044 and Grant No. DGE-1148903 to Anise Grant. MXene research at Drexel University was supported by the National Science Foundation under Grant DMR-1740795. Suckerin-12 protein was provided by the Air Force Research Laboratory. This work was performed in part at the Georgia Tech Institute for Electronics and Nanotechnology, a member of the National Nanotechnology Coordinated Infrastructure (NNCI), which is supported by the National Science Foundation (ECCS-2025462)

7.4 Dissemination of Work

This work has been disseminated to the scientific community through the following publications and presentations.

Primary Publications:

[1] **Krecker, M. C**.; Bukharina, D.; Gogotsi, Y.; Tsukruk, V. V. Mechanically Tunable MXene and Silk Bionanocomposites. *In Preparation.*

[2] Wang, Z.; Kang, S.; Cao, S.; **Krecker, M**.; Tsukruk, V. V.; Singamaneni, S. Protein-Based Functional Nanocomposites. *MRS Bulletin* **2020**, 45 (12), 1017–1026. *Cover story

[3] Grant, A. M.*; **Krecker, M. C**.*; Gupta, M. K.; Dennis, P. B.; Crosby, M. G.; Tsukruk, V. V. Marine Structural Protein Stability Induced by Hofmeister Salt Annealing and Enzymatic Cross-Linking. *ACS Biomaterials Science and Engineering* **2020**, 6 (10), 5519–5526. *Co-first authors

[4] **Krecker, M. C**.; Bukharina, D.; Hatter, C. B.; Gogotsi, Y.; Tsukruk, V. V. Bioencapsulated MXene Flakes for Enhanced Stability and Composite Precursors. *Advanced Functional Materials* **2020**, 30 (43), 2004554.

Other Publications:

[5] Xiong, R.; Zhang, X.; **Krecker, M**.; Kang, S.; Smith, M. J.; Tsukruk, V. V. Large and Emissive Crystals from Carbon Quantum Dots onto Interfacial Organized Templates. *Angewandte Chemie - International Edition* **2020**, 59 (45), 20167–20173.

[6] Wei, W.; Faubel, J. L.; Selvakumar, H.; Kovari, D. T.; Tsao, J.; Rivas, F.; Mohabir, A. T.; **Krecker, M**.; Rahbar, E.; Hall, A. R.; Filler, M. A.; Washburn, J. L.; Weigel, P. H.; Curtis, J. E. Self-Regenerating Giant Hyaluronan Polymer Brushes. *Nature Communications* **2019**, 10 (1), 5527.

[7] Xiong, R.; Yu, S.; Smith, M. J.; Zhou, J.; **Krecker, M**.; Zhang, L.; Nepal, D.; Bunning, T. J.; Tsukruk, V. V. Self-Assembly of Emissive Nanocellulose/Quantum Dot Nanostructures for Chiral Fluorescent Materials. *ACS Nano* **2019**, 13 (8), 9074–9081.

Presentations:

[1] **Krecker, M**.; Bukharina, D.; Hatter, C. B.; Gogotsi, Y.; Tsukruk, V. V. Self-Assembly of Recombinant Silk Fibroin on $Ti_3C_2T_x$ MXene Surface, Oral presentation at the 2020 Virtual MRS Spring/Fall Meeting & Exhibit, December 2020.

[2] **Krecker, M**.; Grant, A.; Savchak, M.; Borodinov, N.; Luzinov, L.; Tsukruk, V. V. Assembly of grafted polymers on modified graphene oxide, Oral presentation at the 255th American Chemical Society National Meeting & Exposition, New Orleans, LA, March 2018.

[3] Grant, A.; **Krecker, M**.; Tadepalli, S.; Gupta, M.; Crosby, M.; Dennis, P.; Singamaneni, S.; Naik, R.; Tsukruk, R. Aqueous Toughening in Crosslinked Marine Animal Proteins, Oral presentation at the 255th American Chemical Society National Meeting & Exposition, New Orleans, LA, March 2018.

APPENDIX A. CHAPTER 4 SUPPORTING INFORMATION

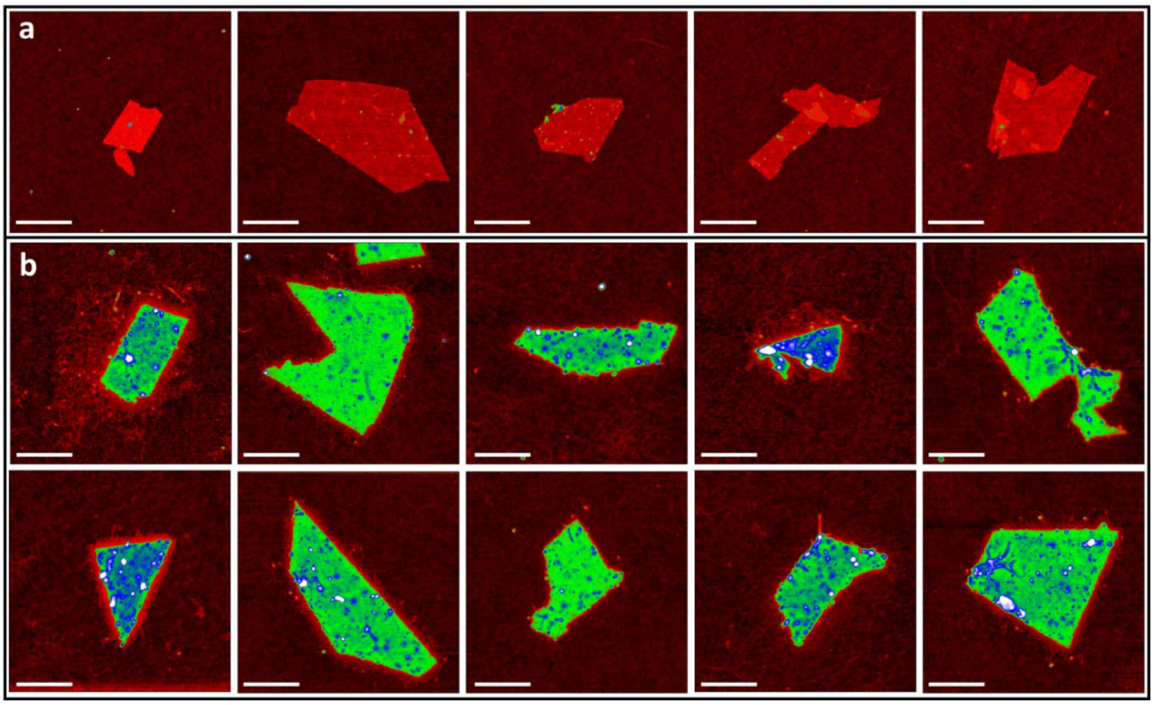

Figure A.1 AFM topography images of pristine MXene (a) and SFMX on day 1 (b) with 16 nm Z-scale and 500 nm scale bars.

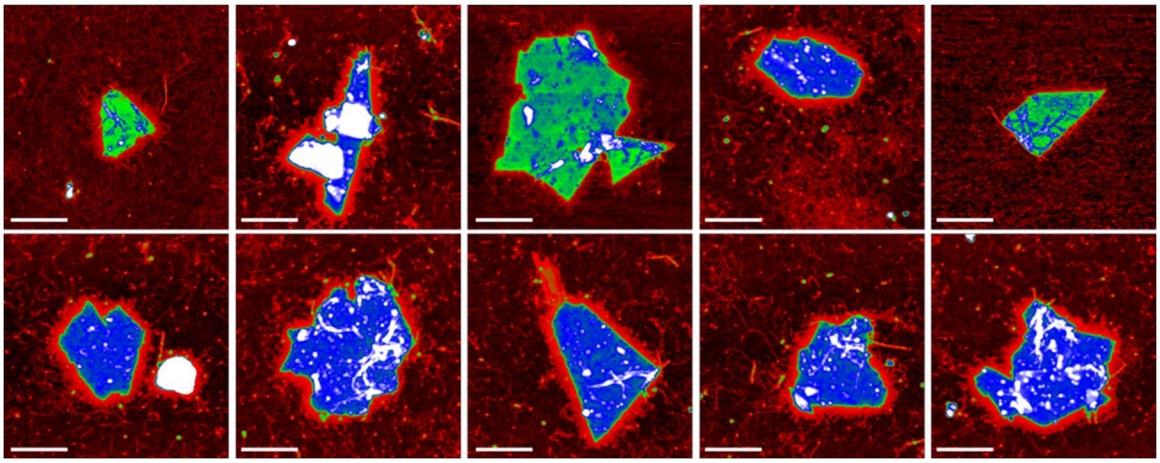

Figure A.2 AFM topography images of SFMX on day 3 with 16 nm Z-scale and 500 nm scale bars.

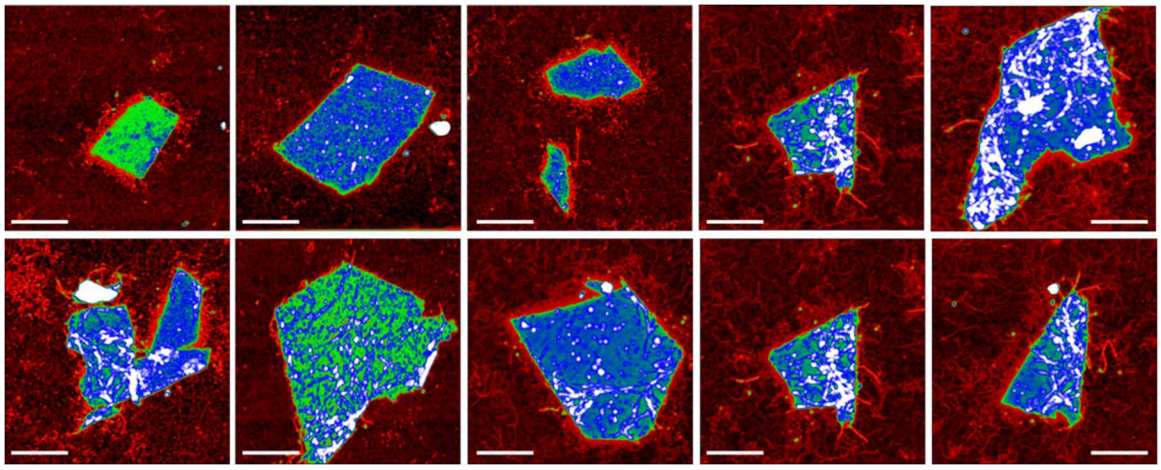

Figure A.3 AFM topography images of SFMX on day 5 with 16 nm Z-scale and 500 nm scale bars.

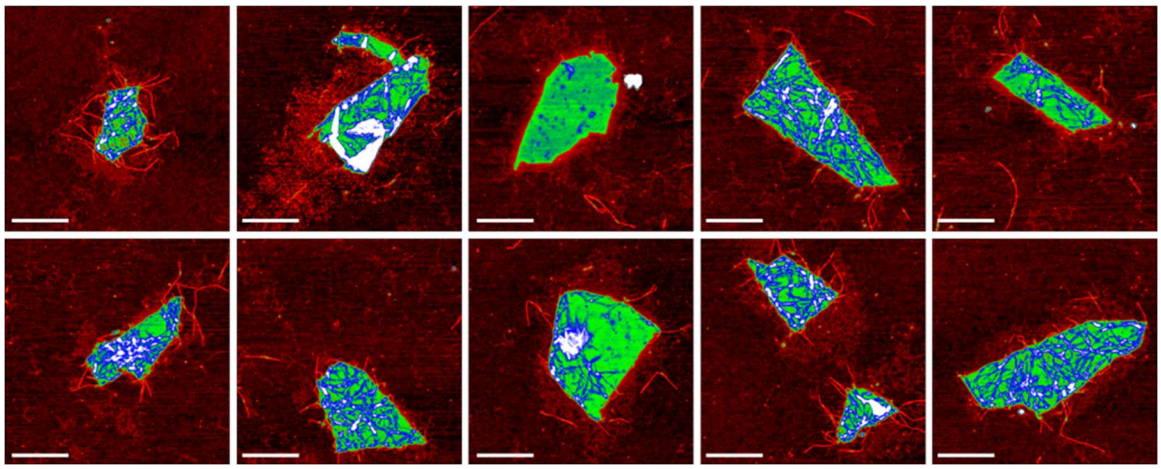

Figure A.4 AFM topography images of SFMX on day 7 with 16 nm Z-scale and 500 nm scale bars.

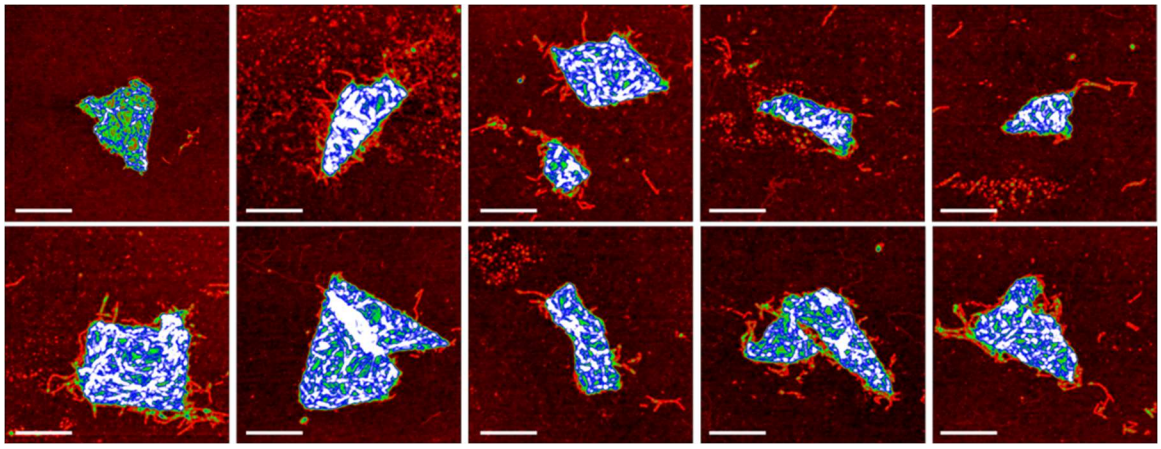

Figure A.5 AFM topography images of SFMX on day 19 with 16 nm Z-scale and 500 nm scale bars.

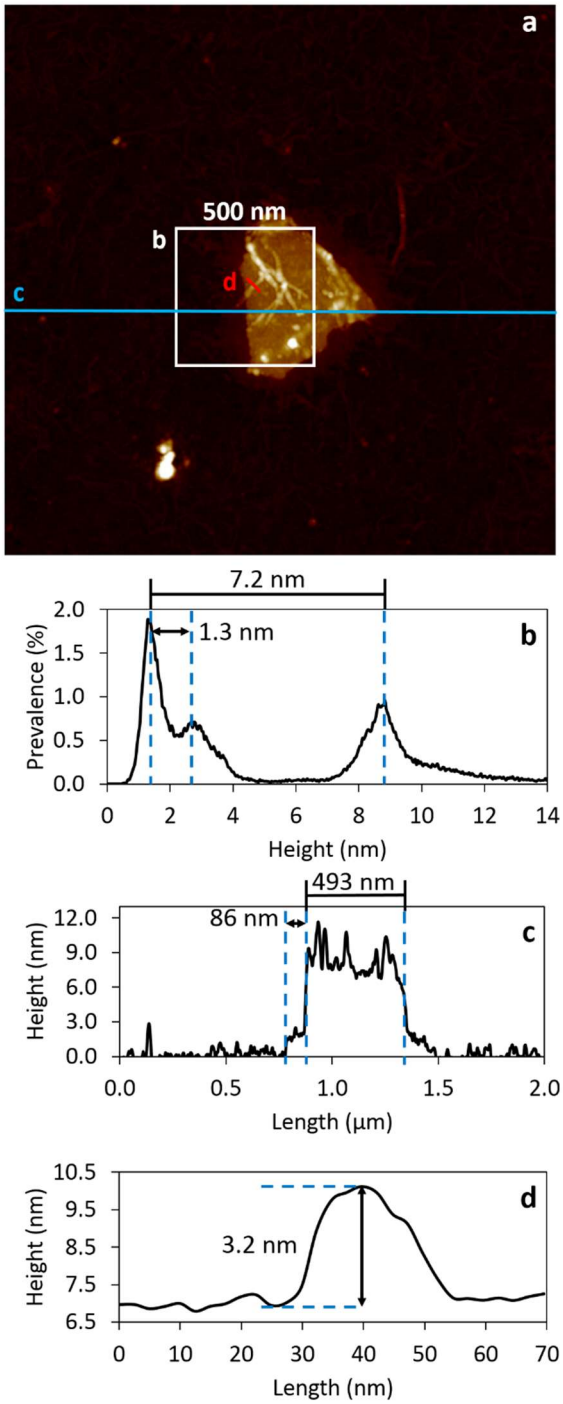

Figure A.6 A topographical AFM image of a day three SFMX flake (a) with corresponding height histogram showing flake and corona height (b), flake height profile showing size of corona (c), and profile showing a fibril height (d).

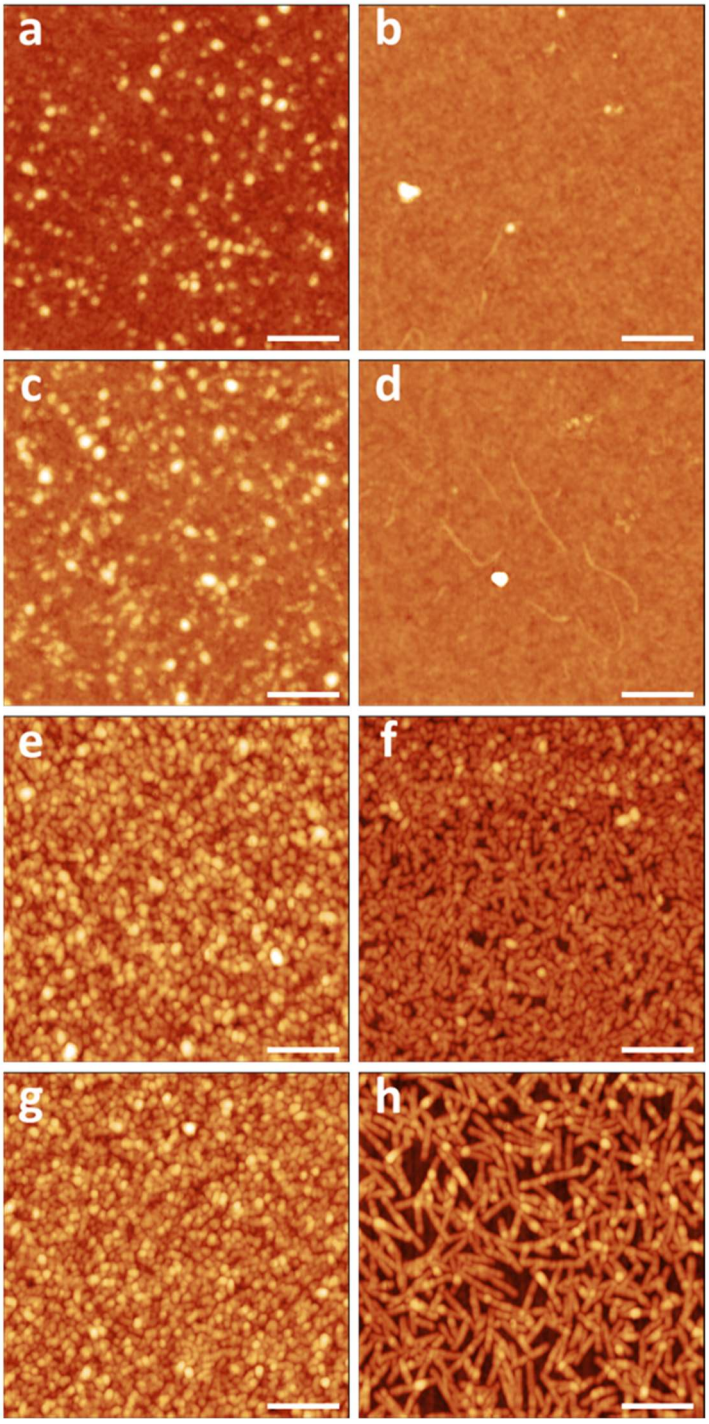

Figure A.7 AFM images of silk spin (a, c, e, g) and dip (b, d, f, h) cast from 0.1 wt% silk solution that was kept at 4 °C for 105 days (a, b) and six days (c, d, e, f, g, h). The images include silk films allowed to sit in water at 4 °C (e, f) and 50 °C (g, h) for three days. Z scale is 10 nm and scale bars are 200 nm.

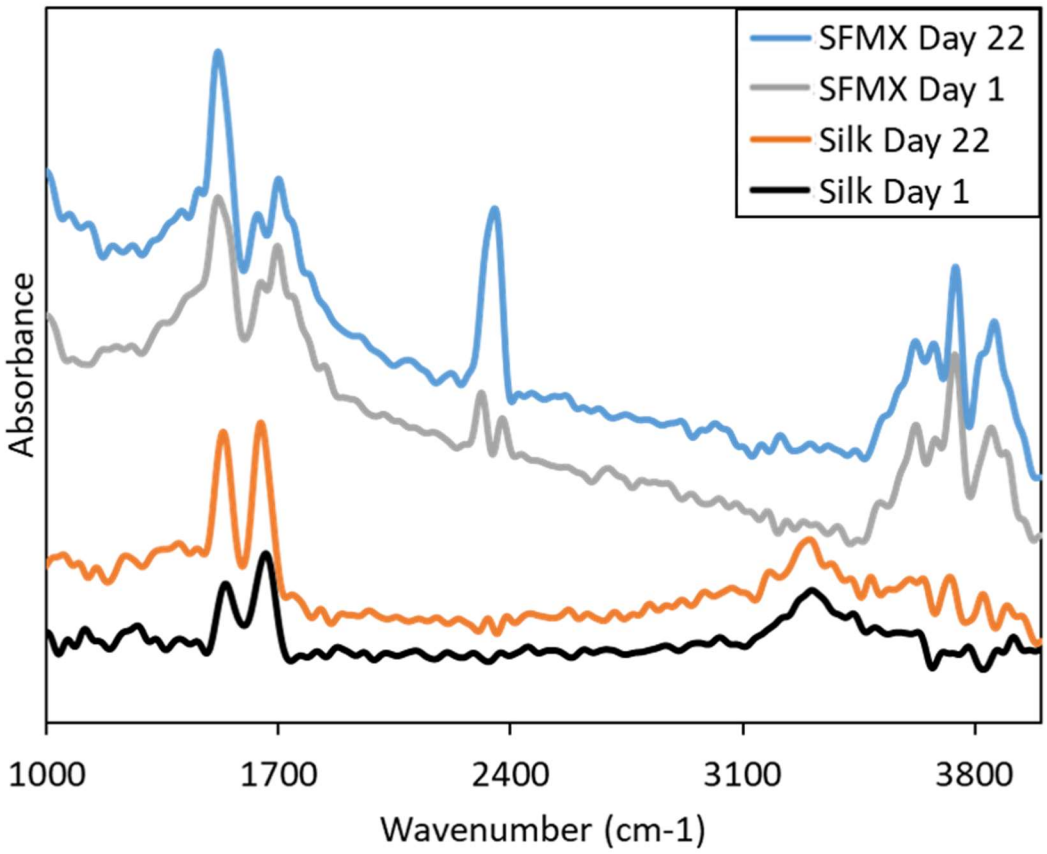

Figure A.8 ATR-FTIR spectra of silk and SFMX from fresh solutions and those kept at 4 °C for 22 days.

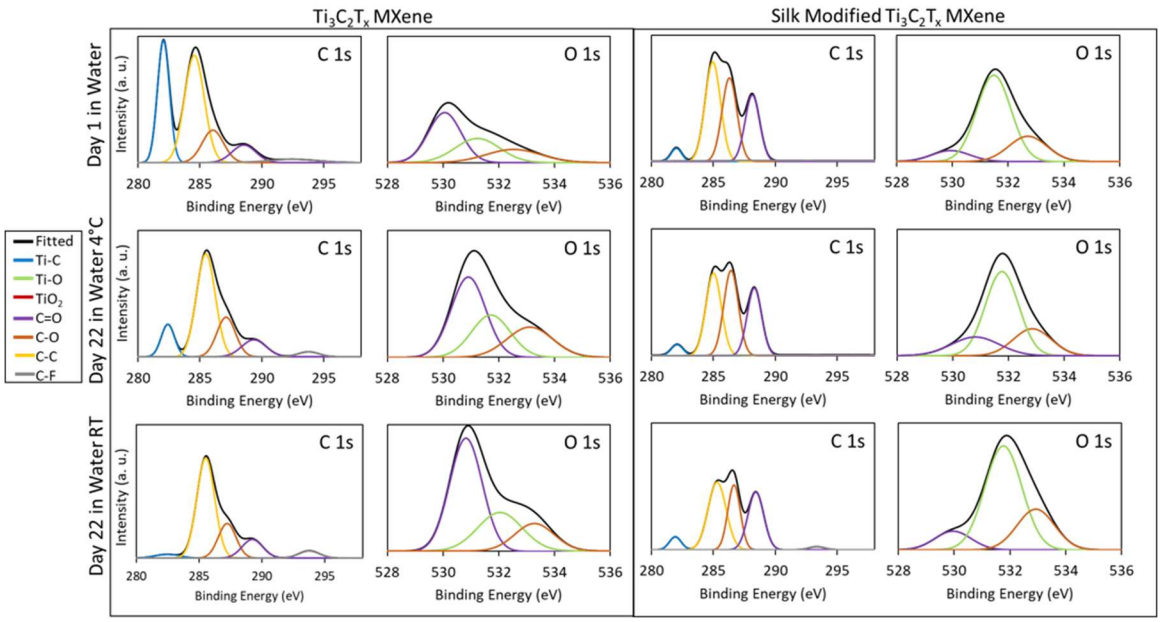

Figure A.9 XPS spectra of pristine MXene and SFMX after being stored in water at 4°C and room temperature over a period of 22 days.

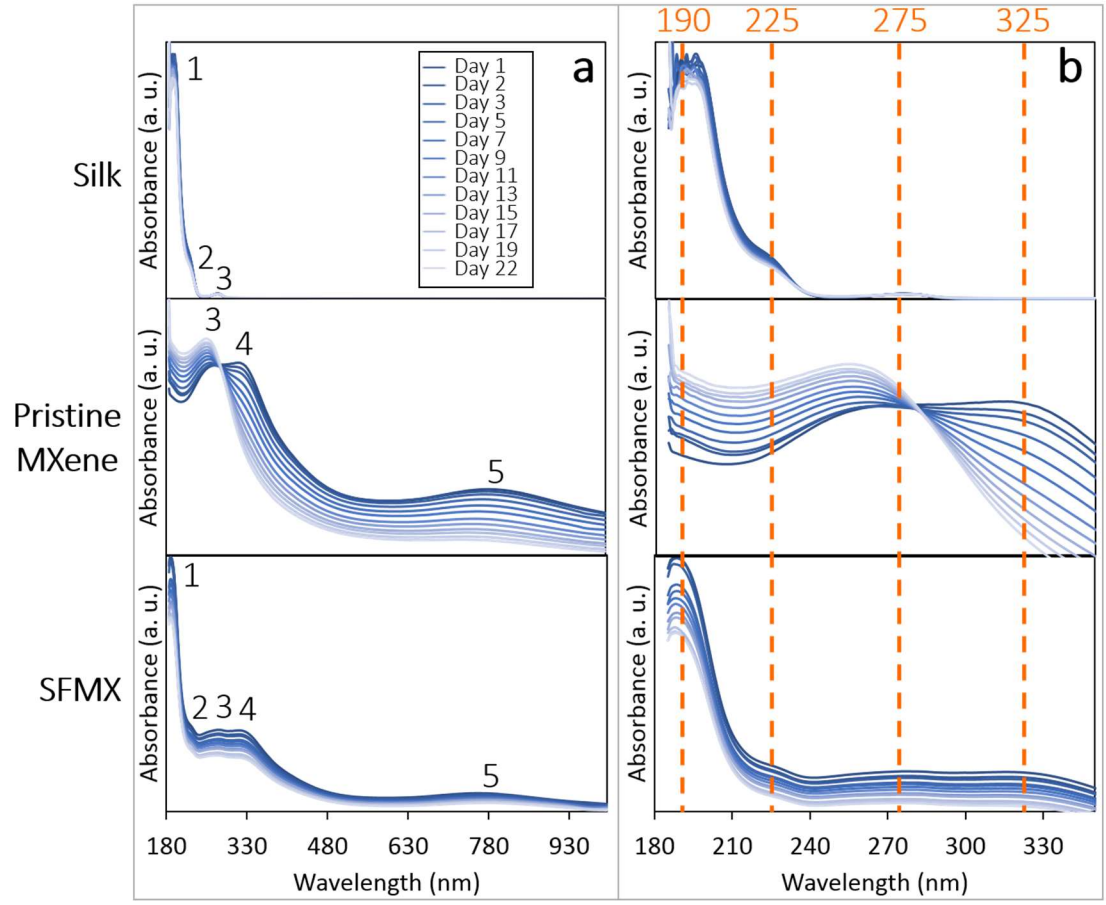

Figure A.10 UV-Vis spectra of pristine silk, MXene, and SFMX solutions at 0.01 wt% from (a) 180-1000 nm and from (b) 180-350 nm to show the peak origins of the SFMX.

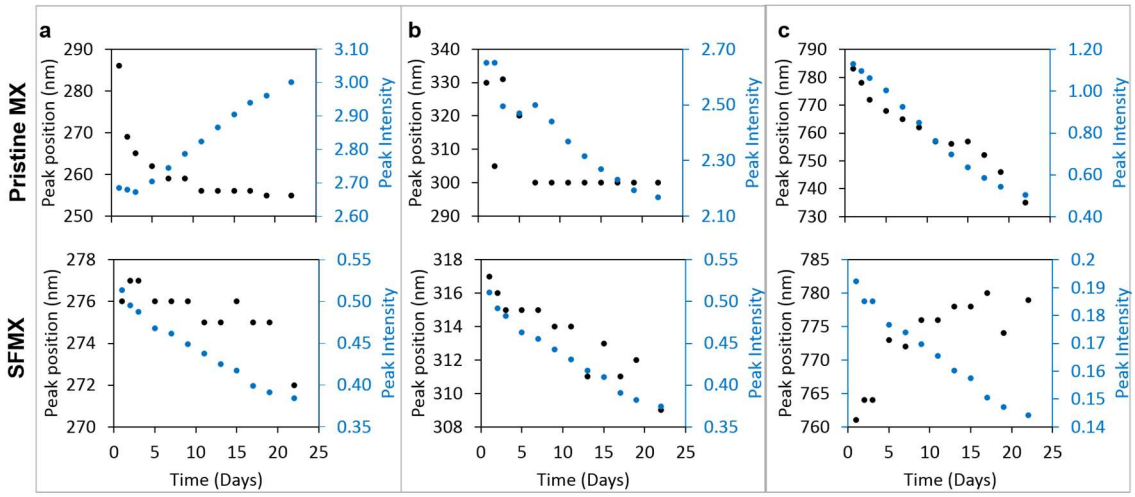

Figure A.11 Plots of UV-Vis peak position and absorbance intensity for peaks 3 (a), 4 (b), and 5 (c) as designated in Figure A.10.

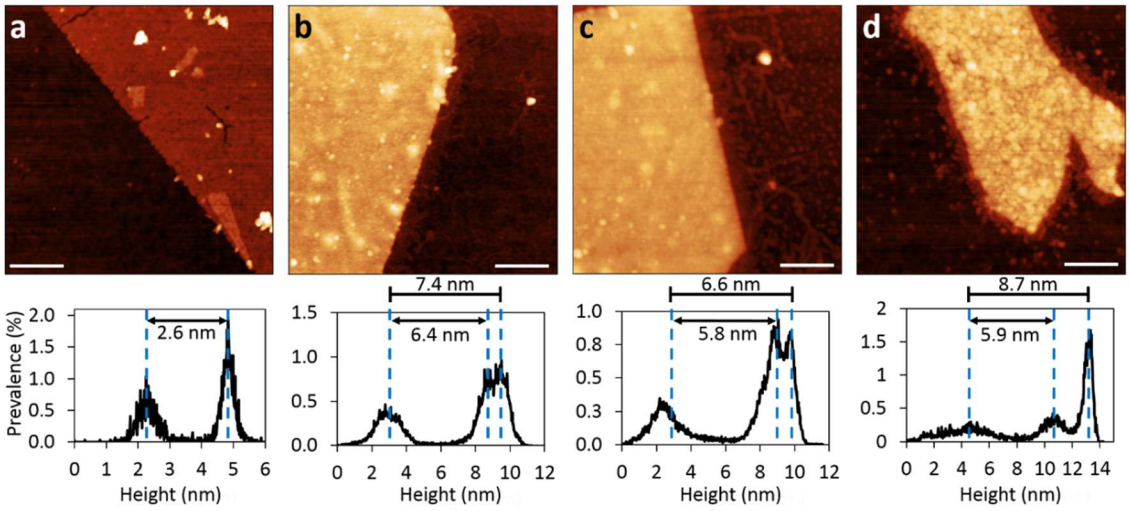

Figure A.12 AFM topography images and corresponding histograms of pristine MXene (a), SFMX (b), MeOH vapor treated SFMX (c), and MeOH solvent treated SFMX. Scale bars are 200 nm and Z scale is 30 nm.

To ensure the fibril formation takes place in solution and not due to spin casting, these flakes were deposited onto thermally oxidized silicon wafers via dip coating and either allowed to air dry or dry by air gun. As shown in Figure A.10, flakes deposited after

three weeks in solution show no visible difference in morphology due to different deposition (spin or dip cast) or drying techniques (evaporation and airflow). Flakes were also unperturbed by post deposition rinses in water proving these flakes are relatively stable and have a high affinity to the silica surface.

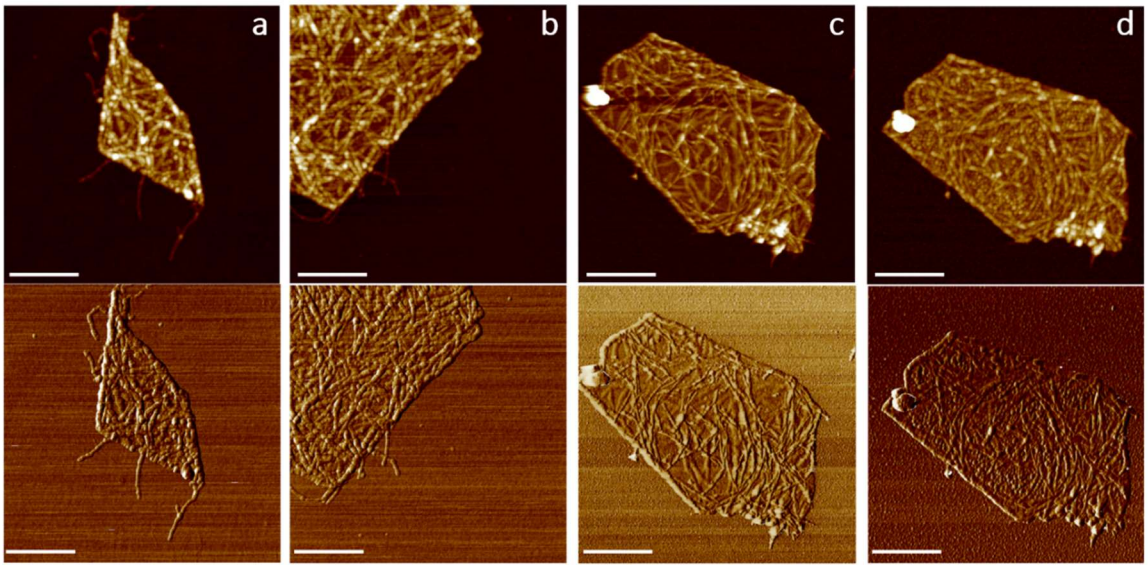

Figure A.13 AFM topographical (top) and corresponding phase (bottom) images (Z=25 nm, phase=10°, Scale bar=500 nm) of dip cast SFMX flakes (a) allowed to dry by evaporation and (b) dried with an air gun as well as one flake spun cast from water at 3000 rpm for 30 seconds (c) before and (d) after being rinsed with water via spin casting.

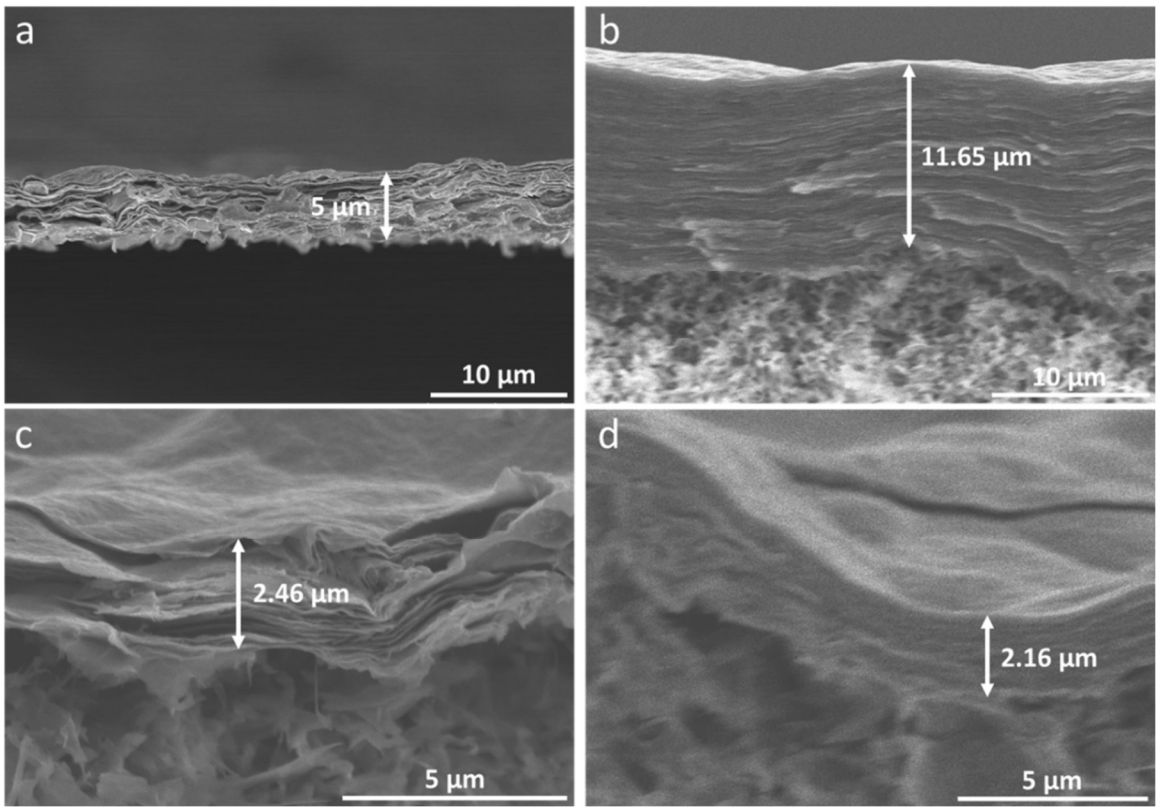

Figure A.14 SEM images showing the thickness of MX (a, c) and SFMX (b, d) vacuum filtered films.

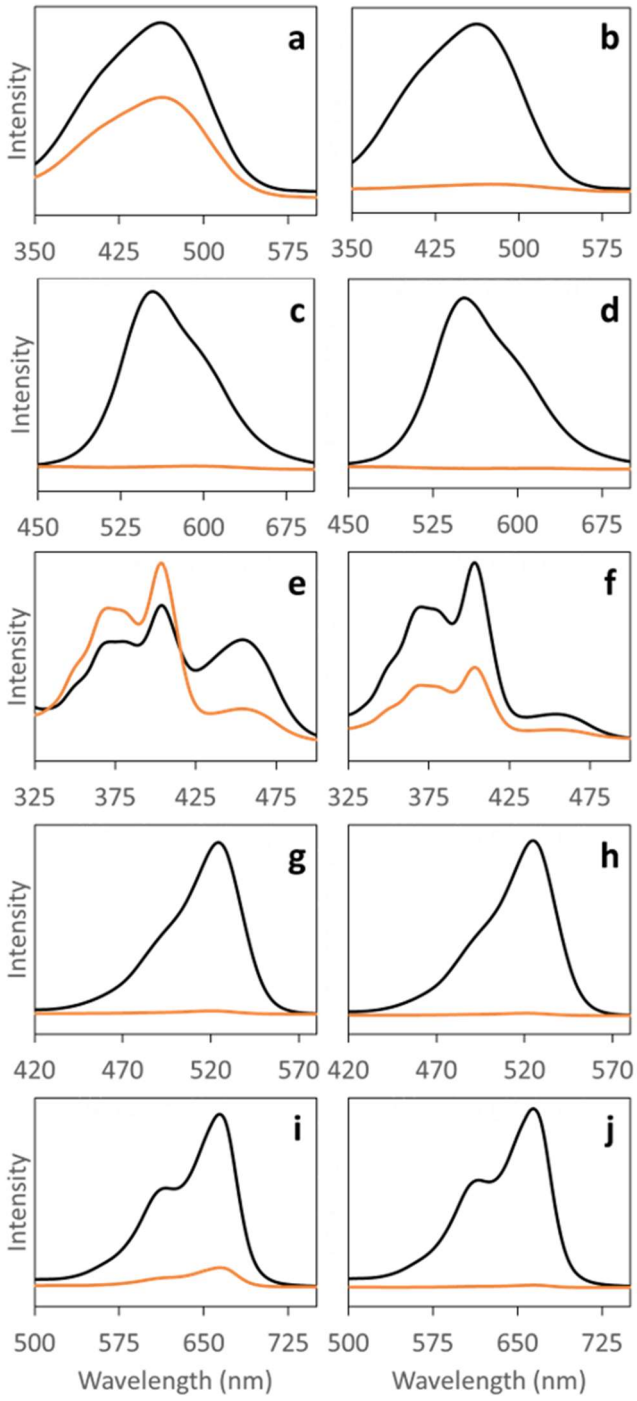

Figure A.15 UV-Vis spectra of PMR (a, b), BB (c, d), P (e, f), R6G (g, h), and MB (i, j) dye solutions before (black) and after (orange) filtering through MX (a, c, e, g, i) SFMX (b, d, f, h, j) films.

Table A.1 Table showing permeance and dye rejection performance of MX and SFMX vacuum assisted filtration films.

Dye	Size (nm)	Charge (mV)	Sample	Permeance ($Lm^{-2}bar^{-1}h^{-1}$)	Rejection (%)
BB	2.8 x 1.8	-30.4 ± 0.8	MX	171.4	97.9
			SFMX	85.6	100.0
P	1.3 x 0.9	-23.4 ± 1.4	MX	458.4	11.5
			SFMX	125.9	60.3
PMR	1.9 x 0.7	-9.0 ± 1.0	MX	145.7	43.3
			SFMX	73.7	94.6
R6G	1.9 x 1.2	-0.8 ± 0.8	MX	553.2	98.0
			SFMX	94.7	98.8
MB	1.7 x 0.4	7.0 ± 1.0	MX	653.1	88.9
			SFMX	66.2	98.9

APPENDIX B. CHAPTER 6 SUPPORTING INFORMATION

Table B.1 Summary of processing conditions and RMS roughness measurements discussed in the main text for suckerin-12 films.

Imaging Method	S12 Deposition	Concentration (wt%)	Sodium Salt	Annealing Time (hr)	RMS Roughness (nm)
AFM	DC	1	N/A	N/A	0.4 ± 0.08
AFM	SC	1	N/A	N/A	0.9 ± 0.5
AFM	SC	3	Sulfate	1	2.2 ± 0.4
AFM	SC	3	Citrate	1	3.2 ± 0.5
AFM	SC	3	Phosphate	1	3 ± 0.3
AFM	SC	3	Acetate	1	3.1 ± 0.3
AFM	DC/ rinse	0.1	Sulfate	1	0.34 ± 0.02
AFM	DC/ rinse	0.1	Sulfate	264	0.49 ± 0.02
AFM	DC/ rinse	0.1	Citrate	1	0.52 ± 0.02
AFM	DC/ rinse	0.1	Citrate	264	1.01 ± 0.03
HRAFM	DC/ rinse	0.1	N/A	N/A	0.353 ± 0.004
HRAFM	DC/ rinse	0.1	Sulfate	16	0.185 ± 0.017
HRAFM	DC/ rinse	0.1	Citrate	16	0.354 ± 0.012
HRAFM	DC/ rinse	0.1	Phosphate	16	0.524 ± 0.067
HRAFM	DC/ rinse	0.1	Acetate	16	0.233 ± 0.011

Table B.2 Summary of processing conditions and RMS roughness measurements for suckerin-12-MXene systems as discussed in the main text.

Imaging Method	S12 Deposition	Concentration (wt%)	Sodium Salt	Annealing Time (hr)	Flake Thickness (nm)	RMS Roughness (nm)
AFM	N/A	N/A	N/A	N/A	1.85 ± 0.01	0.28 ± 0.09
AFM	DC/ rinse	0.1	N/A	N/A	2.35 ± 0.01	0.69 ± 0.22
AFM	DC/ rinse	0.1	Sulfate	1	3.04 ± 0.01	0.47 ± 0.01
AFM	DC/ rinse	0.1	Sulfate	264	2.38 ± 0.01	0.48 ± 0.04
AFM	DC/ rinse	0.1	Citrate	1	2.99 ± 0.02	0.62 ± 0.03
AFM	DC/ rinse	0.1	Citrate	264	4.06 ± 0.02	0.52 ± 0.20
HRAFM	DC/ rinse	0.1	N/A	N/A	3.030 ± 0.009	0.355 ± 0.012
HRAFM	DC/ rinse	0.1	Sulfate	16	2.704 ± 0.006	0.257 ± 0.010
HRAFM	DC/ rinse	0.1	Citrate	16	2.567 ± 0.013	0.501 ± 0.081
HRAFM	DC/ rinse	0.1	Phosphate	16	2.904 ± 0.060	1.103 ± 0.041
HRAFM	DC/ rinse	0.1	Acetate	16	3.105 ± 0.007	0.367 ± 0.007
HRAFM	Suspension/ DC	0.24	N/A	N/A	4.039 ± 0.004	0.273 ± 0.023
HRAFM	Suspension/ SC	0.24	N/A	N/A	4.624 ± 0.005	0.274 ± 0.010
HRAFM	Suspension/ SC	0.24	Sulfate	16	4.069 ± 0.004	0.236 ± 0.033
HRAFM	Suspension/ SC	0.24	Citrate	16	4.904 ± 0.867	0.765 ± 0.264
HRAFM	Suspension/ SC	0.24	Phosphate	16	4.340 ± 0.01	0.736 ± 0.027
HRAFM	Suspension/ SC	0.24	Acetate	16	4.019 ± 0.006	0.378 ± 0.078

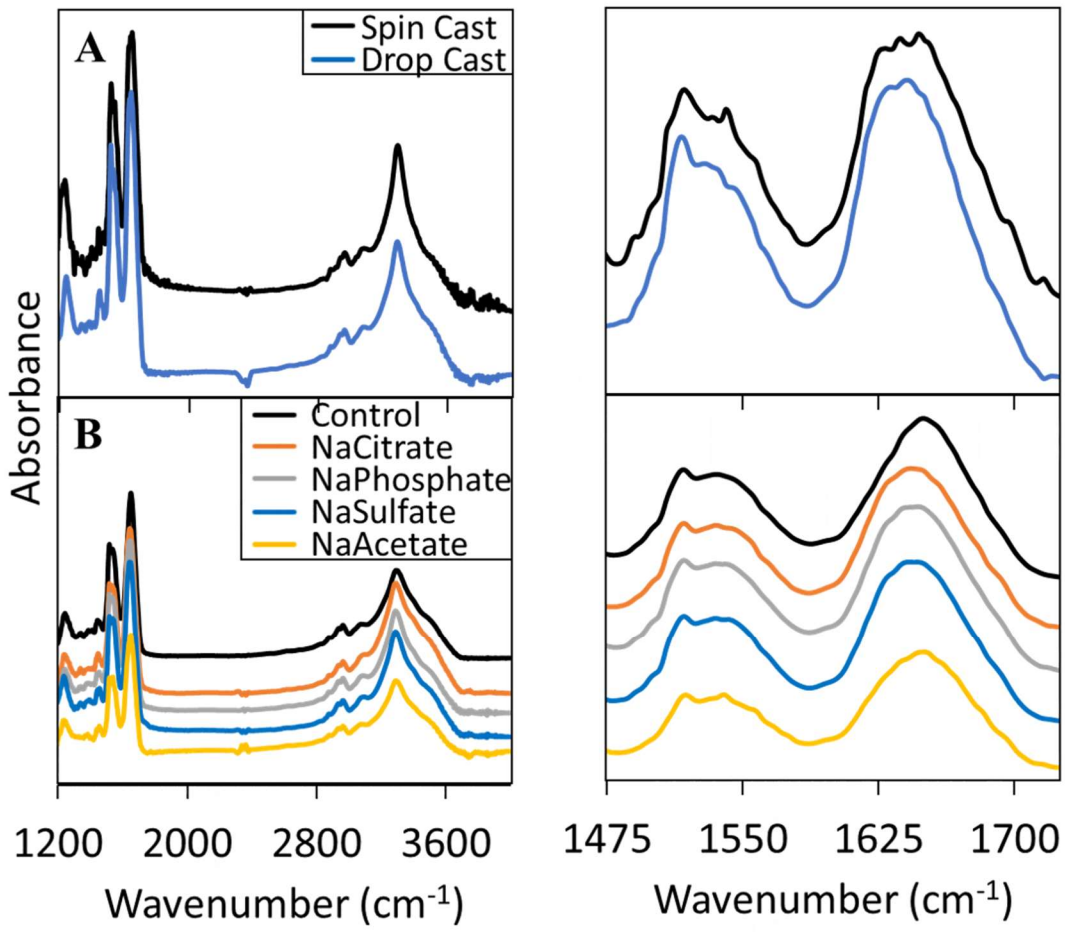

Figure B.1 ATR-FTIR spectra corresponding to those shown in Figures 6.1 (A) and 6.2 (B) meant to show the full length of the spectra taken (left) as well as a zoomed in version (right) showing the amide I and II bands.

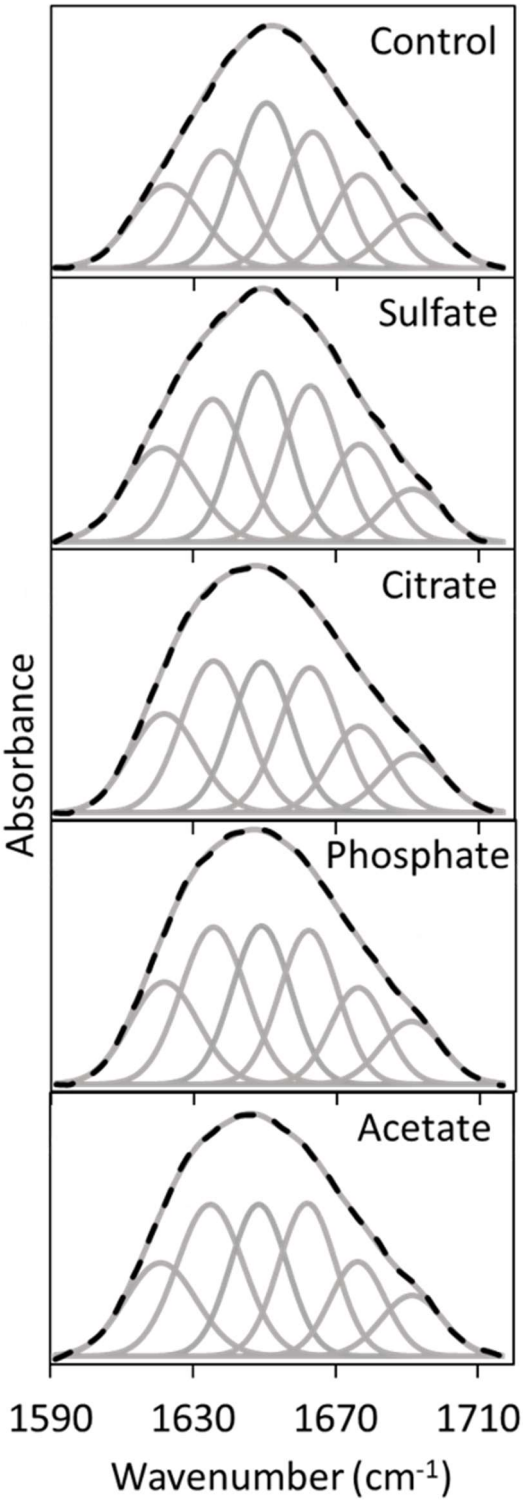

Figure B.2 Peak deconvolutions (grey) of the amide I bands in ATR-FTIR spectra of suckerin-12 films before and after salt annealing (Figure 6.2). The original background subtracted curve is shown as a black dashed line.

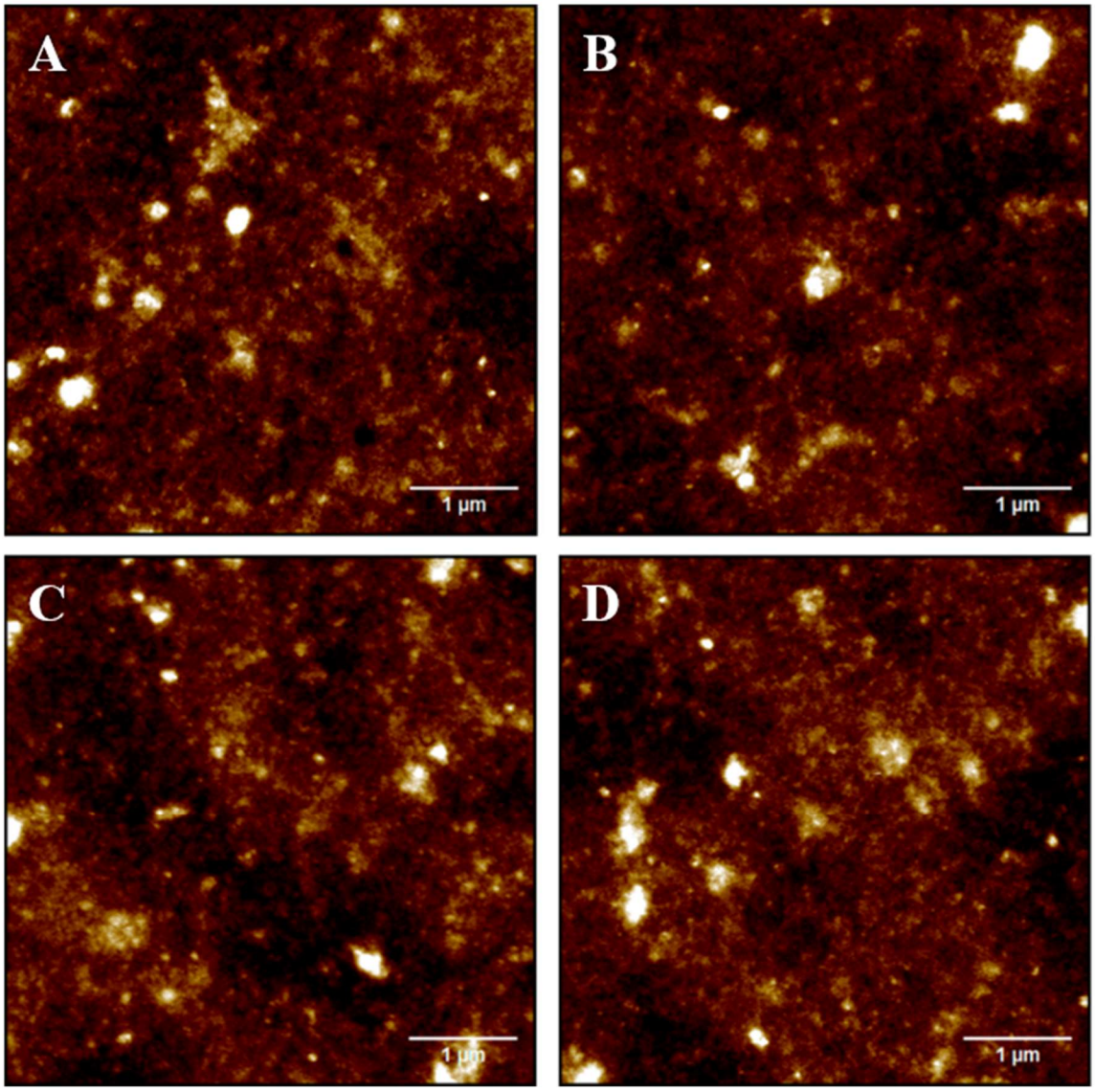

Figure B.3 AFM topographical images of spin cast 3 wt% suckerin-12 films after salt annealing for 1 hour with sodium phosphate (A), sodium acetate (B), sodium citrate (C), and sodium sulfate (D). Scale: 1 um. Z range: 33 nm (A), 38 nm (B), 30 nm (C), and 36 nm (D).

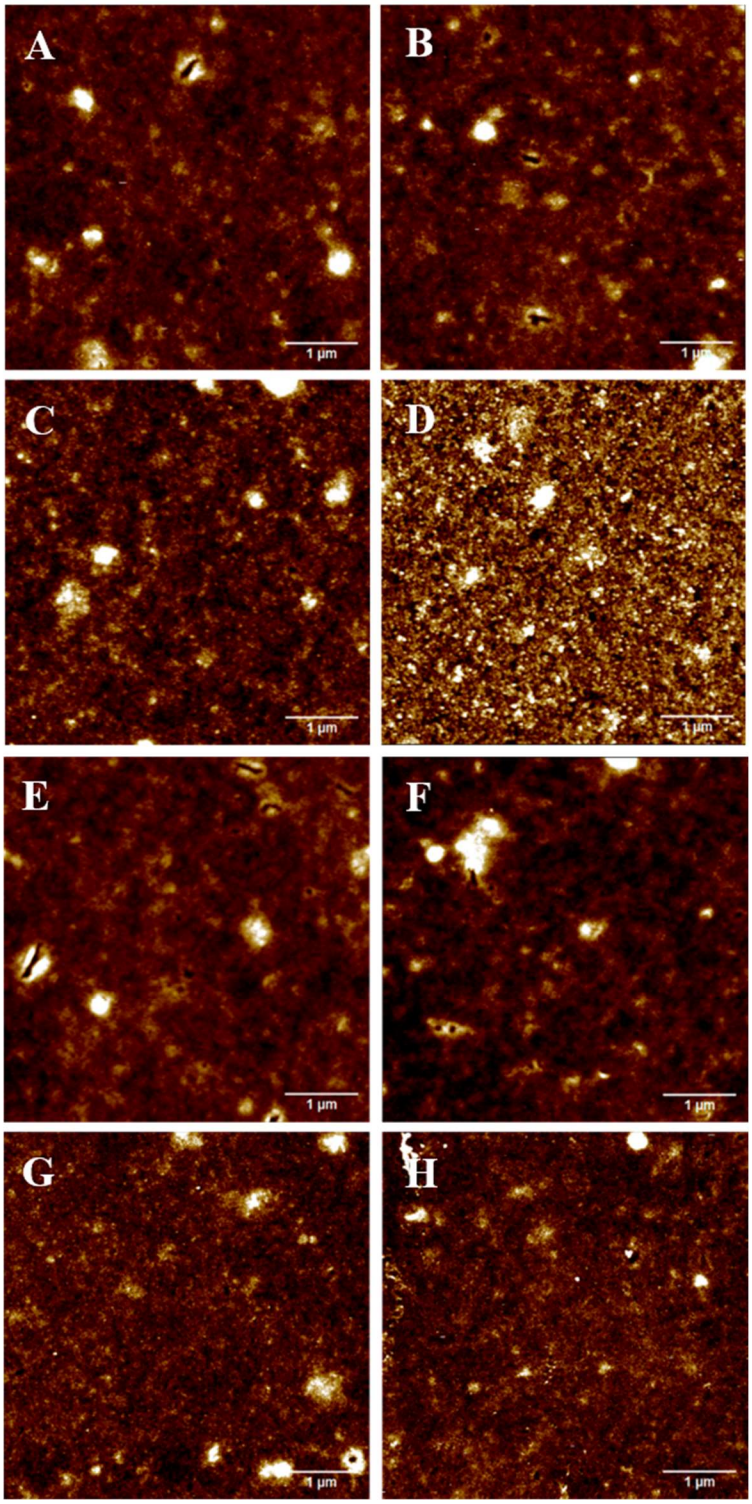

Figure B.4 AFM topographical images of spin cast, salt annealed 3 wt% suckerin-12 films before (A, C, E, G) and after (B, D, F, H) immersion in water. The samples shown were neat (A, B) and annealed with sodium phosphate (C, D), sodium acetate (E, F), sodium citrate (G, H), and sodium sulfate (I, J). Scale: 1 um. Z range: 20 nm (A-H).

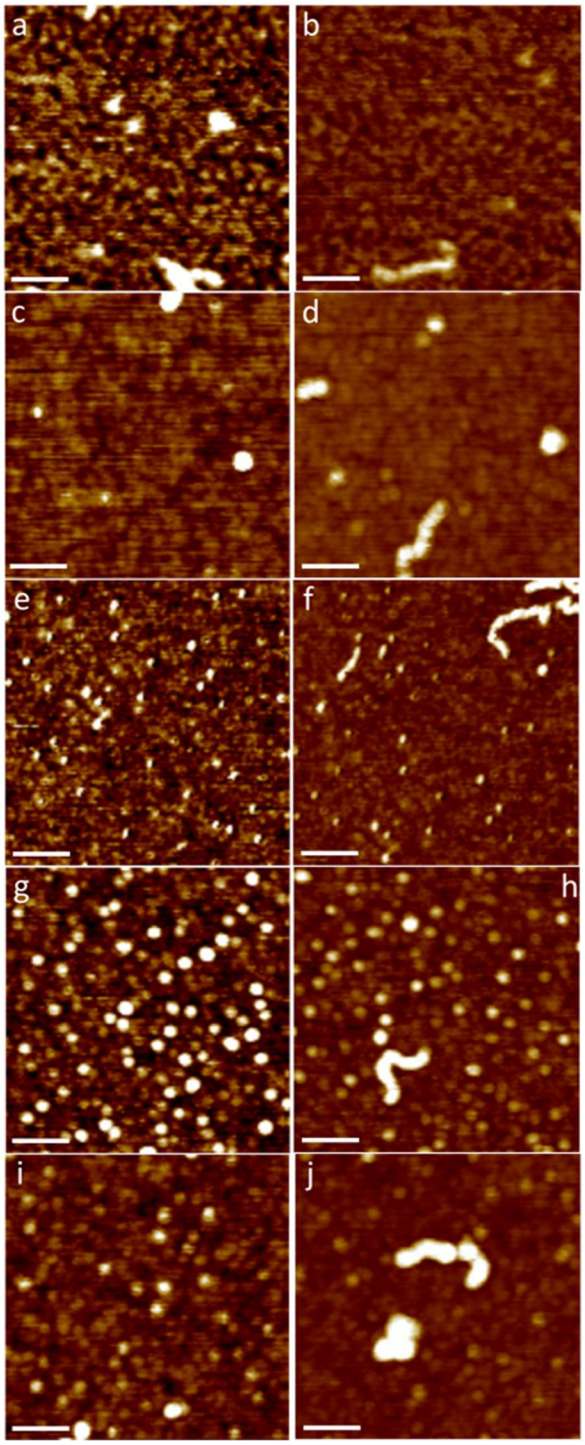

Figure B.5 AFM topographical images displaying overall morphology (a, c, e, g, i) and isolated fibrils (b, d, f, h, j) of suckerin-12 films drop cast from 0.1 wt% solution, rinsed, and then salt annealed for 16 hours with 100 mM of sodium sulfate (c, d), sodium citrate (e, f), sodium phosphate (g, h), and sodium acetate (i, j). Scale bars are 100 nm and Z scales are 2.5 nm (a, c, e, g, i) and 6 nm (b, d, f, h, j).